Spring 2020

Experimental Study and Numerical Simulation of Heat Transfer and Fluid Flow in Laser Welded and Brazed Joints

Masoud Mohammadpour
mohammadpour@smu.edu

EXPERIMENTAL STUDY AND NUMERICAL SIMULATION OF HEAT TRANSFER AND FLUID FLOW IN LASER WELDED AND BRAZED JOINTS

Approved by

Dr. Radovan Kovacevic

Dr. Blair Carlson

Dr. Xin-Lin Gao

Dr. Wei Tong

Dr. Xu Nie

EXPERIMENTAL STUDY AND NUMERICAL SIMULATION OF HEAT TRANSFER AND FLUID FLOW IN LASER WELDED AND BRAZED JOINTS

A Dissertation Presented to the Graduate Faculty of the

Bobby B. Lyle School of Engineering

Southern Methodist University

in

Partial Fulfillment of the Requirements

for the Degree of

Doctor of Philosophy

With a

Major in Mechanical Engineering

by

Masoud Mohammadpour

(B.S., Tabriz Azad University, Iran, 2010)
(M.S., Urmia University, Iran, 2012)

May 16 , 2020

ACKNOWLEDGEMENTS

My sincere gratitude goes to Professor Radovan Kovacevic, my advisor, for his continuous support and guidance in my research and completing this dissertation. He has been my mentor any time I needed advice and I will never forget his sincerity and consistent encouragement. I would like also to appreciate my advisory committee members, Dr. Blair Carlson, Dr. Wei Tong, Dr. Xin-Lin Gao, and Dr. Xu Nie for their support and valuable suggestions.

My special thanks goes to Mr. Andrew Socha for his help in preparing experimental setups and providing technical assistance. I was fortune enough to have a number of wonderful colleagues in RCAM and very thankful for their invaluable help, friendship, and for all the good memories we have made in the last four years.

As always, I want to express my greatest appreciation for my parents, Alieh and Gholamreza, for their unconditional support and endless patience. I could never stand here without their unspeakable sacrifices. My sister and life mentor, Lida, has been so generous with her love and encouragement and I cannot thank her enough for that.

Last but not least, I am very grateful for my beloved wife, Saba, for her great companion, motivation, self-devotion, and patience during my graduate study.

This work was supported financially by National Science Foundation and General Motors.

TO MY WIFE AND PARENTS

Masoud Mohammadpour B.S., Tabriz Azad University, Iran, 2010
M.S., Urmia University, Iran, 2012

Experimental Study and Numerical Simulation of Heat Transfer and Fluid Flow in Laser Welded and Brazed Joints

Advisor: Professor Radovan Kovacevic

Doctor of Philosophy degree conferred May 16, 2020
Dissertation completed May 5, 2020

Laser joining with advantages of high power density and high processing speed is becoming a dominant process for joining parts of the body in white (BIW) in automotive manufacturing. Aluminum alloys and new generations of advanced high strength steels (AHSS) are of great value for the automotive industry to build light weight, environmentally-friendly, high-quality, and durable vehicles. Their usage in body structure is increasing due to high strength-to-weight ratio and good formability. Lap and coach-peel joints are the most commonly used type of joints in assembly of the body components manufactured with each of these two alloys.

Laser brazing is a widely used process for joining closure panels in automotive manufacturing exemplified by joints such as the upper to lower panels of a liftgate or the roof to body side outer panels. Laser brazed seams are in visible areas and require a high quality surface and seam characteristics. Therefore, in this study novel techniques were studied to develop a robust welding and brazing processes of similar and dissimilar materials. Experimental studies as well as the numerical modeling and high-speed imaging approaches were used to gain a deeper understanding of the laser welding-brazing process, determine the effect of process parameters on weld dimensions, and analyze the dynamics of possible imperfections during the process.

In dissimilar application, a feasibility study was conducted on laser joining of aluminum alloy to galvanized steel by means of twin-spot laser beams. Twin-spot mode was introduced to heat up a large surface area with less reduction in energy density for coach-peel joints with a wider geometry. The filler material was brazed on the steel side and partially fusion-welded on the aluminum side. The brazed results were investigated from the perspectives of microstructure evolution, tensile strength, surface roughness, edge straightness, and fracture mechanism. The generation of intermetallic compound (IMC) at the steel/seam interface was optimized by introducing a validated finite element thermal model to obtain the temperature history during the process and predict the thickness of a possible IMC layer. A multi-response optimization approach based on response surface methodology (RSM) was developed to find the fit model that correlated the main process parameters (laser power, wire feed speed, and scanning speed) and their interactions to surface roughness and mechanical strength. Under optimum processing condition the effects of alloying elements were also investigated on the performance of resultant joints. Different percentages of Si, Mn and Zn were introduced into the weld through three Al-based ($AlSi_{12}$, $AlSi_5$, and $AlSi_3Mn$) and one Zn-based ($ZnAl_{15}$) filler wires. Joint mechanical properties were examined in terms of monotonic loading circumstance. Microstructural properties were evaluated in terms of the IMC layer thickness and composition.

In laser brazing of galvanized steels, the effect of laser beam inclination angle was investigated on process stability and spatter occurrence. Steel outer panels in automotive application are zinc coated for improved corrosion protection; however, the existence of low boiling element in coating has made the laser brazing process more challenging. Zinc has a boiling point of 907 °C which is lower than the melting range of copper-based filler wire, 965 – 1032 °C and as such is the predominant cause of laser brazing process instability and spattering for zinc

coated steels. Therefore, experimental and numerical methods were applied to investigate the effect of laser beam inclination angle on laser braze quality of galvanized steels. High-speed videography revealed that spatter mostly occurred at the wetting line and melt pool front where the escaping zinc vapor came into interaction with the melt material. Application of a developed thermo-fluid simulation model considering laser-material interaction, wetting dynamics, material melting, and solidification, resulted in temperature profiles during the brazing processes for given beam angles as well as both the positions of the zinc evaporation front and wetting front. It was found that negative travel angles helped to move the zinc evaporation front ahead of the wetting front and reduce the interaction between the zinc vapor and melt pool. Experimental observations confirmed that partially removing and/or evaporating the zinc layer ahead of the wetting zone contributed to a stable process and good braze quality.

TABLE OF CONTENTS

LIST OF FIGURES

Figure Page

LIST OF TABLES

Table Page

Chapter 1

INTRODUCTION

1.1 Types of laser joining processes and applications

In last decade the utilization of laser-based material processing over traditional methods has increased tremendously. Contributing factors are the many advantages including the feasibility of complete automation, reaching a high processing speed, a higher quality product, cost reduction, and a smaller heat affected zone [1, 2]. Laser beam material processing is an umbrella term that refers to the four main groups of manufacturing process (1) forming, (2) joining, (3) machining, and (4) surface engineering [3]. A comprehensive classification of these laser-based fabrication techniques with a few representative examples from each category is provided in Figure 1.1. However, as the field matures, new developments and innovations continue to emerge in both the lasers themselves and their applications.

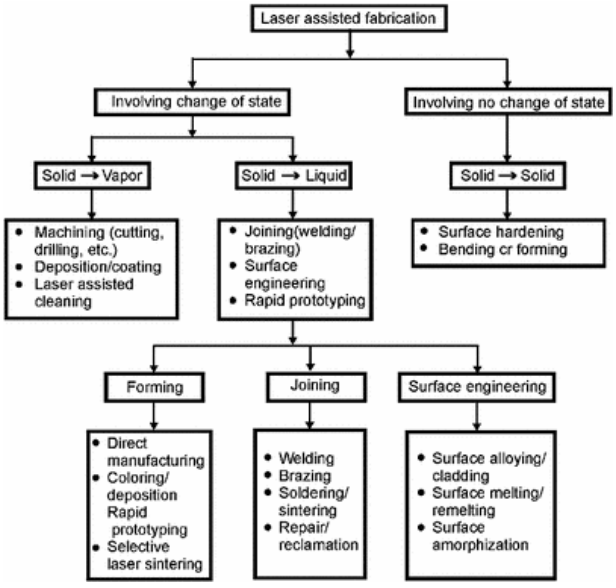

Figure 1.1 General classification of laser-based joining and manufacturing methods for engineering applications [3].

The common thread connecting these processes is their employment of lasers; however, each process utilizes distinct parameters. The most important parameters are the power density and interaction time that play a crucial role in changing the regimen of the process zone. As shown in Figure 1.2, the processing map can distinguish the different laser processes according to the laser power and interaction time. In this dissertation, two typical joining techniques, including laser brazing, and autogenous laser welding are considered.

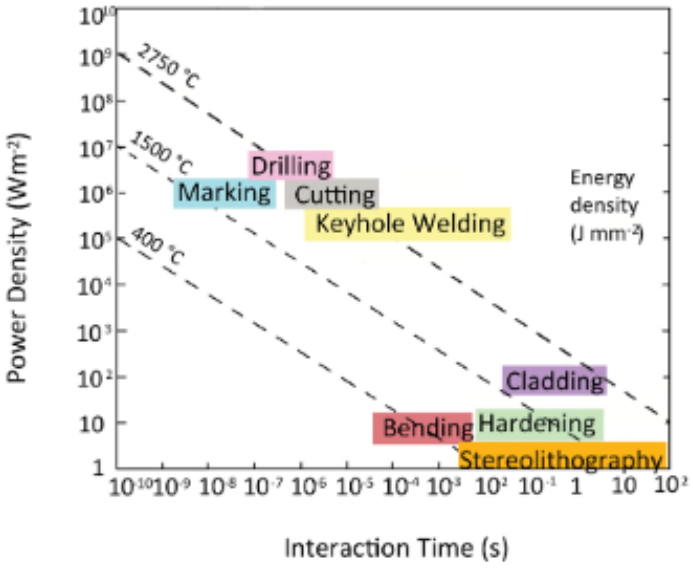

Figure 1.2 Effects of basic laser material interaction parameters in laser processes [4].

Generally laser joining processes can be categorized into three main types (see Figure 1.3) laser brazing, autogenous laser welding (with conventional and remote scanner heads), and laser welding assisted with wire. These modern technologies are widely used in different industries to join various types of materials like carbon steel, high-strength steel, stainless steel, titanium alloys, nickel-based alloys, and reflective metals like aluminum and copper alloys in similar and dissimilar conditions. The main advantages over the other fusion welding processes can include the high processing speed, large depth/width ratio of the weld bead, and limited size of the heat-affected zone (HAZ)[1]. The automotive industry is the best example that has received great

benefits and has been completely revolutionized with the advent of laser joining processes. As shown in Figure 1.4 a large number of applications can be found in the powertrain, components, chassis, body in white (BIW), engine, interior, and exhaust systems [2, 5].

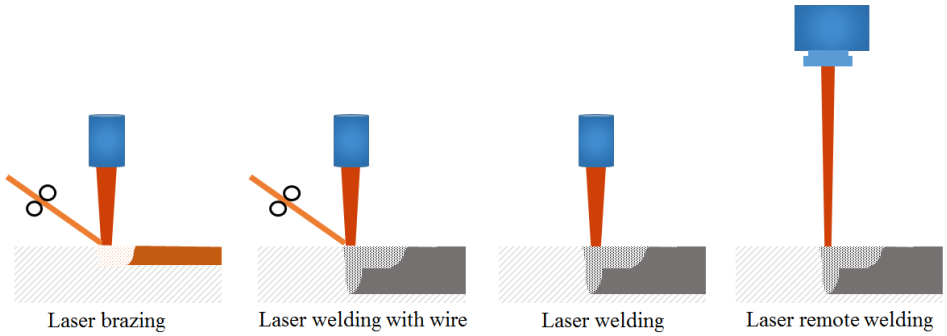

Figure 1.3 Types of laser joining processes.

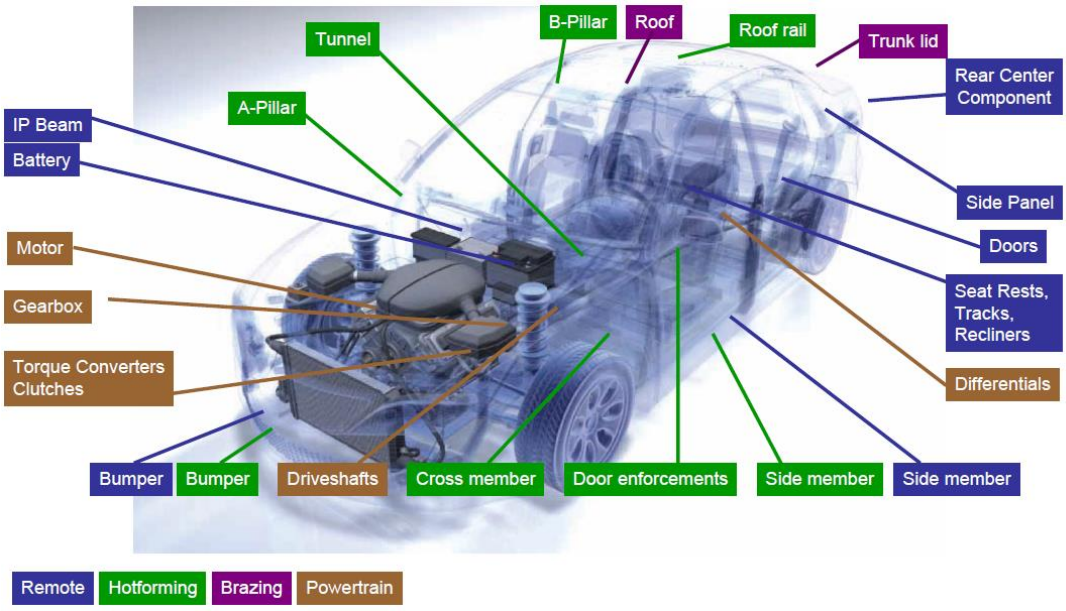

Figure 1.4 Application of laser welding in the automotive industry [6].

1.2 Application of galvanized steel and aluminum alloys in the automotive industry

To identify the materials that have potential for use in car manufacturing several criteria like ease of manufacturing, environmental issues, low cost, design parameters, and manufacturing consistency should be considered in material selection [7]. In addition to these criteria, steel with

an effective combination of high strength, and low yield-to-tensile ratio is considered the predominant material in the automotive industry. Currently, most of the steel sheets in car-bodies are zinc-coated for the purpose of enhancing corrosion resistance as well as facilitating the stamping process and product durability. The zinc coating process can enhance the life time of manufactured parts with galvanized steel that has allowed automakers to provide voluntary warranties for corrosion protection lasting as long as 12 years [8].

To control global warming and reduce the emission of CO_2, the U.S. Environmental Protection Agency requires significant improvements in the fuel efficiency of vehicles. Fuel economy rules mandated that 2016 vehicle models were required to average 35.5 miles per gallon (mpg). This standard mandates an increase to 54.5 mpg by 2025 (see Figure 1.5) [9]. To achieve this goal, two main approaches have been proposed: development of new powertrain solutions and mass reduction in vehicle body weight. Reducing the overall weight of a vehicle was recognized as the most effective way to enhance the fuel efficiency. To tackle this approach, two main interests in alternative lightweight materials and development of advanced high-strength steel have been growing in the automotive industry.

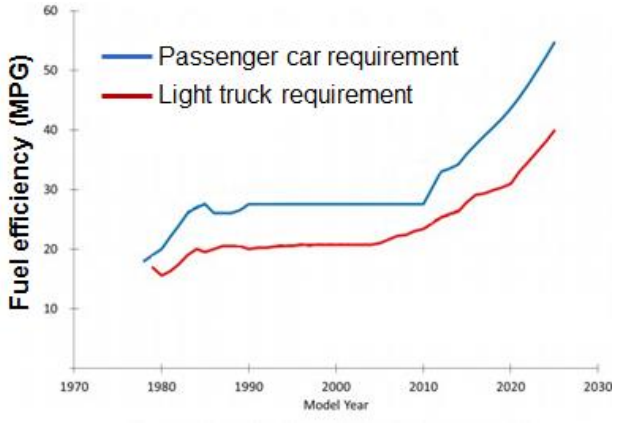

Figure 1.5 Fuel economy standards by model year [9].

The replacement of conventional steel by lightweight materials, such as aluminum (Al), magnesium (Mg), and titanium (Ti) for application in the skin panels and components has aroused the attention of researchers [10]. Aluminum is the most promising lightweight material due to its higher strength-to-weight ratio and lower cost over Mg and Ti. The application of aluminum alloys can reduce the weight of vehicles by up to 50% [11]. The utilization of aluminum has not been limited to casting components. Due to satisfactory performance, the application of aluminum has spread to the chassis construction frame and BIW assemblies [12]. In this regard Audi announced its intent to reduce the vehicle body weight by 40% in manufacturing the A8 model by using an aluminum-intensive space frame [13]. The construction of an automotive body structure typically consists of 6xxx series and 5xxx series aluminum alloys. Components such as latch and hinge reinforcements are made from 5xxx series non-heat treatable aluminum alloys while parts such as deck lids, roofs, and other outer panels are made of 6xxx alloys [13].

Joining aluminum alloys using either laser-based or resistance methods is more challenging than welding steel [14]. This can be attributed to the special features of aluminum alloys such as high reflectivity, high thermal expansion coefficient, high thermal conductivity, porosity generation during the welding process, and the oxide layer on the surface. Therefore, instead of finding better joining methods for alternative materials, some manufacturers have focused on development of new grades of advanced high strength steels (AHSS). The first generation (Gen. 1) of the AHSS family included dual phase (DP) steels, complex phase (CP) steels, transformation-induced plasticity (TRIP), and Ferritic-Bainitic (FB). The AHSS Gen. 1 was better positioned than conventional steels in terms of strength-elongation of the product. The AHSS second generation (Gen. 2) family achieved twining-induced plasticity (TWIP) and lighter weight with induced plasticity (L-IP). However, the higher cost of production was found to be prohibitive in finding

applications. Compared to Gen. 1 and Gen. 2 steels, the 3rd generation (Gen. 3) AHSS has a better combination of high strength and superior ductility. As a result, they have received an increasing interest from both the steel and automotive industries [15]. The well-known "banana plot" depicts tensile elongation of different AHSS generations as a function of strength (see Figure 1.6).

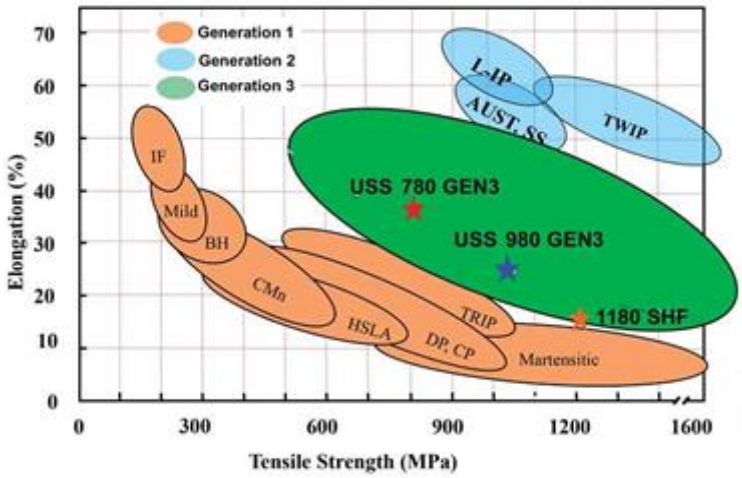

Figure 1.6 The ductility - tensile strength of AHSS [15].

A bypass and cost-effective method of producing a hybrid aluminum-steel structure is currently available in the BIW application [10]. This method achieves an even lighter vehicle with higher stiffness with respect to available materials. In this approach, the "mixed materials strategy" of using the right material in the right place in the right amount is applied. However, the entire vehicle is, in general, made from mixed materials, including the Al engine blocks and suspension parts, steel bodies, plastic trim, and Mg instrument panel support beams. Typically, such parts were attached to a predominantly steel body (i.e., a steel BIW) in final assembly. However, in this novel concept, the body structure is made from mixed materials incorporating several grades of steel and Al sheets. As shown in Figure 1.7 aluminum alloys can be used in nonstructural outer panels, such as roofs, hoods, fenders, and trunk lids. From both a mechanical point of view and an economical perspective, to maintain car crashworthiness, it is not possible to

replace steel as cheap as three times with aluminum. Thus, hybrid steel-aluminum structures have been introduced as a good replacement for many common all-steel body structures, making the joining of aluminum to steel inevitable [10]. This approach has opened up an attractive field of research for joining aluminum and steel alloys together.

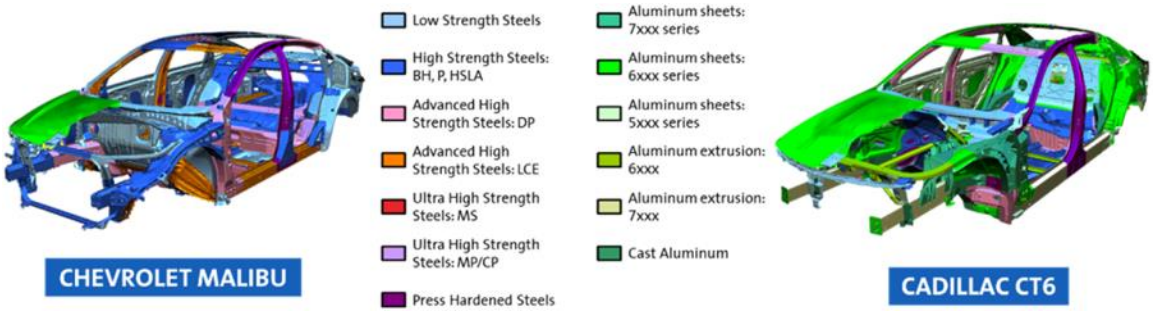

Figure 1.7 General Motors' first completed vehicle with a body made from mixed materials [16].

1.3 Laser brazing

Laser brazing is a metal joining process based on melting a cold/hot filler wire with a laser beam. The brazing wire is introduced into the braze seam via a wire feeder unit. The filler wire was heated above melting point allowing molten material to flow into the seam between two or more close-fitting parts by capillary action. In comparison to soldering, the temperature of brazing must be greater than 450 ℃ and lower than the melting temperature of the base metal. Laser brazing is a low-input process in which the defocused or magnified laser spot that is typically 1-2 times larger than the diameter of filler wire delivers a low energy level (105 W/cm^2) during the process [17]. At low levels of energy density, the laser beam only interacts with the surface of the weld bead, and then the heat is transferred to the interior by conduction in the so-called "laser conduction" mode. The high-speed processing condition up to several meters per minute at a very low-heat input is accompanied by a short heating time, small heating area, and low distortion. Laser brazing has been commonly used in the automotive industry for joining closure panels which

are in visible areas of the car body "class A joints". Example applications are the joining of a roof panel to the outer body side, and the joining of an upper decklid panel to a lower decklid panel (see Figure 1.8 (a-b)). This process has dramatically revolutionized the BIW assembly not only in reduction of processing time but also the final joint quality. The resulting joints are aesthetically pleasing and require minimal secondary finishing [17]. As shown in Figure 1.8c the number of steps to complete the roof joint is decreased from 3 to 1.

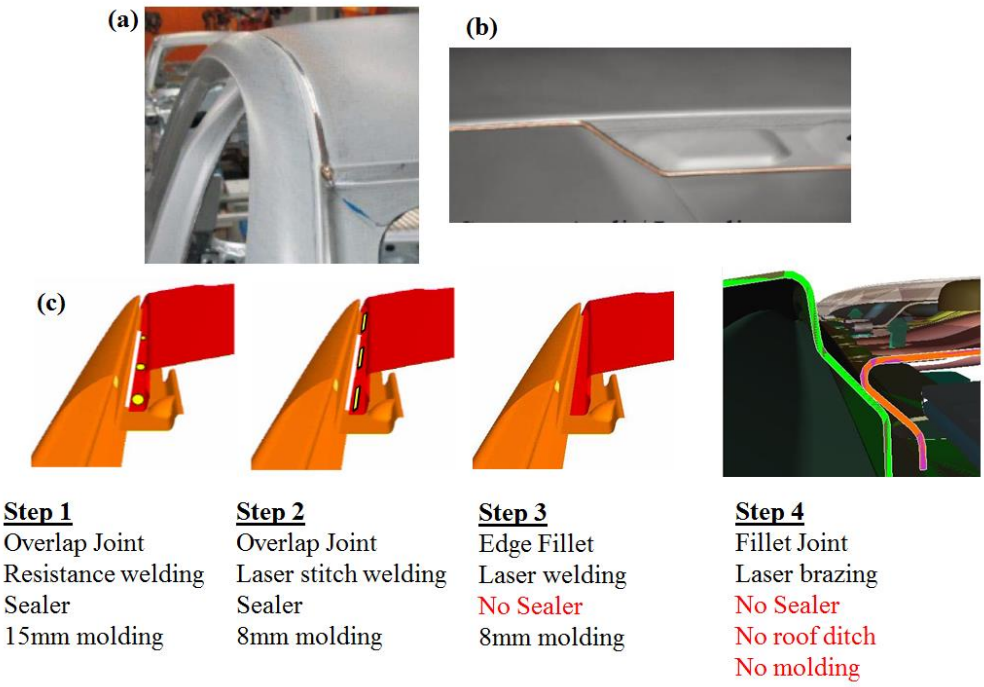

Figure 1.8 (a-b) Typical configuration of laser brazing joints in BIW, (c) Development process in roof joining techniques [6].

1.3.1 Effects of parameters in laser brazing

The effecting parameters on the final quality of the joint during the process can be categorized into the three main sections of process parameters, heat source, and materials (see Figure 1.9).

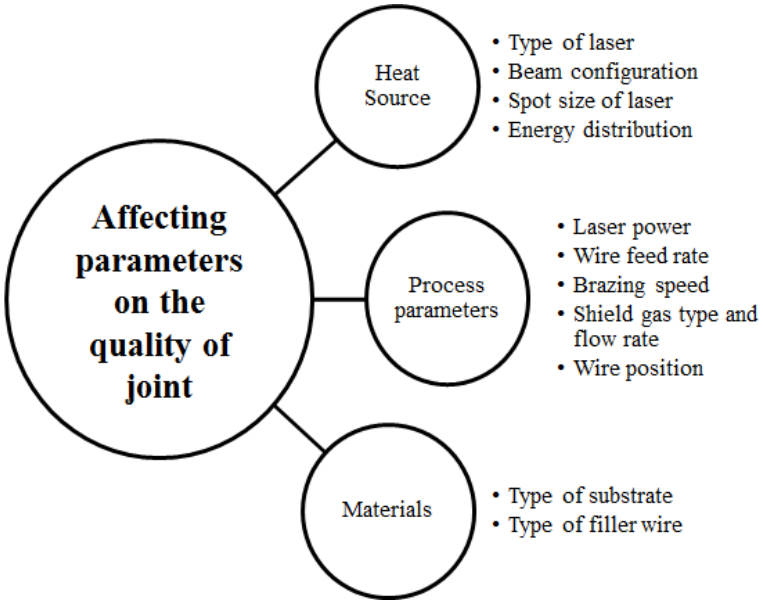

Figure 1.9 Influential parameters in laser brazing process.

The heat source parameters consist of laser type, wavelength, beam diameter, continuous or pulse wavelength mode, energy distribution, and more importantly beam shape. The energy distribution plays a crucial role in this laser-based joining process, and it has significant effect on the final beads [18]. To enhance the quality and mechanical properties of laser brazed joints, along with the developments in single laser beam mode, several multi-beam laser modes were developed for this process [19, 20]. Figure 1.10 depicts different types of available multi-beam lasers for the application of the laser brazing process. The difference of energy distribution between Gaussian and Top-hat is also noticeable. The three main processing parameters (LP, BS, WFR) play a crucial role in the level of heat input and directly affect the stability of the process. Their individual changes can lead to process defects that are directly related to the level of applied energy level.

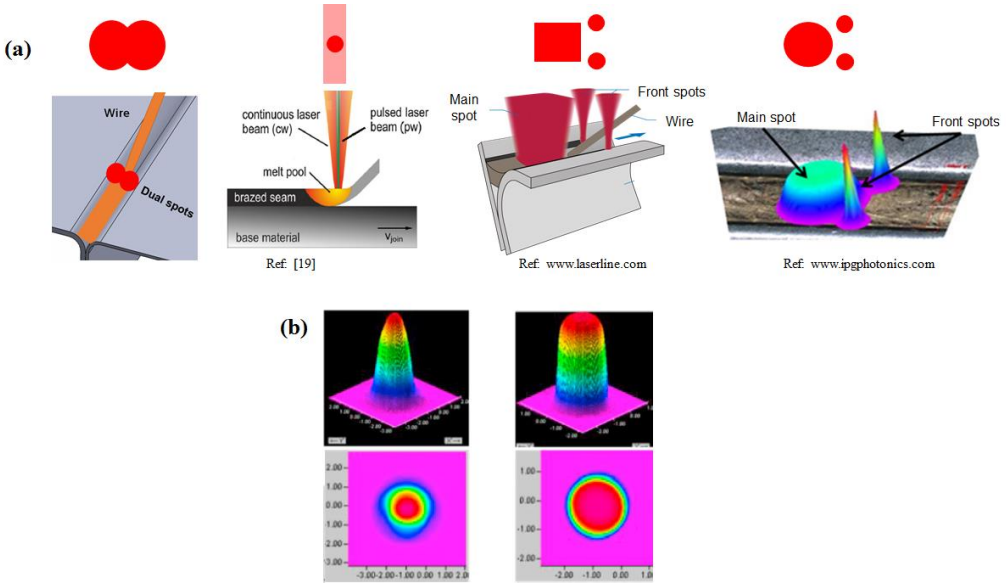

Figure 1.10 (a) Developed multi- beam lasers for brazing process, (b) Comparison of energy distribution of YAG (left) and diode (right) laser beam [18].

Laser brazing was developed to join steel and aluminum panels by means of Cu-based, Al-based, and Zn-based filler materials. Therefore, each set of material combinations with specific material properties are matter in final quality and process parameters. Laser efficiency, or laser energy transfer efficiency, describes the percentage of energy absorbed by the work-piece. This behavior directly relates to the material's surface quality and reflectivity [21]. The combination of process parameters and efficiency determined by the processing parameter create a complicated physics behind the small size of the molten pool, including melting, fluid flow, mass and heat transfer, solidification, free-surface deformation, and interfacial reaction. Surface tension in the molten pool largely depends on its composition and temperature. Without considering the influence of heat input and chemical elements, the values of surface tension σ_{sol-g}, σ_{sol-l}, and σ_{l-g} could be altered during the interaction of gas and the molten metal [22]. In addition, disturbances could be caused by the hydraulic pressure difference when the drop of filler wire falls into the molten pool. Pressure could build from the plasma plume and the shielding gas impinging

on the molten weld pool surface. Consequently, the idea to improve the weld surface quality by controlling the flow of filler wire into the molten pool and optimizing the shielding gas parameters comes naturally. Therefore, the type and flow rate of shielding gas is another influential parameter. Shielding gas not only protects the molten material from oxidation but also increases the laser absorption coefficient by blowing off the plasma and stabilizing the process. Zhang et al. [23] investigated the effect of gas composition on stability of laser processing. They found that different shielding gases have a tendency to form different plasma. The shielding gas with a lower molecular weight, higher thermal conductivity, and higher ionization energy will generate less plasma. As shown in Table 1.1, helium gas is the most effective to suppress the plasma and increase weld penetration. With respect to argon, helium as a low density gas requires a higher flow rate to provide better protection for the molten pool. Due to the economic consideration, argon or a mixture of argon and other shielding gases is normally chosen as the shielding gas.

Table 1.1 Physical properties of shielding gases [23].

	Molecular weight (g/mol)	Thermal conductivity (W/m.k)	Ionization energy (ev)
Helium	4	0.15363	24.6
Nitrogen	28	0.0255	15.6
Argon	40	0.01732	15.8

1.3.2 Dissimilar laser welding-brazing

Laser brazing process as a method for joining like materials was also implemented for dissimilar applications or so-called “laser welding-brazing” where aluminum panels are joined to dissimilar materials, such as steel [24]. Figure 1.11 shows a schematic view of a dissimilar concept in laser brazing. In the body structure of vehicles, aluminum alloys can be used in nonstructural outer panels, such as roof, doors, hood, front and rear fenders, and trunk lids. During the joining process, the aluminum substrate is melted, whereas the steel substrate is only wetted

by the Al-based filler material within a melting range of 570℃-640℃. When joining aluminum alloys to steels by laser, the large electrochemical difference, different thermal properties, dissimilar thermal expansion, heat capacity and thermal conductivity, different lattice transformation and melting points and nearly zero solid solubility are led to the generation of a brittle Al/Fe intermetallic compound layer at the interface [25]. Figure 1.12 represents the Fe-Al phase diagram and possible composition of intermetallic compounds at the dissimilar interface.

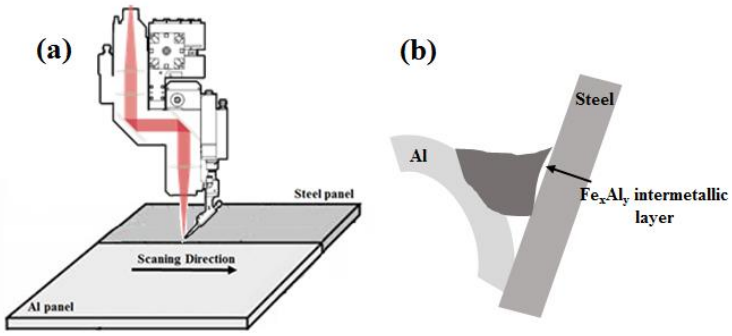

Figure 1.11 (a) The representation of dissimilar brazing, (b) Schematic cross-sectional view of aluminum to steel joint.

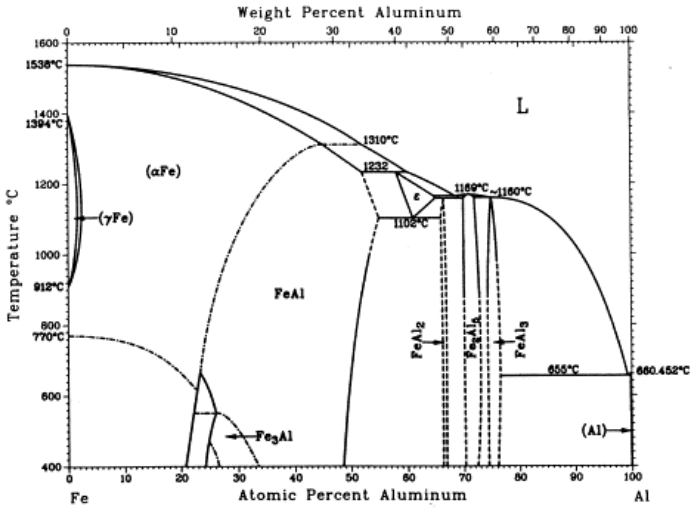

Figure 1.12 Fe-Al binary phase diagram [26].

The formation of intermetallic is governed by a diffusion mechanism [27]. This mechanism is strongly related to the temperature reached at the Al/Fe interface and the time of interaction at high temperature related to the cooling speed. Therefore, the key point is finding a way to control the size and quantity of the Al/Fe intermetallic compound (IMC) layer. Schubert et al. [28] manipulated the diffusion process in laser welding of dissimilar materials by modifying the heat input. They could not only control but also restrict the formation of the IMC layer. The time and temperature dependent nature in growing the IMC layer can be resolved. Al_5Fe_2 is the first thermodynamically stable Fe-Al phase to nucleate, because Gibbs energy follows the sequence of $\Delta G0(Al_5Fe_2) < \Delta G0(Al_3Fe) < \Delta G0(Al_2Fe) < \Delta G0(AlFe) < 0 < \Delta G0(AlFe_3)$ [28].

1.3.3 Issues in the laser brazing process

In the automotive industry, laser brazing is expected to join the outer surface parts, because the heat input is easily controlled and the brazed bead appearance is very smooth and good [29]. A Cu-based filler wire is utilized for galvanized steel sheets, and Al-based filler wires are used for joining aluminum-to-aluminum and aluminum-to-steel sheets. As discussed previously several parameters are involved in this process. The correct tuning up of those parameters to an appropriate level of energy is a vital prerequisite to deliver high strength and smooth surface joints. In conditions with a higher energy level (high laser power, low brazing speed, low wire feed speed) defects like open-out holes, overheat, black soot, and more spatter may occur. In contrast, unmelted wire and rise are the typical defects that could be observed in lower energy levels. Figure 1.13 shows the typical brazed defects found in laser-brazed beads, resulting in degradation of the bead surface appearance and reduction in the joint strength.

Figure 1.13 Different type of seam imperfections in the laser brazing process [30].

The imperfections listed above can be classified as imperfections of the seam geometry. Some types of imperfection like unmelted wire (see 1st column of Figure 1.13) and one-sided wetting (see 2nd column of Figure 1.13) can be observed in both similar joints and aluminum-to-steel dissimilar joints. These defects can be attributed to the low energy level and misalignment of laser spot with the filler wire, respectively. The major cause for the formation of open-out holes can be attributed to (1) unsteady relation of wire feed and brazing speed; (2) low wire feed rates; (3) unsteady wire movement in the lateral and/or vertical direction (e.g., due to a large diameter wire nozzle). Porosity and spatter (see 3rd column in Figure 1.13) are merely the types of imperfection that are observed in laser brazing of galvanized steel sheets and dissimilar Al/Fe joints. These imperfections can be attributed to the existence of zinc coating on steel panels as the low boiling element. The zinc's boiling point of 907 °C is lower than the melting range of copper-based filler wire 965-1032 °C. Kimura et al. [31] observed experimentally that high-pressurized zinc vapor expels from underneath the molten filler material. The vapor results in seam defects like open-out holes, porosities, and a large amount of it results as spatters. The highly-pressurized zinc vapor during the brazing process disrupts the melt pool stability. The vapor even can permeate the molten material and result in spatter defects. In a dissimilar joining process with the use of Al-based filler wires that have a lower melting range 570-640 °C than the boiling temperature of the zinc layer, there is a possibility of porosity generation inside of the brazed bead. During the

process at the interaction area, the zinc layer was liquefied instantaneously during wetting of the molten material on the coated substrate. The interaction between zinc and the filler material was also potentially governed by solubility effects. Zinc-related porosity might exist when the cooling time is too short to allow zinc to evaporate from the molten pool, as shown in Figure 1.14. Gatzen et al. [32] reported that preheating of the substrate can reduce zinc-related porosity and obtain small wetting angles. When the temperature of the substrate was elevated, the increased coating thickness (the local wt.% of zinc) was detrimental to the wetting and the width of the solidified droplets. Therefore, in the pre-heated condition, the zinc-coating should be as thin as possible to obtain increased wetting.

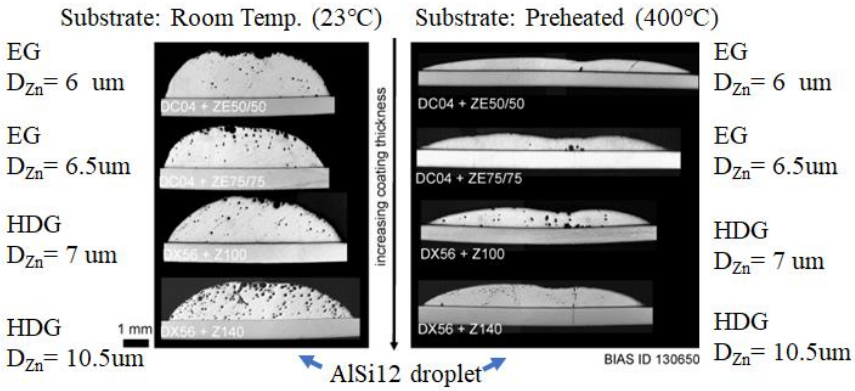

Figure 1.14 Results of sessile drop tests with substrates at the room temperature (left) and preheated to 400℃ (right) [32].

1.4 Applications of numerical simulation in heat transfer, fluid flow, and structural analysis of laser welding-brazing process

In recent years laser joining has become a more important technology that has found many industrial applications. Although, the physics behind this process has not yet been completely understood. The nature of laser beam welding and brazing processes are a combination and interaction of several physical effects such as laser and material interaction, phase change, fluid

flow, heat and mass transfer interaction of solid, liquid, and gas phases (Figure 1.15). The findings through experimental investigations provide valuable information in understanding the physics of process, dynamic correlations, and defects. Unfortunately, based just on experimental studies, some useful information is difficult to acquire, such as temperatures near or inside of the molten pool, pressure distribution in keyhole area, the fluid velocity field, solidification rate, flow direction, and so forth. Therefore, simulation can be a useful tool for a complete understanding of the process and formation mechanism of defects.

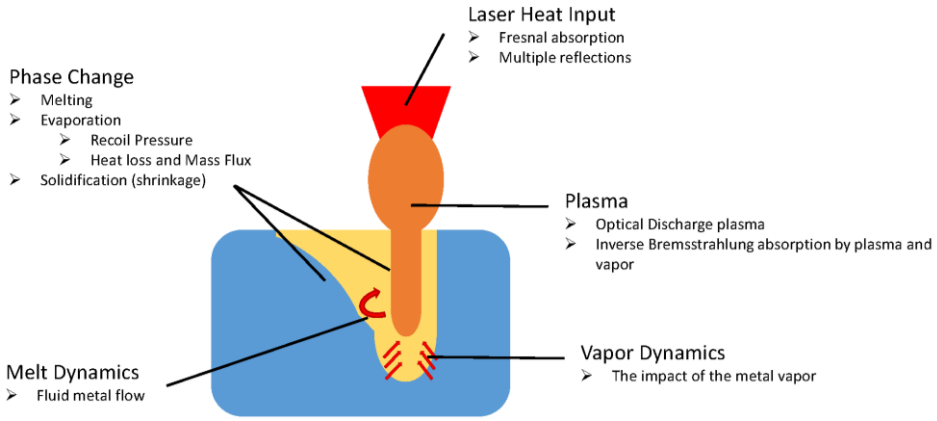

Figure 1.15 Schematic of physical phenomena in laser welding.

Another advantage of laser joining simulation is help for process optimization that could dramatically decrease the amount of costly and time consuming experiments. Numerical simulation can be utilized to predict the joint geometry, microstructure, temperature history, and other weld properties. These properties used to be obtained through trial-and-error experimental works [33]. As discussed earlier laser joining is a complex phenomenon that requires a "multi-physical" aspect for simulating the process. In spite of the rise in computer efficiency, a complete simulation, starting from light propagation until structural distortion, is currently not conceivable. For the moment, numerical codes are constrained to simulate the process scale by scale and to concatenate results. For example, the first step is laser and material interaction (multiple

reflection) that provides heat input to a heat transfer and fluid flow calculation. Then, heat transfer and fluid flow simulations, are coupled with a free surface tracking method and a multiple reflection consideration. The available heat distribution with the time, can be solved for a metallurgical problem to obtain material and phase properties and lead to a mechanical computation. However, there is no simulation model in literature that can encompass all of these physics in single model. As shown in Figure 1.16, the simulation of a laser joining process can be partitioned into two main groups of thermo-mechanical and multi-physical simulations [33].

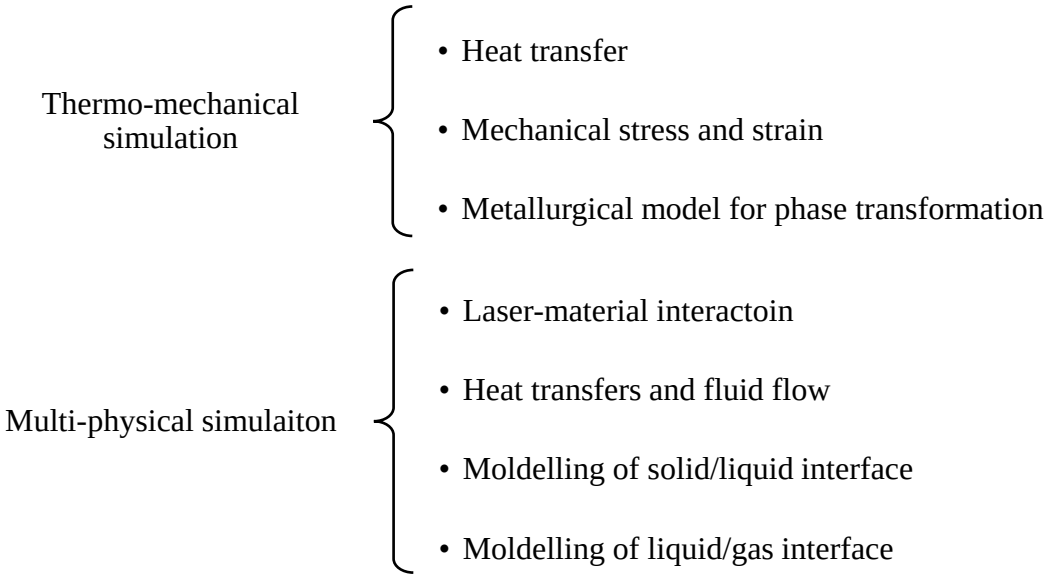

Figure 1.16 Different approaches in laser welding simulations.

The first priority of industry is the design and optimization of manufacturing processes and components. The simulation can be a handy tool to improve the production sequences and to minimize production problems. For this reason a huge amount of models try to calculate the thermal history, mechanical effects of welding as residual strains and distortions, and mechanical performance of laser welded joints under monotonic and cyclic loading circumstances. The algorithm of thermo-mechanical simulation as the conductive heat transfer approach can be shown in Figure 1.17.

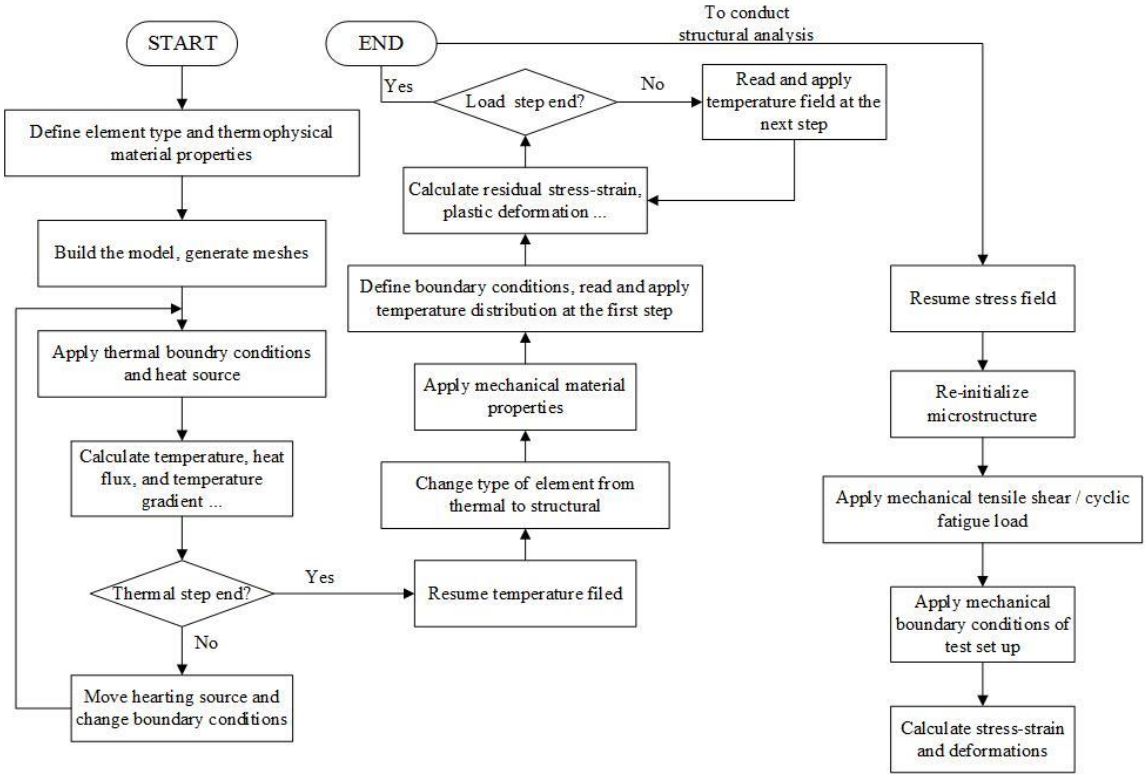

Figure 1.17 Flowchart of thermo-mechanical and structural simulations procedure.

Numerical simulation based on multi-physic solutions provides a scientific and effective way to reveal the process mechanism of laser welding. Much research focuses on modeling of laser-material interaction, dynamic of keyhole, precisely capturing the free surfaces, and laser absorption mechanisms of material. The application of finite element analysis (FEA) and computational fluid dynamics (CFD) models in temperature field analysis of dissimilar laser brazing and autogenous laser welding processes was employed. The validated mechanical model was developed to study the effect of processing parameters on the mechanical performance of laser welded joints.

1.5 Research objectives

The single-beam and multi-beam laser welding-brazing techniques are investigated to join steel and aluminum panels in similar and dissimilar conditions. The effects of processing

parameters on the weld quality and robustness of process are investigated experimentally and numerically. An on-line vision system based on a high-speed video imaging accompanied with green laser illumination source are also used to gain a better understandings of the molten pool dynamic behavior and defect occurrence mechanisms. The main objectives can be listed as follow:

- Implement a twin-spot laser joining procedure of dissimilar aluminum and steel in a coach peel configuration for the automotive industry. The main issues to address are the feasibility, quality of joint, process robustness, and formation of brittle intermetallic phases.
- Develop a thermal simulation model to capture the effect of process parameters on the temperature fields with the purpose of optimization as well as to minimize the thickness of the intermetallic layer.
- Conduct a comprehensive process parameters optimization to identify influential parameters, their interactions, and effect of the wire alloying elements on the mechanical strength and quality of dissimilar welded joints.
- A novel method for measuring weld edge straightness is developed and an acceptable quality criteria based on human vision resolution is introduced.
- Introduce a process window graph so-called “Brazibility graph” for the laser brazing of galvanized steels in roof joint of car-body.
- Develop a thermo-fluid simulation model to study the formation of braze seam and calculate the temperature history and velocity fields in the melt area.

References

[1] K.J. Lee, S. Kumai, T. Arai, Interfacial Microstructure and Strength of Steel to Aluminum Alloy Lap Joints Welded by a Defocused Laser Beam, Materials Transactions, 46 (2005) 1847-56.

[2] W.M. Steen, J. Mazumder, Laser Welding. Laser Material Processing. London: Springer London; 2010. p. 199-249.

[3] J.D. Majumdar, I, Manna, Introduction to LaserAssisted Fabrication of Materials. In: Majumdar JD, Manna I, editors. Laser-Assisted Fabrication of Materials. Berlin, Heidelberg: Springer Berlin Heidelberg, (2013) 1-67.

[4] S. Williams, W, Suder, Use of fundamental laser material interaction parameters in laser welding. CLEO: 2011 - Laser Science to Photonic Applications, (2011) 1-2.

[5] J. Lu, V. Kujanpää, Review study on remote laser welding with fiber lasers, Journal of Laser Applications, 25 (2013) 052008.

[6] D. Havrilla, Laser Based Manufacturing in the Automotive Industry. 2010.

[7] G. Davies, Chapter 3 - Materials for consideration and use in automotive body structures. In: Davies G, editor. Materials for Automobile Bodies (Second Edition). Oxford: Butterworth-Heinemann, (2012) 93-143.

[8] S. Fujita, D. Mizuno, Corrosion and corrosion test methods of zinc coated steel sheets on automobiles, Corrosion Science, 49 (2007) 211-9.

[9] L. David, Greene, H. Howard, J.S.E.P. Baker, Reducing Greenhouse Gas Emissions From U.S. Transportation, (2011).

[10] K. Martinsen, S.J. Hu, B.E. Carlson, Joining of dissimilar materials, CIRP Annals, 64 (2015) 679-99.

[11] A.W. Alshaer, L. Li, A. Mistry, Understanding the effect of heat input and sheet gap on porosity formation in fillet edge and flange couch laser welding of AC-170PX aluminum alloy for automotive component manufacture, Journal of Manufacturing Science and Engineering, 137 (2015) 021011-13.

[12] R. Roth, J. Clark, A. Kelkar, Automobile bodies: Can aluminum be an economical alternative to steel? JOM, 53 (2001) 28-32.

[13] W.S. Miller, L. Zhuang, J. Bottema, A.J. Wittebrood, P. De Smet, A. Haszler, Recent development in aluminium alloys for the automotive industry. Materials Science and Engineering: A, 280 (200) 37-49.

[14] J. Matsumoto, H. Mochizuki, Spot welding of aluminium alloy - electrode life for various electrodes, Welding International, 8 (1994) 438-44.

[15] H. Aydin, E. Essadiqi, I.H. Jung, S. Yue, Development of 3rd generation AHSS with medium Mn content alloying compositions, Materials Science and Engineering: A, 564 (2013) 501-8.

[16] M. Liu, Y. Guo, J. Wang, M. Yergin, Corrosion avoidance in lightweight materials for automotive applications, npj Materials Degradation, 2 (2018) 24.

[17] C.E. Mohammad Darvish, G. Evgeny, M. Holger, O. Andreas, Advantages of three-focal fiber technology in laser brazing of galvanized steel, Lasers in Manufacturing Conference (2017).

[18] G. Filliard, M.E. Mansori, M.D. Metz-Noblat, C. Bremont, A. Reullier, L. Tirado, Influence of process parameters on thermal cycle and intermetallic compounds formation in high speed laser weld-brazing of aluminium-steel angle joints, Procedia Manufacturing, 26 (2018) 690-9.

[19] S. Frank, Flux-free laser joining of aluminum and galvanized steel. Journal of Materials Processing Technology, 222 (2015) 365-72.

[20] G. Yang, J. Ma, B. Carlson, H.P. Wang, R. Kovacevic, Effect of laser beam configuration on microstructure evolution and joint performance in laser joining AA 6111 panels, Materials & Design, 123(2017) 197-210.

[21] M. Sokolov, A. Salminen, Methods for improving laser beam welding efficiency. Physics Procedia, 56 (2014) 450-7.

[22] G.M. Grigorenko, Y.M. Pomarin, V.Y. Orlovsky, Theoretical and experimental investigation of the thermodynamic and kinetic nitrogen absorption by liquid alloys, Materials Science Forum, 318-320 (1999) 25-30.

[23] M. Zhang, G. Chen, Y. Zhou, S. Liao, Optimization of deep penetration laser welding of thick stainless steel with a 10kW fiber laser, Materials & Design, 53 (2014) 568-76.

[24] P. Wang, X. Chen, Q. Pan, B. Madigan, J. Long, Laser welding dissimilar materials of aluminum to steel: an overview, International Journal of Advanced Manufacturing Technology, 87 (2016) 3081-90.

[25] S. Yan, Z. Hong, T. Watanabe, T. Jingguo, CW/PW dual-beam YAG laser welding of steel/aluminum alloy sheets, Optics and Lasers in Engineering, 48 (2010) 732-6.

[26] J.L. Murray, Fe–Al binary phase diagram, in: H. Baker (Ed.), Alloy Phase Diagrams, ASM International, Materials Park, OH, USA, 1992, p. 54.

[27] Y. Miyashita, Y. Mutoh, M. Akahori, Okumura, H.I. Nakagawa, Laser welding of dissimilar metals aided by unsteady thermal conduction boundary element method analysis, Welding international, 19 (2005) 687-696.

[28] H. Springer, A. Kostka, E. Payton, D. Raabe, A. Kaysser-Pyzalla, G. Eggeler, On the formation and growth of intermetallic phases during interdiffusion between low-carbon steel and aluminum alloys. Acta Mater. 59 (2011) 1586–1600.

[29] M. Heitmanek, M. Dobler, M. Graudenz, W. Perret, G. Göbel, M. Schmidt, Laser brazing with beam scanning: experimental and simulative analysis, Physics Procedia, 56 (2014) 689-98.

[30] D. Donst, P. Abels, M. Ungers, F. Klocke, S. Kaierle, On-line quality control system for laser brazing, International Congress on Applications of Lasers & Electro-Optics, (2009) 420-9.

[31] S. Kimura, S. Takemura, M. Mizutani, S. Katayama, Laser brazing phenomena of galvanized steel and pit formation mechanism, International Congress on Applications of Lasers & Electro-Optics, (2006) 528.

[32] M. Gatzen, T. Radel, C. Thomy, F. Vollertsen. Wetting behavior of eutectic Al–Si droplets on zinc coated steel substrates, Journal of Materials Processing Technology, 214 (2014) 123-31.

[33] M. Dal, R. Fabbro, An overview of the state of art in laser welding simulation, Optics & Laser Technology, 78 (2016) 2-14.

Chapter 2

EFFECT OF DUAL LASER BEAM ON DISSIMILAR WELDING-BRAZING OF ALUMINUM TO GALVANIZED STEEL

2.1 Introduction

To control global warming, the U.S. Environmental Protection Agency requires significant improvements in fuel efficiency. One of the best solutions to attain this requisite is to reduce the car's weight by fabricating light weight alloys like Al materials. Nevertheless, to maintain car crashworthiness, aluminum alloys can substitute for steel structures to only some extent. Thus, hybrid steel-aluminum structures have been introduced as a good replacement for many common all-steel body structures, making the joining of aluminum to steel inevitable [1]. Regarding the joining of multi-component structures, the conventional joining processes have been studied and developed, including mechanical joining with rivets or screws, adhesive bonding, friction stir welding, explosive welding, and fusion welding [2]. Restrictions like slower assembly cycle and visibility of the rivets has made mechanical joining undesirable specifically in shell parts [3]. Solid state welding processes are extremely limited to the shape and size of joints so that only simple geometries such as butt and overlapping can be joined [4]. On the other hand, fusion welding of such dissimilar metals has posed many issues due to existence of significant differences between Fe and Al. The zero solid solubility of Fe and Al caused the development of undesirable brittle intermetallic compounds (IMCs) along the interface. It has been shown that an IMC layer with higher thickness reduces the strength of the joint significantly because of its low stress intensity factor as well as high crack propagation rate [5]. However, it was reported that the formation of IMC is useful to improve the wettability between Al and Fe, and good mechanical properties can

be achieved if the thickness of the IMC layer is less than 10 μm [6]. Thus, controlling the formation and growth of the Fe-Al IMCs is the current challenge of joining Al to steel.

In the subcategory of laser joining, a concept of laser brazing was developed for the joining the steel and aluminum panels. Recently the new concept of this process was proposed for the application of dissimilar metals. A liquid/solid state was utilized to join Al-steel where the diffusion of elements through the interface was limited and the reaction rate compared to the liquid/liquid state laser welding was minimized. Based on this concept, considerable attempts have been carried out for joining Al-steel structures by lasers. These studies involved a hybrid welding/brazing with a filler wire in which a fusion welding joint was formed at the aluminum side and a brazing joint was created at the steel side of the weld bead. In this type of joining technology, several solutions have been reported to restrict the growth of IMCs at the aluminum-steel side of the bead to sub-critical values [7]. The process temperature particularly at the interface of Al-steel is shown to have a huge effect on the growth of IMCs. Therefore, monitoring the thermal regime during the process as well as the resulting numerical prediction should be of a great importance. Until now, only very limited literature in the field of numerical simulation models has been proposed to predict the temperature profile during Laser Welding-Brazing (LWB) [8-10]. Mathieu et al. [9] carried out an experimental and numerical approaches to measure temperature during the process. They showed that there was a specific temperate range in which the IMC layer had the greatest rate of growth. Applying the results obtained by numerical simulation, minimizing the process temperature, and process duration made it possible to keep the thickness of the IMC layer below a critical value.

Most studies of the laser joining process have been carried out by using a single laser beam. In some recent studies the advantages of using dual laser beams have reported in laser welding-

brazing processes. Yan et al. [13] observed that application of a dual beam Nd:YAG laser could generate an acceptable joint of steel/aluminum sheets and effectively reduce the presence of blowholes. As shown by Shen et al. [11] a tandem beam used for laser welding of dissimilar titanium alloys had higher strength and elongation than a single beam for laser welding. It was found that the dual-beam LWB compared to a single laser beam improved the process stability. LWB made a visually better-looking weld bead with a larger width. Furthermore, this weld bead increased the shear strength of the joint [12]. Li et al. [13] used cross-beam LWB to join the Zn-coated steel to a Mg alloy in a lap joint configuration. They revealed that the cross-beam mode was superior in reducing the wetting angle and promoting the spread of filler material with respect to the single beam mode.

The coach peel joint, due to the wider space between its panels in comparison to the other types of joints, needed to have a larger laser beam spot to cover the groove appropriately. As the laser spot size increased, the laser power should increase in order to have a high welding speed. To fulfill the requirement of larger beam size, some investigations were carried out recently. Frank S. [14] reported that a combination of continuous and pulsed laser beams in a circular-and-line-shaped mode perpendicular to the weld provided a good wetting at a welding speed of 3.6 m/min. Laserline Company announced a new laser head that generates a triple-spot laser for welding/brazing of similar and dissimilar materials. In this design two smaller laser spots are used to preheat the materials to be welded, and the laser spot in the middle is used to melt the filler material. Another beam arrangement that has good compatibility with the geometry of a coach peel joint is the dual laser beam that has been studied only on welding of similar aluminum [15]. This type of laser beam can deliver wider beams either across the weld groove or along it. To the

best of our knowledge, no research has been published on the dissimilar laser welding-brazing of coach-peel joints by implementing twin-spot laser beams.

However, there has been no comprehensive research done on understanding the correlation between either measured or predicted temperature profiles at the brazed joint interfaces and IMC thickness as well as joint mechanical properties at an elevated scanning speed. In this study, a high speed LWB process by means of two types of dual laser beam arrangement modes (cross and in-line) to join aluminum alloy to galvanized steel (hot-dip and electrogalvanized) in a coach-peel configuration was conducted. The surface quality of the obtained beads and the effect of IMC layer thickness on mechanical properties of the joint were also investigated. Furthermore, a method for measuring weld edge straightness was developed which is significant as straightness defines the quality of transition from the weld surface to the base metal. Finally, the numerical simulation using commercial software ANSYS was proposed to predict the temperature regime through either a weld or brazed interface.

2.2 Experimental procedure

The base metal used in this study was a 1.2 mm thick aluminum 6022 alloy coach peel panel and two types of galvanized low carbon steel coach peel panels with a thickness of 0.65mm (Hot-dip galvanized steel (HDG) and electro-galvanized steel (EG)). The filler wire used in this study was Al4047 with 1.6 mm in diameter. The chemical composition of materials are listed in Table 2.1.

Table 2.1 Chemical composition of materials used.

Substrates and filler wire	Alloying elements								
Element	Si	Fe	Mn	Cu	Mg	Zn	Ti	Cr	Al
Al 6022	0.8-1.5	0.05-0.2	0.02-0.1	0.01-0.11	0.45-0.7	0.25	0.15	0.1	Bal.
Al 4047	12.55	0.43	0.18	0.05	0.05	0.1	0.1	-	Bal.
Element	C	Al	Mn	P	Si	S	Fe	Zinc layer THK (μm)	
Low carbon steel	0.003	0.034	0.11	0.01	0.005	0.05	Bal.	HDG 8-10 EG 12-16	

An IPG fiber laser of 4 kW in power was used to carry out the welding of dissimilar materials (Al to steel). A brazed coupon is shown in Figure 2.1. The dual laser beam modes (cross-beam and in-line beam) were used with respect to the center of joint, and a schematic diagram of dual beams are shown in Figure 2.2. To obtain a dual laser beam shape, an optical beam splitter was mounted inside the laser head that split the laser beam in two beams with a power distribution of 50/50 on each side. The generated dual spots had the same diameter of 1.45 mm at the defocused plane and generated beams that had a 22.66% overlap of the spot. In an experimental setup, a laser head and Binzel wire feeding system were mounted on a 6-axis KUKA robot. The shielding gas used to protect the molten pool from an ambient atmosphere was pure argon with the flow rate of 25 SCFH. A schematic view of the experimental setup is illustrated in Figure 2.3 with the horizontal distance from the tip of shielding gas tube to the laser beam, the tilt angle of gas shielding tube, and the angle of filler wire. To protect the optics from direct reflections of laser beam, the laser head was also tilted at 5º. All experiments were carried out at a welding speed of 60 mm/s and wire feed rate of 70 mm/s. Because of the differences in beam mode and their energy distribution, the magnitude of optimum laser power for dual cross beam and dual in-line beam were selected as 3.2kW and 3.4 kW, respectively.

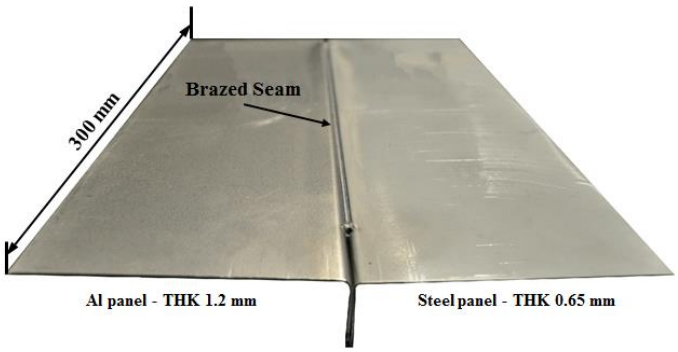

Figure 2.1 Laser welded-brazed coupon in coach peel configuration.

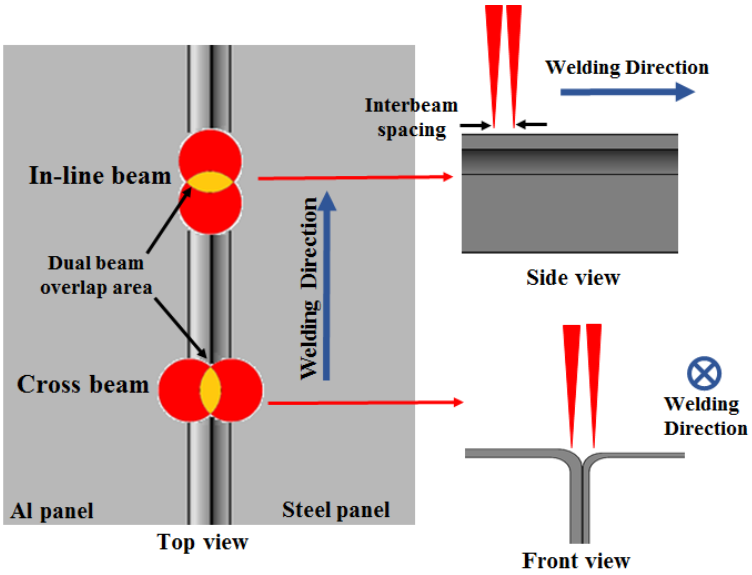

Figure 2.2 Schematic view of dual beams and their positions with respect to groove center.

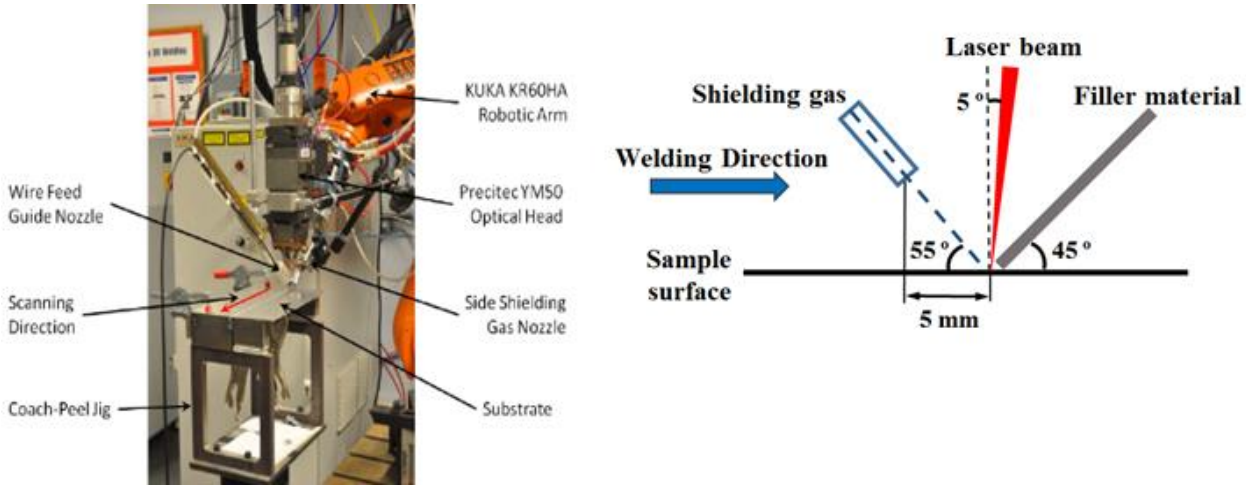

Figure 2.3 The experimental setup and schematic view of arrangements.

To obtain thermal cycles around the bead at both sides of Al and steel, the number of thermocouples were mounted close to the welded/brazed area. The temperature along the bead was measured by K-type thermocouple. The National Instruments data acquisition system was used to capture temperature at every 0.1 s. To quantify the surface roughness of the obtained beads, the surface profile of the bead was measured by the Micro Photonic Nanovea ST400/3D non-contact profiling device to ensure the surface roughness of the bead would be in an acceptable range. To obtain more reliable data, each measurement was reported three times for each laser welded/brazed joint, and the average was reported as the surface roughness. The edge straightness was another parameter that was measured by Keyence VR-3100 to get the edge waviness of the beads generated along the steel and aluminum panels. To acquire coupons for doing characterization and tensile tests, a water-jet cutting machine (integrated Flying Bridge Water-jet 4400, Flow International) was used. The typical sample prepared for tensile test is shown in Figure 2.4. Inspection of microstructure analysis of the joint cross sections was carried out by an optical microscopy and scanning electron microscopy (SEM) equipped by energy dispersive spectroscopy (EDS). The transverse cross section was mechanically polished using different grit sizes of sand paper (120 to 2000). Before the final polishing with 0.04 μm Al_2O_3 particle suspensions, the samples were polished with a diamond paste of different particle sizes, 9, 6, and 1 μm. The polished cross sections were etched with a double etching process, first immersed in C_2H_5OH-5%HNO_3 solution for 5s and then a solution made of 1ml HF +1.5 ml HCl + 2.5 ml HNO_3 +95 ml H_2O was used to reveal the general microstructure of steel and aluminum respectively.

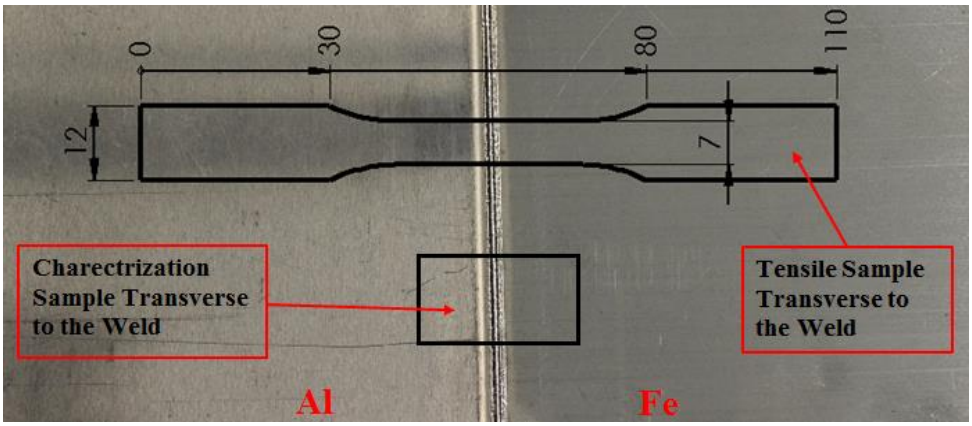

Figure 2.4 The specimen prepared for tensile test (dimensions are in mm).

2.3 Finite element modeling

2.3.1 Assumptions and Governing equations

The goal of the finite element method was to obtain the temperature history during the LWB process. The actual process dealt with many parameters to simplify the FE model that didn't affect the accuracy of simulation results. Therefore, the following assumptions were considered in the finite element thermal analysis of LWB of joining galvanized steel sheet panels to aluminum panels in a coach peel configuration:

1. The pre-constructed geometry of the joint was fixed before laser radiation.
2. The substrates and bead obtained by filler wire were taken into account as isotropic without considering the fluid flow of molten material and its spreading.
3. The applied heat from laser irradiation followed a double rotary Gaussian distribution.
4. The effect of shielding gas on heat input was neglected.
5. The influence of zinc layer on the thermal properties of weld zone was ignored.

Due to the nonlinear transient nature of the LWB process and severe change of thermal as well as physical properties of the utilized materials, the differential equation of thermal conduction was applied:

$$\rho \frac{\partial (C_p T)}{\partial t} = k \left(\frac{\partial^2 T}{\partial^2 x} + \frac{\partial^2 T}{\partial^2 y} + \frac{\partial^2 T}{\partial^2 z} \right) + \dot{q}_{laser}(x, y, z, t) \quad (2\text{-}1)$$

where, $\rho, C_p, \mathrm{T}, \mathrm{t}, k$ and x, y, z were the material density, specific heat, temperature, time, thermal conductivity, and Cartesian coordinates, respectively. For moving the heat source model, the laser induced volume heat source was described by the following equations for dual cross and in-line laser beams (see Figure 2.5) [16].

$$\dot{q}_{laser}(cross\ beam) = \frac{9\eta Q}{\pi H {R_0}^2 (1 - e^{-3})} \exp\left(\frac{-9}{{R_0}^2 \ln\left(\frac{H}{-y}\right)} ((x - x_0 \pm d)^2 + (z - vt)^2) \right) \quad (2\text{-}2)$$

$$\dot{q}_{laser}(In\ line\ beam) = \frac{9\eta Q}{\pi H {R_0}^2 (1 - e^{-3})} \exp\left(\frac{-9}{{R_0}^2 \ln\left(\frac{H}{-y}\right)} ((x - x_0)^2 + (z - vt - d)^2) \right) \quad (2\text{-}3)$$

where η was the absorption coefficient, Q was the nominal power of the laser beam, y varied from 0 to H, H was the depth of the fusion zone, v was the welding speed, R_0 was the effective radius of the volumetric heat source on the material surface, and d was the center distance of dual beams.

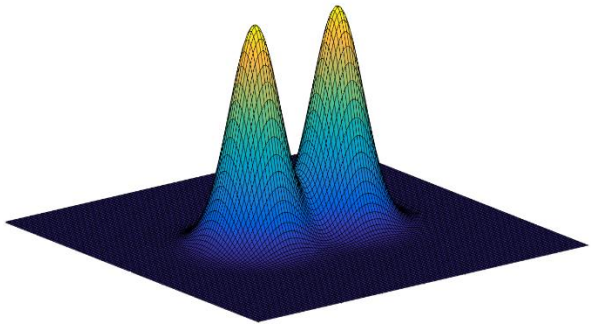

Figure 2.5 Laser power density distribution in dual-beam mode.

when t=0 the initial temperature of specimen is uniform and equal to ambient temperature ($T=T_0=20^{\circ}C$). Due to the geometry of dissimilar joints, the symmetry boundary condition was not considered in simulation, and the natural boundary condition on the panel surfaces could be represented as:

$$k\frac{\partial T}{\partial n} - q_s + h(T - T_0) + \sigma\varepsilon(T^4 - T_0^4) = 0 \quad (2\text{-}4)$$

where k, q_s , h, σ, ε and T_0 were the thermal conductivity, imposed heat flux, convection heat transfer coefficient, Stefan-Boltzmann constant, emissivity, and ambient temperature, respectively. Since the Eq. (2-4) is non-linear, in order to simplify the boundary calculation and avoid its nonlinearity"a lumped heat transfer coefficient" was considered in this simulation. This lumped coefficient considered heat loss due to convection and radiation that can be presented as Eq. (2-5) [17].

$$h_{eff} = 2.4 \times 10^{-3} \times \varepsilon \times T^{1.61} \quad (2\text{-}5)$$

2.3.2 Numerical procedure

The dimensions of the model of dissimilar laser welded/brazed joint are shown in Figure 2.6. Implementing the non-uniform finite element mesh in thermal modeling of the LWB process due to unsymmetrical structure of fabricated joints is the only way to have less computational time. A sufficiently fine mesh was applied in the regions near the weld zone to obtain more realistic results. SOLID70 was selected as a parent element for meshing the model, and the sizes of the elements were refined several times in order to get a converged solution (element size independent results). The optimum number of elements in this investigation was 248784 elements, and the sizes of smallest element that was employed near the weld zone had dimensions of 0.094 mm × 0.073 mm × 0.06mm.

The steps of the simulation process are shown in Figure 2.7. The geometry of panels and bead were built up in the coach peel configuration. It is worth noting that the dimensions of the welded bead were measured from the actual cross sections of the bead. The "kill and birth" technique was implemented in the FE model to simulate the process of groove filling by melted wire. In this method, first, all the elements defined as filler metal were killed. Consequently the effect of these elements on the simulations results were not applied. By moving the heat source along the joint line, the groove elements were activated step by step with respect to simulation time steps, and the joint bead was formed. The acquired temperature results were more accurate and closer to reality than applying thermal loads directly to nodes and elements without the element activation method. In order to define the material properties, three temperature-dependent thermal properties were selected for the aluminum panel, steel panel, and filler wire as shown in Figure 2.8. Since the welding area experiences the highest thermal gradient during the welding process, the coarse mesh was applied in that region. To obtain the thermal history and temperature profiles, the appropriate thermal boundary conditions and volumetric rotary Gaussian heat source were employed.

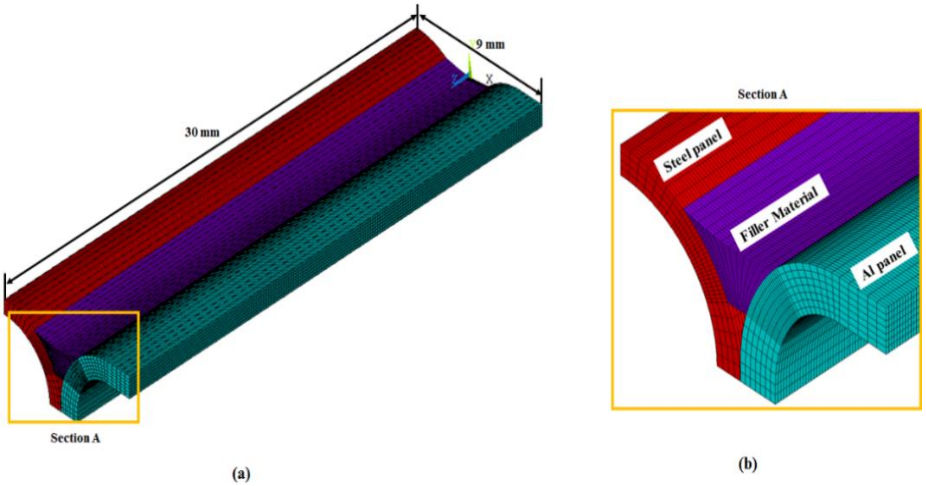

Figure 2.6 Dimensions of Finite element meshed model: (a) general view, (b) close-up of weld zone.

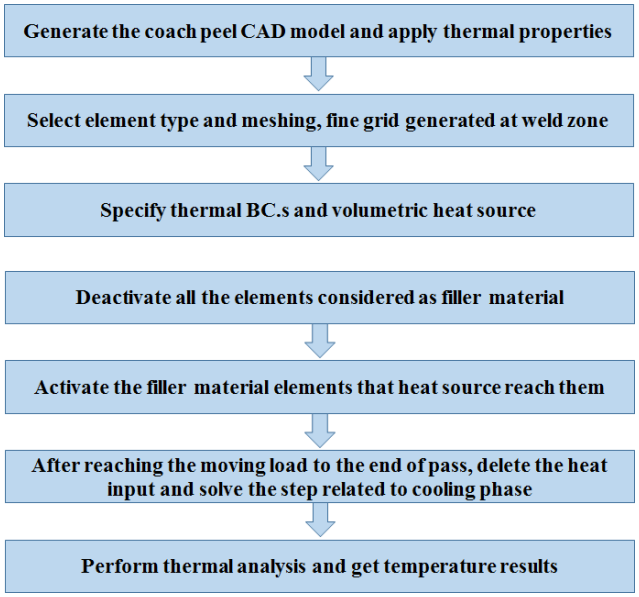

Figure 2.7 Flowchart of extraction of meshed model from the cross section of an actual joint as well as the numerical simulation procedure.

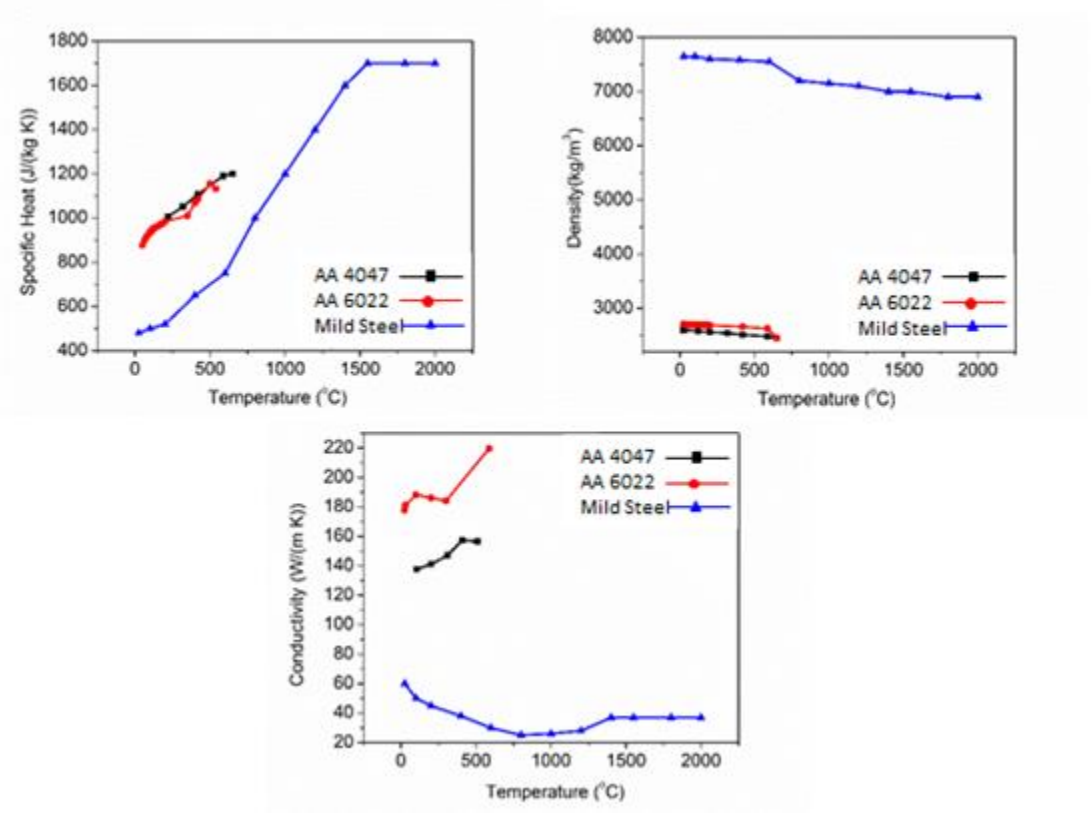

Figure 2.8 Thermo-physical properties of galvanized steel, aluminum alloy and filler wire as a function of temperature [15, 18].

2.4 Results and discussion

2.4.1 Microstructural characterization

The process parameter optimization for a coach peel joint configuration was conducted for the two types of laser beam modes with a combination of Al 6022 panels and two types of steel panels. The criteria for a sound joint was high surface quality of the top side of the bead and not re-melted on the back side of the panels. In keeping these criteria, several single-factor optimizations were done. The best result was achieved with a scanning speed of 3.6mm/min, wire feed rate 4.2mm/min, and laser power of 3.2kW and 3.4kW, respectively for cross- and in-line dual beams.

The cross-sectional view of the joint obtained by a cross-beam laser mode showed a good quality that was free of pores (Figure 2.9). It can be seen that the process temperature was not high enough to melt the steel panel. However, the aluminum panel was melted, and that result is why the terminology of laser welding/brazing is used in dissimilar joints. The dilution of wire with aluminum substrate was evident particularly at the top side of the interface. Thus, the result was the welding and aluminum mixture with Al-Si wire along with brazing of the steel to the in-situ-formed Al-Si-Fe alloy. In addition, the welded/brazed bead showed two different microstructures in different zones that were recognizable after etching. In order to study the details of the top and bottom areas of the bead, optical micrographs of these two zones were captured at higher magnifications as shown in Figure 2.9. The microstructure at the upper region consisted of α-Al solid solution dendrites at various growth directions and short rod-like Al-Si eutectics in the grain boundaries. On the other hand, the lower region of the brazed bead was composed of an almost-intact microstructure of the wire containing the small Al grains with dispersed Si particles. Whereas in the in-line beam joints, the same microstructure was present throughout the weld area

from top to bottom, including the solidification-induced large Al dendrite. It is noteworthy that the dendrite size was finer at the top side as shown in Figure 2.10. In contrast to a dual-cross beam configuration, the laser power distribution in a dual in-line shape was highly concentrated inside the groove of the joint instead of the adjacent surfaces of the substrates. Specifically, the wire went through re-melting and solidification in two sequences. As a result, the depth of penetration was increased slightly higher than was found for the dual cross-beam shape. In addition, the two-sequential solidification improved the homogeneity of microstructure; the morphology of the Al dendrites was almost uniform throughout the bead. The distinct microstructures illustrate the various thermal regimes experienced by the bead at different locations due to a difference in beam configuration.

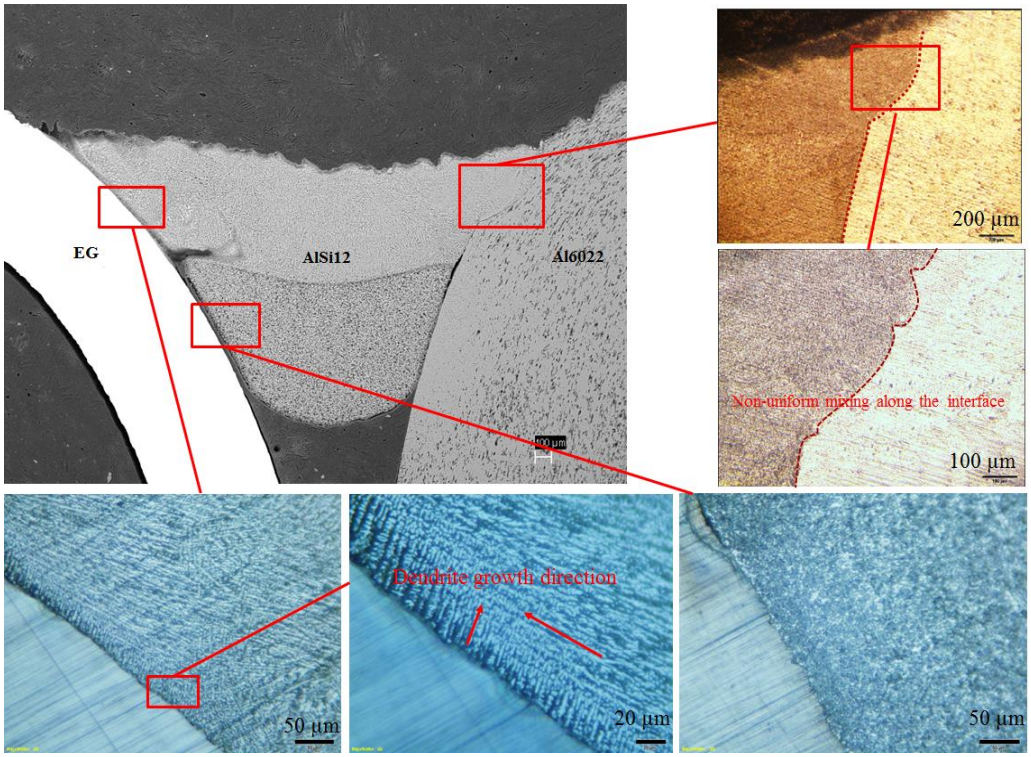

Figure 2.9 Microstructure of the LWB joint in cross-beam mode at different magnifications.

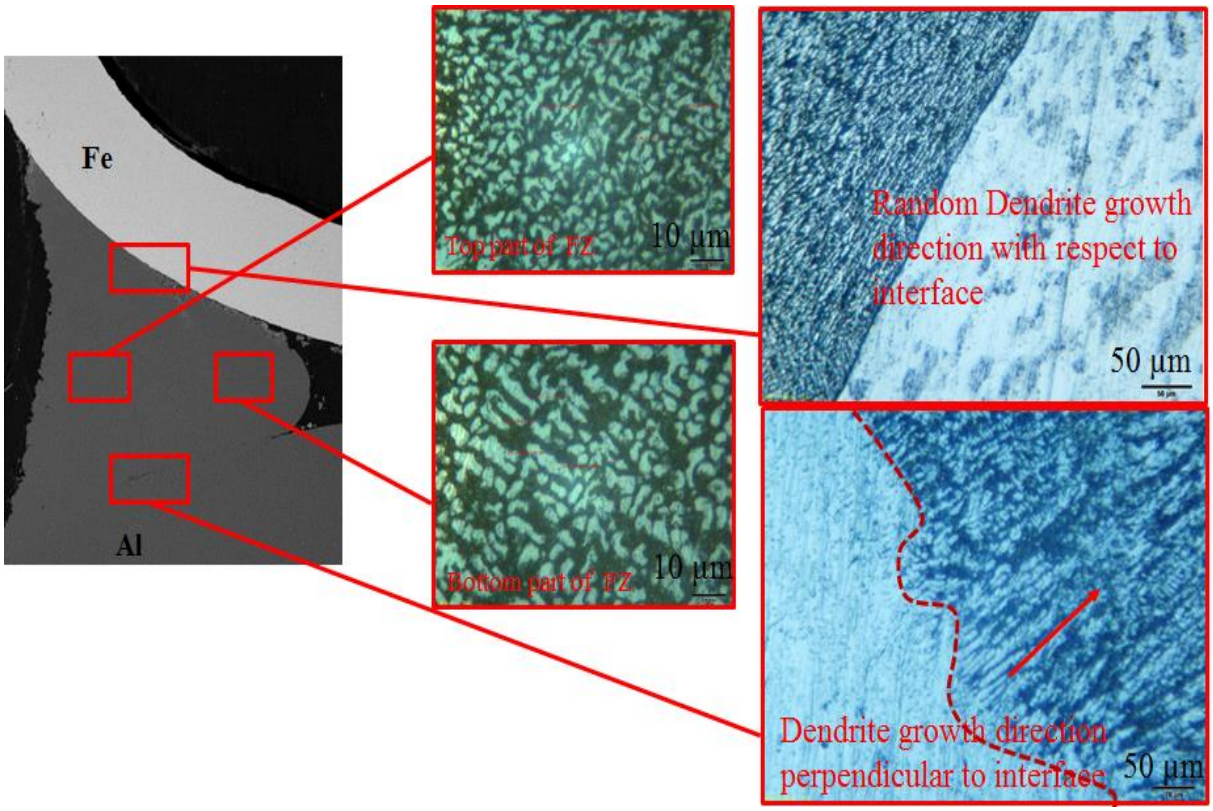

Figure 2.10 Microstructure of the LWB joint in in-line mode at different magnifications.

Since the thickness of the generated intermetallic layer (IMC) was not uniform (Figure 2.11) the steel/bead interface was measured by SEM at different locations. A distinct IMC layer was not detected at the corners of the seam, while its thickness became maximum in the middle section. Similar observation was reported by Fillard et al. [19] proved that the thickest IMC layer generated in the middle section of brazing interface. The maximum values of IMC thickness for all types of joints are summarized in Table 2.2. The values were far from the reported critical value of (10 µm) in literature [6]. SEM equipped by EDS analyzer was utilized to know the chemical composition of the dilution layer based on the distribution of elements through the steel/bead interface. Figure 2.12 presents the interfacial microstructure of the laser-brazed joint as well as the EDS line scan across the interface for sample joints of dual in-line and cross-beam modes.

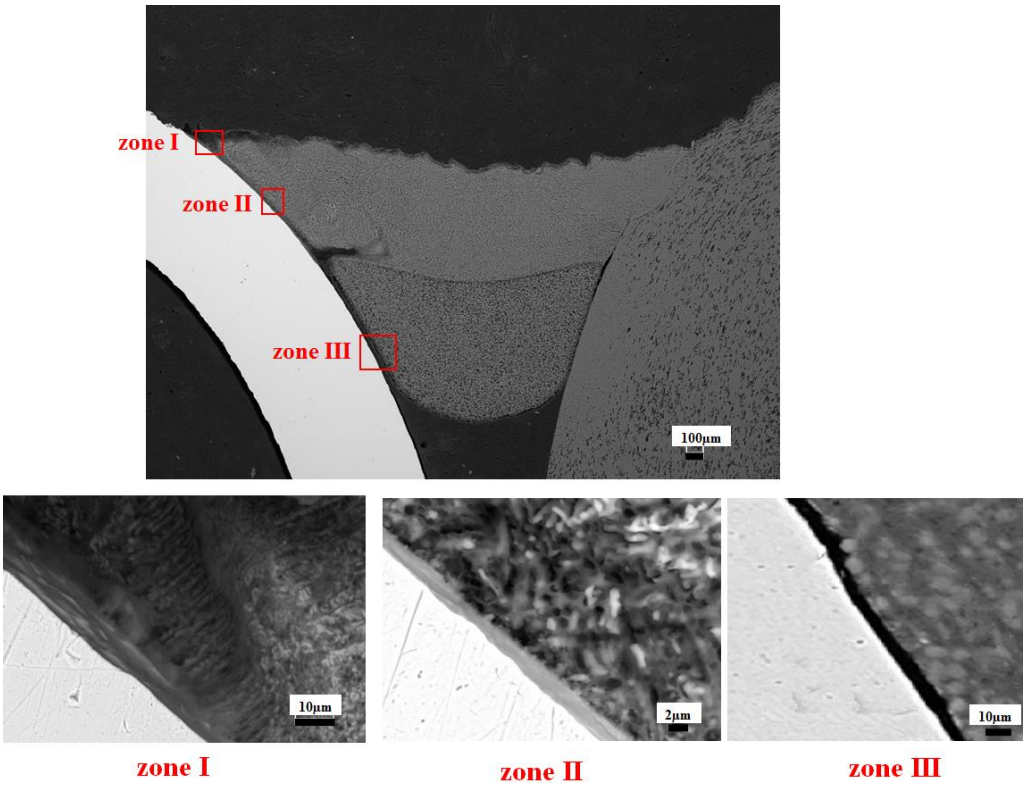

Figure 2.11 The measured thickness of IMC layer for cross-beam joint.

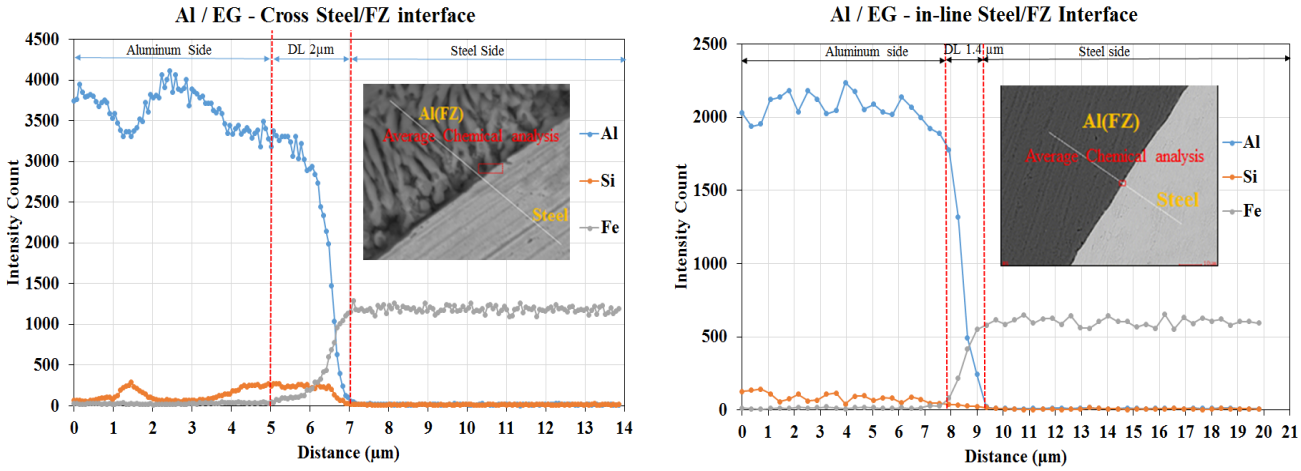

Figure 2.12 SEM image of brazed bead-steel interface and EDS line scan across the interface: (a) Al / EG - in-line, (b) Al / EG – cross.

Table 2.2 Metallurgical features of possible IMC compound based on the EDS analysis of the interface of steel-Al for all LBW joints in atomic percent.

Welding/brazing joint type	Dilution layer thickness	Al	Fe	Si	Possible IMC type
Al / EG - cross	2 µm	73	15	10	Al_7Fe_2Si
Al / HDG - cross	1.6 µm	72	16	11	Al_7Fe_2Si
Al / EG – in-line	1.4 µm	86	9	5	Al(Fe)
Al / HDG – in-line	1 µm	84	8	8	Al(Fe)

Based on the ternary Al-Fe-Si phase diagram (Figure 2.13), the possible intermetallic phases developed during laser brazing could be Al_7Fe_2Si, Al_9Fe_2Si, and $(Al,Si)_7Fe_2$ [20, 21]. Based on the atomic percent of the elements distributed at the interface, it was observed that in joints obtained by the cross-beam mode, the possible present phase should be Al_7Fe_2Si. Whereas for the in-line beam mode, the dilution layer was so thin, it seemed that IMC could not form. Formation of this type of IMC could be explained by its formation enthalpy and decomposition temperature. It was reported that formation enthalpy of IMC at 298K was one of the key indicators to predict the formation of IMC [22, 23]. The thermodynamic data for possible IMCs that could be formed in the brazing process of Al-steel are summarized in Table 2.3. Among three IMCs, the Al_7Fe_2Si had the lowest decomposition temperature and formation enthalpy. Regarding the focused and much lower heat input obtained by laser, the formation feasibility of Al_7Fe_2Si was thermodynamically favorable compared to the other binary Al-Fe IMCs. In other words, Si pile up at the Al-steel interface and its participation in the formation of IMC layer reduced the formation enthalpy of the IMC layers at much lower temperatures.

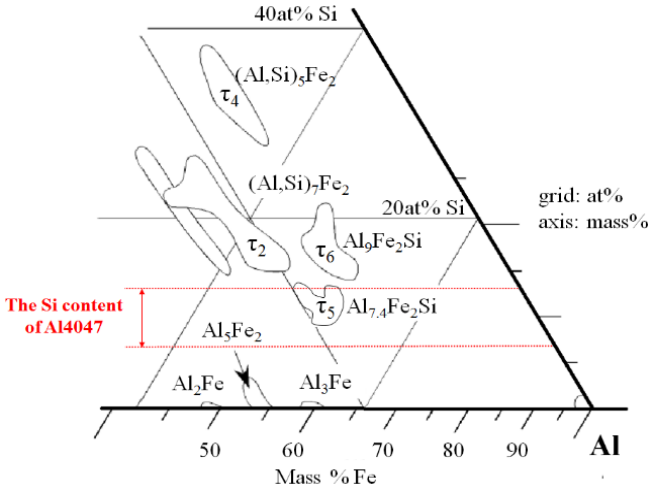

Figure 2.13 Equilibrium AL-Fe-Si ternary phase diagram in the aluminum corner presenting distribution of IMC phase [21].

Table 2.3 Thermodynamic data for a number of IMCs formed in Al-Fe and Al-Fe-Si system [21, 22]

IMC phase type	Al_5Fe_2	Al_3Fe	Al_7Fe_2Si
$\Delta H_{formation}$ (kJ/mol)	-28.8	-27.8	-34.3
Decomposition Temperature (˚C)	1035	1100	700

As mentioned previously, a thin IMC layer was formed at the steel/bead interface for both beam configurations. It was reported that the solid-state diffusion coefficient of Fe through the Si-rich ternary AlFeSi IMC is much smaller with respect to AlFe binary IMC. Regarding the fact that diffusion of Fe inside the dilution layer is crucial to accelerate its growth, Si pile-up at the interface hinders Fe diffusion and reduce the growth rate of dilution layer significantly [21]. This thinner layer could be attributed to the application of a high welding speed that limited the heat input to the steel substrate. Although the laser power used for the in-line beam was slightly higher than for the cross-beam, the thickness of the dilution layer in the in-line beam was less than that of the cross beam. This phenomenon can be related to the shape of the laser beam applied and its energy density, because in the in-line beam, the amount of surrounding substrate that received the

laser energy was smaller. In other words, in cross-beam mode the laser spot covered a larger surface of substrate on both sides. Due to the nature of LBW, with concentrated heat input and application of a high welding speed, a very high cooling rate could be expected. This rate would also be the main reason to restrict the excessive growth of IMC.

According to the results of Table 2.2, electro-galvanized steel (EG) with a larger zinc-layer thickness resulted in a slightly thicker interfacial layer compared to the hot-dip galvanized (HDG) steel. The explanation for such behavior was reported by Gatzen et al. [24]. Reducing the effect of oxide layers that resulted from the participation of the zinc layer with Al during chemical reaction was considered as the main reason to lower the surface tension of the liquid wire and improve wetting. Nevertheless, Zn could accelerate the solid-state diffusion of Fe through the interface that hastened the IMC growth. Dissolution of Zn inside the aluminum lowered the melting temperature of the wire. This lower temperature led to the longer presence of liquid in contact with the steel substrate before solidification. Therefore, it seemed that the presence of zinc coating was necessary as a driving force for wettability. However, the amount of zinc should be controlled to limit the growth of IMC. By studying the spreading behavior of zinc in the molten pool during the laser brazing process, the distribution of this element through the bead was detected by EDS mapping (Figure 2.14) local accumulation of zinc at the outer boarder of the brazed bead was noticeable. It seemed that propagation of Zn liquid toward the bead toe was the main reason for the zinc pile-up in this region. Based on a hypothesis proposed by Agudo et al. [25], fluid dynamic phenomena were the reason for the origination of zinc accumulation at the brazed ends. Implying that dissolved zinc into the liquid Al was being pushed by the newly liquefied Al from the wire.

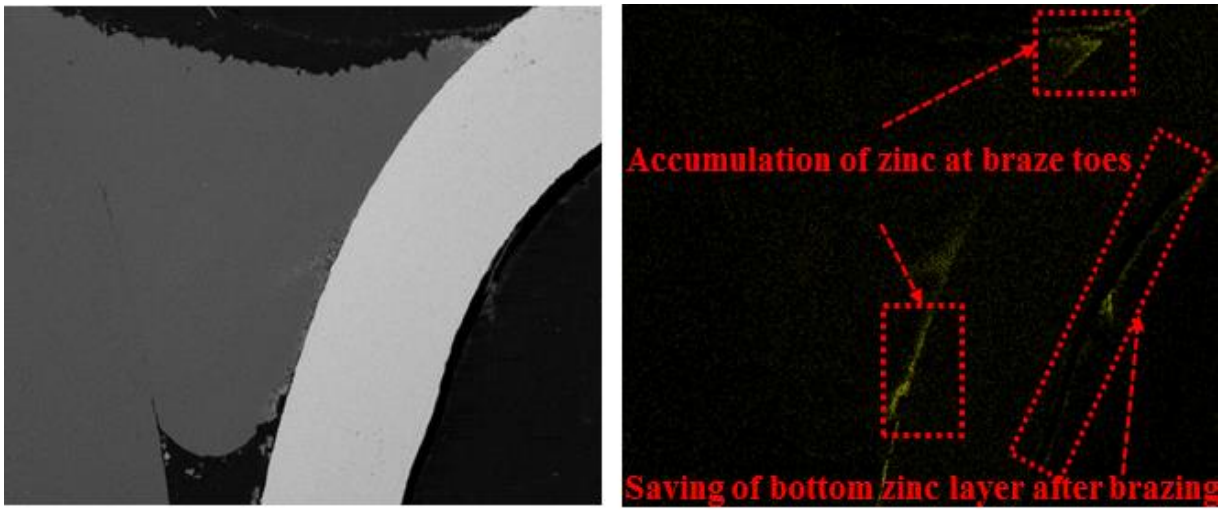

Figure 2.14 EDS map scanning result of zinc distribution at substrate and brazed coat.

2.4.2 Thermal field simulation and experimental validation

The Gaussian rotary heat source was used to simulate the thermal field in dissimilar LWB of galvanized steel and aluminum panels in a coach peel configuration. Figure 2.15 (a-d) depicts the numerically-obtained temperature field of dual cross-beam welded joints at different time intervals. The experimentally-obtained optimum process parameters were applied in the FE model as follows: the laser power Q was 3.2 kW, welding speed v was 60 mm/s, and effective radius of heat source on the bead surface r_0 was 2.5mm. The maximum temperature obtained at all processing times (2280˚C) was far lower than the boiling temperature of steel (2800˚C). The results showed that laser interaction with the surface of the workpiece could be considered as a conduction mode instead of keyhole formation. It can be shown that the higher thermal gradient was located in the center of the groove.

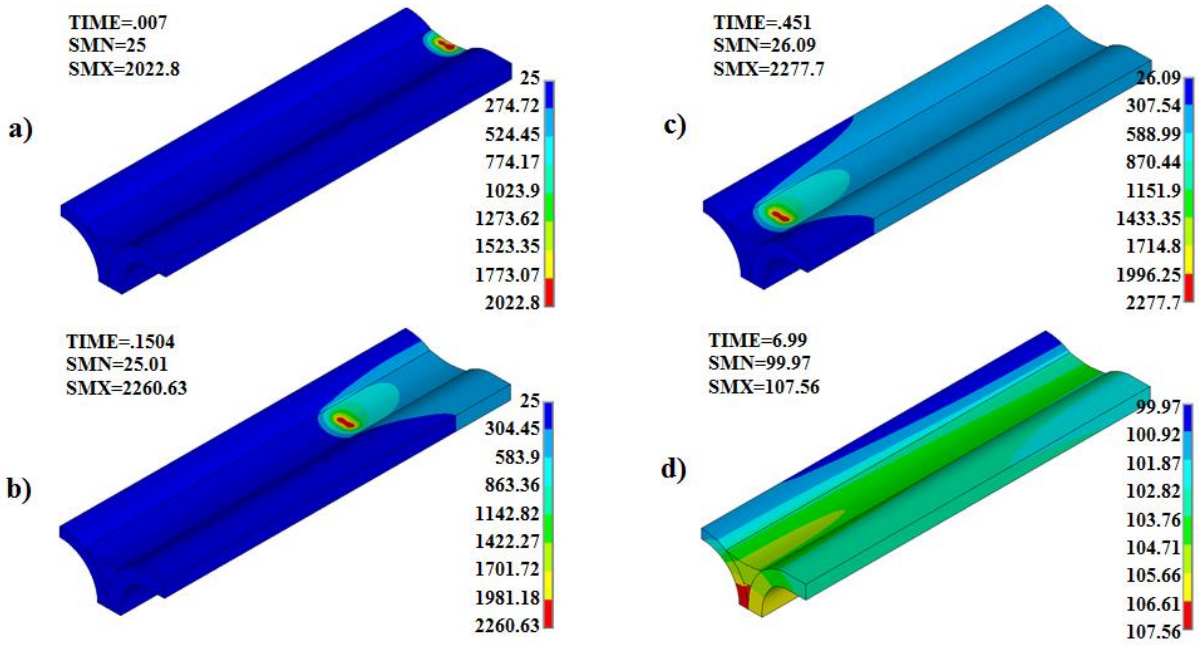

Figure 2.15 Temperature counter history in the joining process: (a) t=0.007 s, (b) t=0.1504 s, (c) t=0.451 s, and in cooling phase (d) t= 6.99 s.

In order to verify the precision of the simulated temperature distribution, the temperature around the weld bead was measured experimentally. The thermal history of the weld obtained by a cross-beam was measured by thermocouples at four points along the weld bead on the aluminum side. The thermal history was then compared to the thermal simulation results. As described in Figure 2.16, there is a good consistency between the thermal cycles obtained from numerical simulation and experimental measurements.

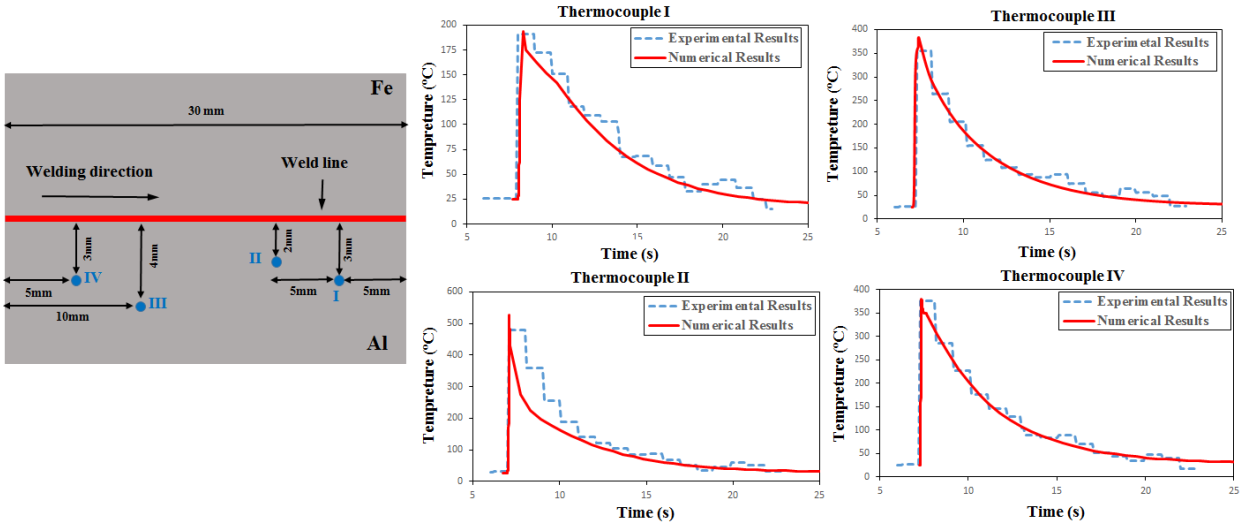

Figure 2.16 Schematic diagram of thermocouple positions and comparison between experimental and simulation results.

The experimentally-obtained and numerically-simulated cross sections of the LWB joint are presented in Figure 2.17. As can be seen, the temperature isotherms that reach the steel-Al interface particularly at the middle region are beyond the melting temperatures of Zn (419˚C) and filler wire of Al4047 (575˚C). This result could confirm the hypothesis that in-situ liquefied Al dissolves and propagates the melted Zn layer toward the outer boundary of the brazed bead. In addition, temperature at the interface of the bead and the steel side was much lower than the melting point of mild steel (1530˚C). This result could affirm the laser brazing nature of the process at the Al-steel interface. The temperature at the interface of the bead and aluminum panel was high enough to melt both materials and caused a kind of weld joint for this type of pair materials. These simulation results were in accordance with the microstructure of filler-Al side indicating that a type of non-uniform interface was produced by the long-distance diffusion of Al and wire into each other. Another key point that should be noticed was the different temperature contours going through the upper and bottom regions of the brazed bead. Relatively elevated temperatures predicted for the top part of the bead confirmed the presence of solidification-induced

Al dendrites found in this area (Figure 2.9). On the other hand, isotherms passing through the downside of the bead were much closer to the melting point of the filler wire, meaning that this part of bead had almost an intact microstructure of filler wire. Hence, it seemed that there was a relatively good agreement between the experimental and simulation results.

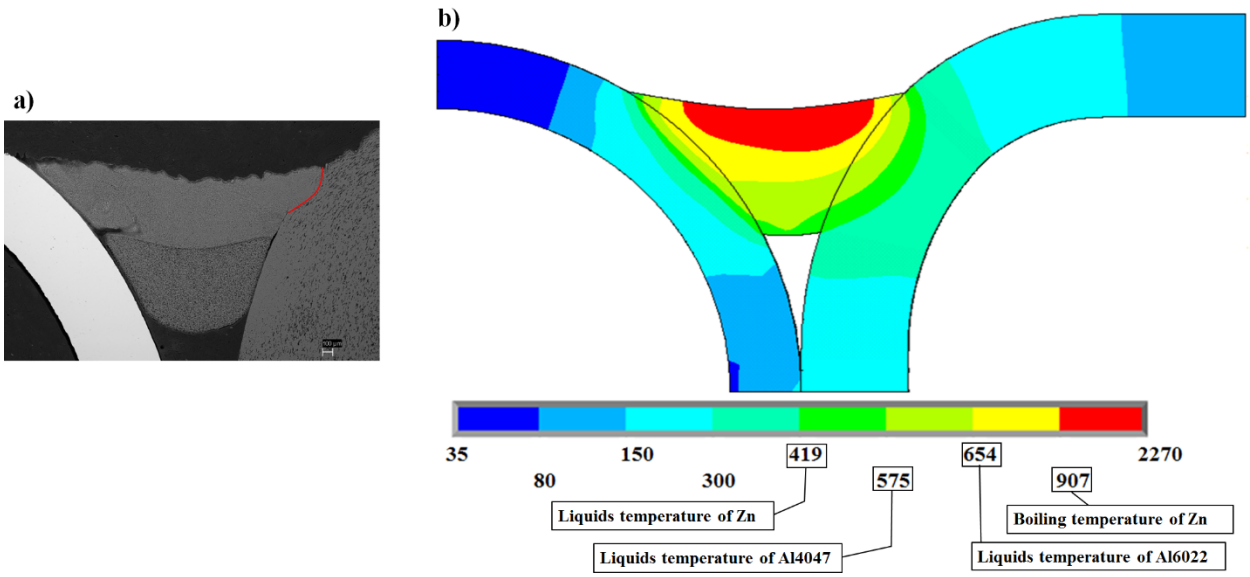

Figure 2.17 Comparison between (a) experimentally and (b) numerically obtained cross-sections by dual cross beam laser mode.

The in-line laser beam was determined by comparing the obtained experimental results with the thermal simulation counters as shown in Figure 2.18. It could be concluded that the fusion size in this mode was larger than in the cross beam. The steel interface area also experienced lower temperature that led to the generation of a thinner IMC layer. Furthermore, the cross mode had a shallower beam with a wider bead area, while the in-line mode covered a smaller bead area with deeper penetration.

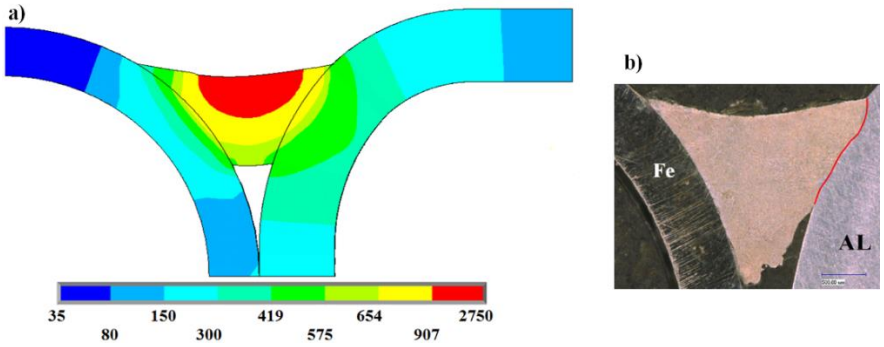

Figure 2.18 Comparison between (a) numerically simulated and (b) experimentally-obtained cross sections by dual in-line laser beam mode.

The most important data extracted from the numerical simulation was the temperature interfacial histories. Following the same procedure, the numerically-computed thermal cycles could be captured in this zone (Figure 2.19). Regarding the temperature range in which aluminum was in the liquid state, the wetting time at the molten aluminum-solid steel interface was less than 1s. These thermal cycles were very short with sharp thermal loadings that implied the reaction control mechanism with respect to diffusion process could be considered as the main mechanism for growth of the IMC layer.

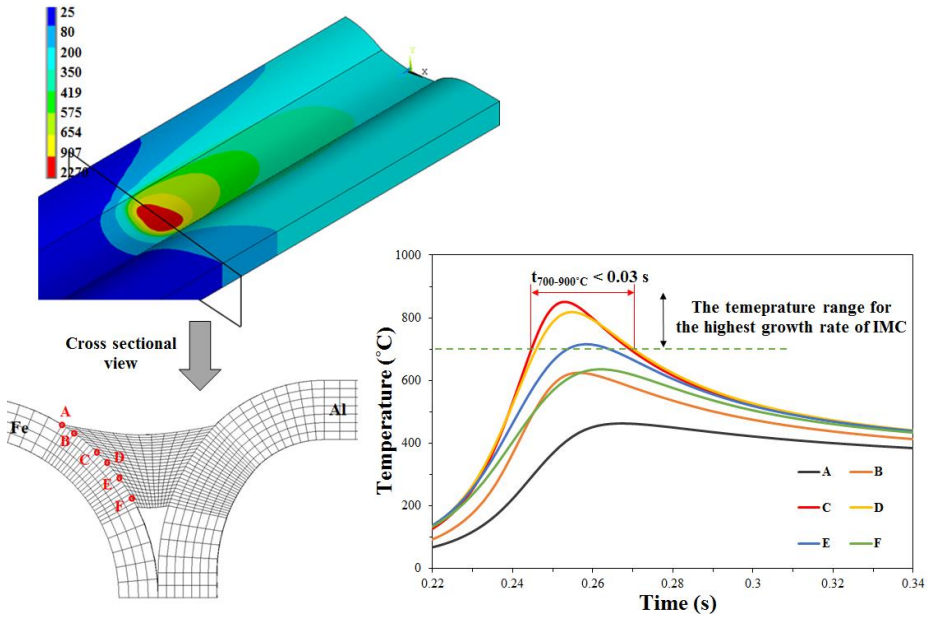

Figure 2.19 Simulated thermal histories at different locations along the brazing interface.

Bouche et al. [26], proposed a kinetic model to explain the mechanism of IMC growth between solid iron and molten aluminum. However, based on this model, the highest growth rate of Fe_2AL_5 and $FeAl_3$, as the two main IMC phases found in Al-Fe binary system, were identified in the temperature range of 700-900˚C and, thus, obeyed the diffusional parabolic law. Based on the predicted and [20, 21] measured temperature of the interface, the kinetic condition for IMC growth through the diffusion mechanism did not exist during the LWB process. Furthermore, Shahverdi et al. [27] reported that the Fe_2Al_5 and $FeAl_3$ formations were the interface reaction's controlled base and diffusion-controlled base, respectively. This result was due to the specific crystallographic nature of these IMCs. This type of IMC produced in the presence of Si had a chemical composition similar to Fe_2Al_5. This result confirmed that once the Al-steel interface interaction was carried out at lower temperatures (<700˚C) and in shorter time (<1s), other IMC besides Al_3Fe could be found [21, 22].

2.4.3 Surface roughness and Edge straightness

The most important features that considered in the evaluation of the brazed joint were surface roughness and edge straightness of the weld bead. The LWB process was the final process without any further post-weld processing required, for the sake of decreasing production time and expense. To compare the weld surface quality of dual in-line and cross beams, two typical shapes of the beads were measured by an optical profilometer (Figure 2.20). The measurements were conducted along the seam. The average as well as standard deviation are given in Table 2.4. According to the obtained results, the best surface quality was obtained by dual cross beams. These results could be attributed to the heat source shape. The cross beam was wider than the diameter of consumable wire that led to preheating the substrate and having better wettability. In the in-line beam, most of the energy was irradiated on filler material without affecting the substrate.

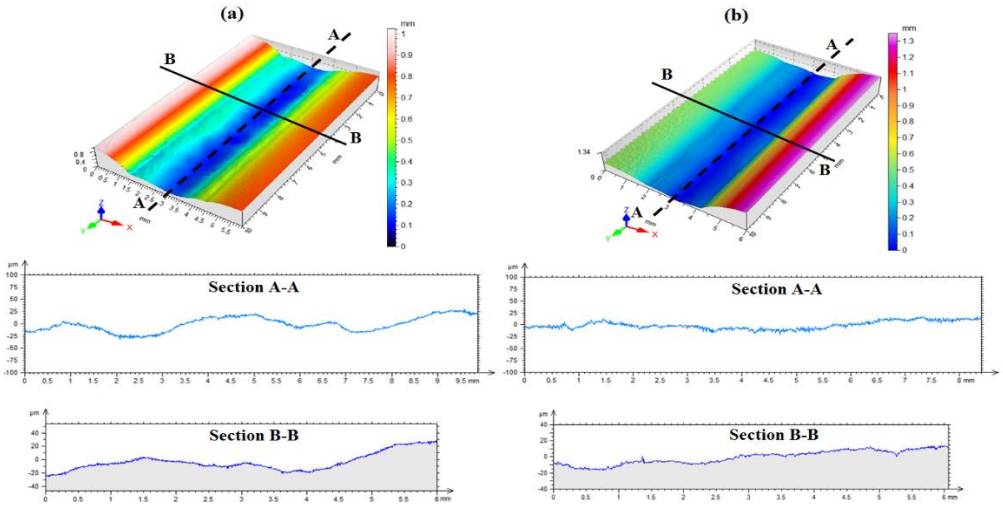

Figure 2.20 3-D view and cross section captured by optical profilometer for the joints: (a) Al / EG – in-line, (b) Al / EG – cross.

Table 2.4 The surface roughness values measured by an optical profilometer.

Panels and laser mode	Surface roughness (Ra) μm	Standard deviation
Al / EG – in-line	1.8	0.07
Al / HDG – in-line	1.3	0.08
Al / EG – cross	1.58	0.51
Al / HDG – cross	0.984	0.19

Edge straightness was the other important indicator to characterize the quality of LWB bead. This characteristic implied that the brazing bead had no irregularities like saw tooth along the edge area of the weld bead. The 'straight' edges give the weld a uniform width appearance. To measure the edge straightness transition point from the weld to the base metal should be identified. In this regard, evenly spaced measurement lines projected on the captured image of brazed seam to obtain the cross-sectional surface profile (see Figure 2.21). To precisely detect the location of transition point, the 2nd order derivative of surface profiles were also obtained. Figure 2.21 depicts the cross-sectional surface profile of seam obtained from the scanned image using the Keyence measurement system.

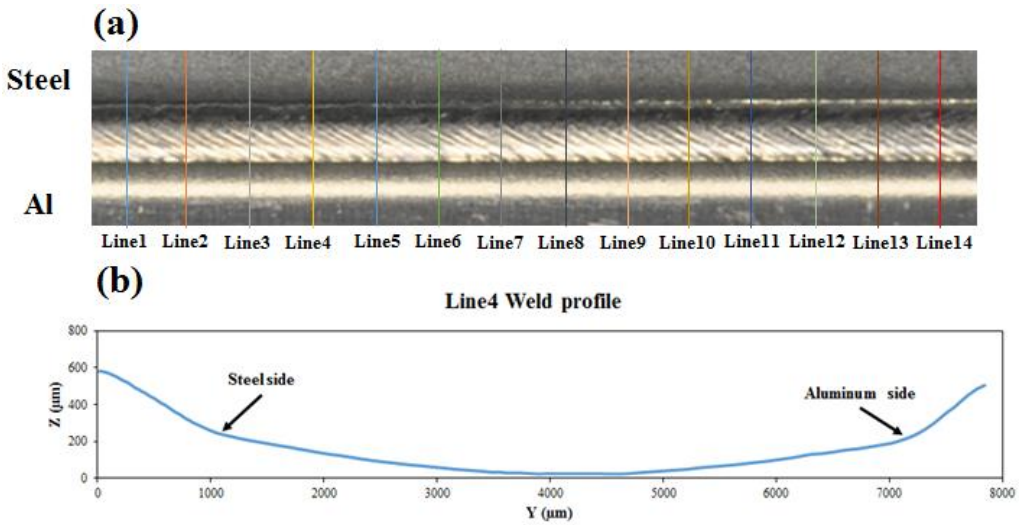

Figure 2.21 (a) Evenly spaced cross-sectional lines on the brazed seam to detect edge transition, (b) weld surface cross-sectional profile.

Figure 2.23 shows the typical coach peel bead surface as well as the variations of edge straightness along the bead for Al-HDG in cross beam mode. The obtained edge locations from each of the 14 cross-sectional lines were employed to plot the dashed black line curves as the edge variation curves for either sides of aluminum and steel. The solid red line corresponds to the least square fit of the deviation curve. The maximum deviation "d" was defined as the distance between the solid blue lines as the boundaries of edge curves. Rayleigh's criteria (2-6) with considering the calculated deviation "d" were used to characterize the weld edge straightness and identify the acceptable deviation level.

$$\theta_{min} = \frac{d}{L} = 1.22\frac{\lambda}{D} \tag{2-6}$$

where, Θ_{min} is the angular resolution of the human eye, d is the minimum distance required between two separate points to be detectable for a given distance, L distance between the eyes and object (two points), λ is the wavelength of light reflected into the eyes, and D is the diameter of the pupil. Figure 2.22 schematically depicts the above-mentioned terminologies.

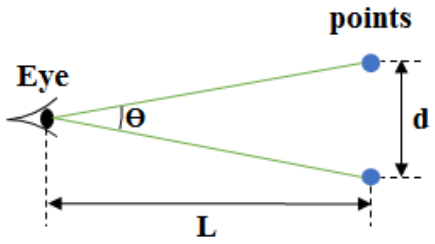

Figure 2.22 Schematic description of Rayleigh's criteria.

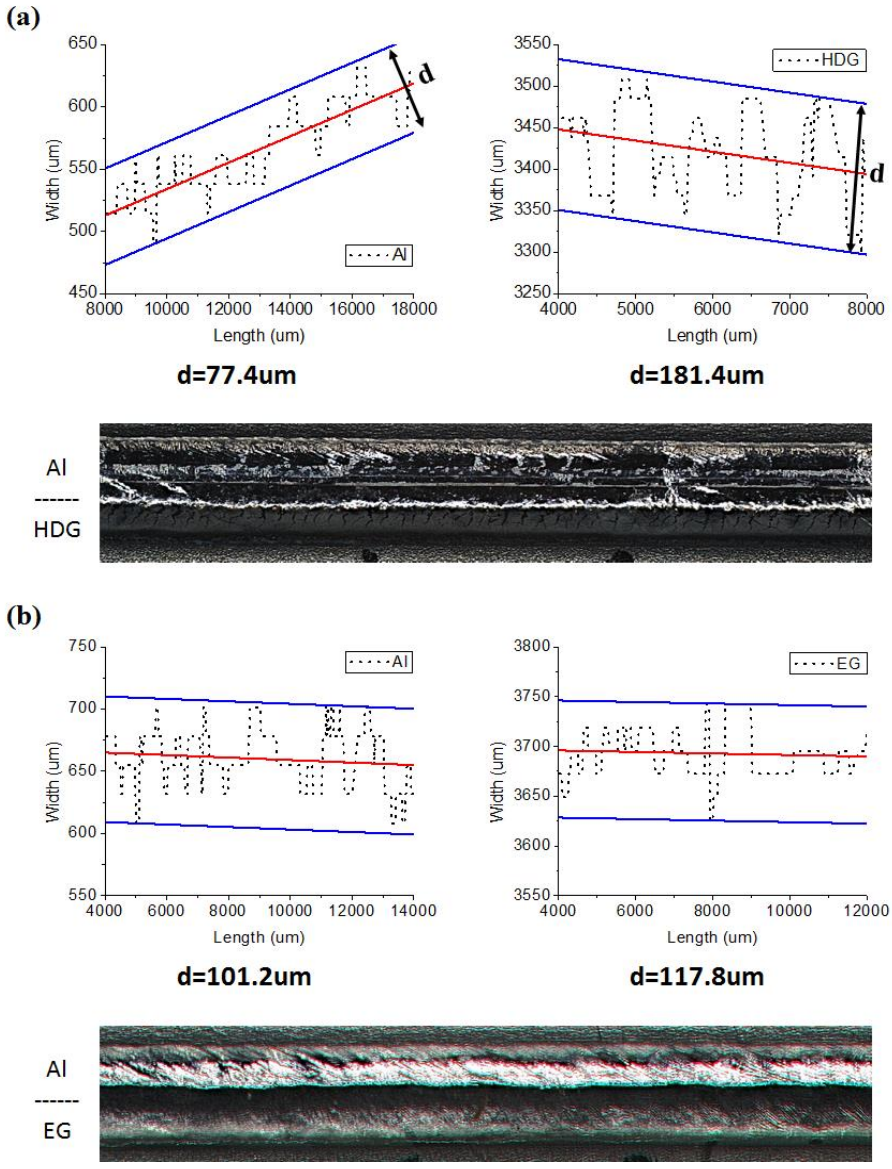

Figure 2.23 The variation of edge straightness along the bead at the Al and steel sides: (a) Al-HDG, (b) Al-EG joints at a cross-beam configuration.

As can be observed, the maximum edge deviation at the steel side is higher than what was measured for the Al side. This deviation was due to the asymmetrical geometry of joints and instability of the molten pool because of the existence of low boiling element as coating. According to Table 2.5, for all joint conditions, the measured values obtained for edge straightness were far from the critical value of 300 μm illustrating that the bead edge variations were not recognizable by the naked eye [28].

Table 2.5 The edge straightness values measured by optical Keyence obtained for dissimilar joints.

Panels and laser mode	Edge straightness (μm)	
	Al side	Steel side
Al / EG – in-line	53.5	86.3
Al / HDG - in-line	96.9	67.4
Al / EG - cross	101.2	117.8
Al / HDG - cross	77.4	181.4

2.4.4 Mechanical evaluation

For each type of welded joints, three tensile tests were conducted. Since the thickness of panels varied and the welds were under a complex state of stress, the mechanical strength of joints was presented in terms of resistance (N/mm) (i.e., force at fracture of the specimen divided by its width). Figure 2.24 depicts the results of several series of tensile tests on coach peel joints. Although the strength of joints was roughly in the same range, the performance of dual-cross beam welded joints under tensile load was better than the dual in-line beam joints. The results indicated that because of larger elongation, there was a kind of ductile behavior in the cross-beam joints. Whereas, the in-line beam joints experienced a kind of brittle fracture. To clarify the failure mode, the fracture surface of the cross beam mode was studied by SEM as shown by Figure 2.25. The presence of elongated dimples as well as plasticized zones around the dimples could be considered as the main characteristics of the ductile fracture that happened at the brazed-Al interface.

Fractured specimens of tensile test were also indicative of different results for dual beam modes. As shown in Figure 2.26 samples in the dual cross-beam mode were failed at the aluminum/seam side. Whereas, in the dual in-line beam mode, fracture happened in the form of separation at the steel/seam interface.

Among the several studies that have been conducted on the dissimilar brazing of steel to aluminum, there was a common agreement on the fact that the critical value of thickness for the IMC layer should be 10 µm. The generated IMC layer beyond this value would weaken the tensile strength of the joint and would cause the steel-brazed bead to become brittle. Although the thickness of possible IMC layers for both types of in-line and cross-beam joints was measured in this study far from the critical value of 10 µm, there were two types of fracture modes. These differences in strength and fracture location could be attributed either to the thickness of the IMC layer generated on the steel/seam interface or the size of fusion zone on the aluminum/seam side. The first explanation for this phenomena can be correlated to the generated IMC layer. As described by Dharmendra et al. [29], there should be a kind of upper and lower limit for IMC layer thickness. If the IMC layer is either very thin or very thick, the steel/seam area would be the weakest part of the joint, and fracture would happen on this side of the joint. The other description for this type of alteration in fracture modes could be credited to the size of the fusion area in the in-line and cross beam joints. As shown in Figure 2.17 -Figure 2.18, where red lines indicate the boundaries of the fusion zone, the clear distinction between the size of the fusion-zone (aluminum/seam) areas for the two types of laser beams highlighted with red lines is obvious. The measured surface areas clarified that the in-line laser beam generated a larger fusion zone around $360980.61\ \mu m^2$. Whereas in the cross-beam fusion zone, this value decreased to $26341.34\ \mu m^2$. This considerable difference in fusion size area (around 13 times) could be a

strong claim that a higher fusion area led to a stronger joint on the aluminum/seam side and, eventually, in the joint fractured on the steel/seam side.

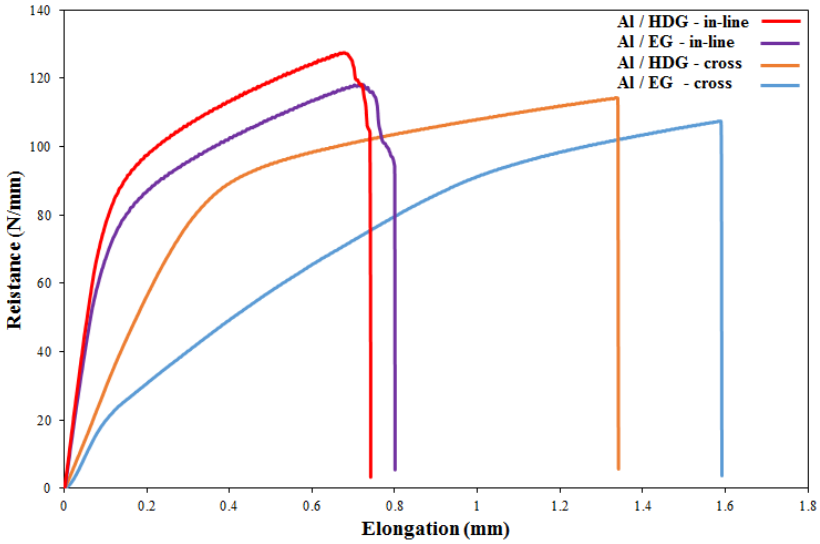

Figure 2.24 Tensile test curves for coach peel welded joints.

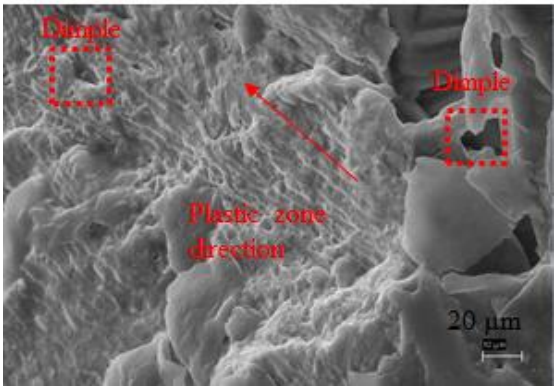

Figure 2.25 SEM fracture surface of the joint made Al / HDG – dual cross mode.

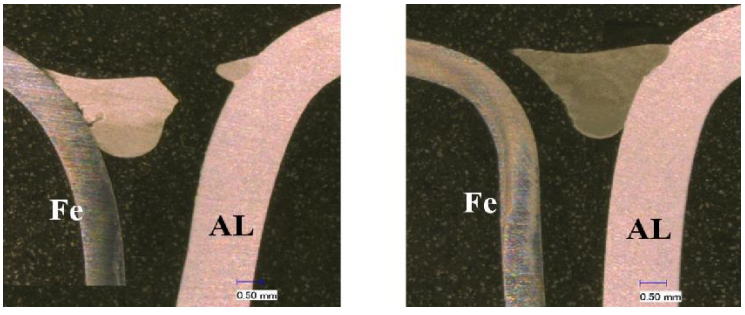

Figure 2.26 Fractured samples of tensile test: (a) dual cross beam, (b) dual in-line beam.

2.5 Conclusions

In the current investigation, the performance of two common types of dual-laser beam modes (cross and in-line) in laser welding-brazing of dissimilar materials was studied in respect to the defect-free joints with acceptable surface roughness. Although both types of beams could deliver jointed panels, the dual cross-beam mode demonstrated some superiority over the dual in-line beam. The major conclusions of this investigation were followed as:

1. Even though the surface roughness of all fabricated welds were in an acceptable range, the best surface roughness was achieved by a dual cross-beam laser joining HDG steel with aluminum.
2. The measured thickness of intermetallic layers in all joint combinations was far below the critical value of 10 μm.
3. The failure position of LWB joints was altered by changing the laser beam mode. In the dual cross-beam mode, specimens were fractured at the aluminum/bead side. Whereas in the dual in-line beam mode, fracture occurred at the steel/bead side.
4. Numerically predicted isotherms passing through the Al-steel interface were obtained in the range of 700-900˚C in which the IMC had the highest growth rate. However, the wetting duration of molten filler material on the steel surface was shorter than 1(s) and was not sufficient for thickening IMC. Thus, apart from the role of filler wire, concentrated heat input as well as high cooling rate induced by application of high-scanning speed restricted the rate of diffusion-control based IMC growth.

References

[1] E. Schubert, M. Klassen, I. Zerner, C. Walz, G. Sepold, Light-weight structures produced by laser beam joining for future applications in automobile and aerospace industry, Journal of Materials Processing Technology, 115 (2001) 2-8.

[2] K. Martinsen, S.J. Hu, B.E. Carlson, Joining of dissimilar materials, CIRP Annals - Manufacturing Technology, 64 (2015) 679-699.

[3] J. Min, Y. Li, B.E. Carlson, S.J. Hu, J. Li, J. Lin, A new single-sided blind riveting method for joining dissimilar materials, CIRP Annals - Manufacturing Technology, 64 (2015) 13-16.

[4] E. Taban, J.E. Gould, J.C. Lippold, Characterization of 6061-T6 aluminum alloy to AISI 1018 steel interfaces during joining and thermo-mechanical conditioning, Materials Science and Engineering: A, 527 (2010) 1704-1708.

[5] G. Sierra, P. Peyre, F. Deschaux Beaume, D. Stuart, G. Fras, Galvanised steel to aluminium joining by laser and GTAW processes, Materials Characterization, 59 (2008) 1705-1715.

[6] H. Laukant, C. Wallmann, M. Müller, M. Korte, B. Stirn, H.G. Haldenwanger, U. Glatzel, Fluxless laser beam joining of aluminium with zinc coated steel, Science and Technology of Welding and Joining, 10 (2005) 219-226.

[7] K. Saida, H. Ohnishi, K. Nishimoto, Fluxless Laser Brazing of Aluminum Alloy to Galvanized Steel using Tandem Beam- Dissimilar Laser Brazing of Aluminum Alloy and Steels, QUARTERLY JOURNAL OF THE JAPAN WELDING SOCIETY, 26 (2008) 235-241.

[8] P. Peyre, G. Sierra, F. Deschaux-Beaume, D. Stuart, G. Fras, Generation of aluminium–steel joints with laser-induced reactive wetting, Materials Science and Engineering: A, 444 (2007) 327-338.

[9] A. Mathieu, S. Matteï, A. Deschamps, B. Martin, D. Grevey, Temperature control in laser brazing of a steel/aluminium assembly using thermographic measurements, NDT & E International, 39 (2006) 272-276.

[10] G. Yang, J. Ma, H.-P. Wang, B. Carlson, R. Kovacevic, Studying the effect of lubricant on laser joining of AA 6111 panels with the addition of AA 4047 filler wire, Materials & Design, 116 (2017) 176-187.

[11] S. Yan, Z. Hong, T. Watanabe, T. Jingguo, CW/PW dual-beam YAG laser welding of steel/aluminum alloy sheets, Optics and Lasers in Engineering, 48 (2010) 732-736.

[12] S. Chen, Z. Zhai, J. Huang, X. Zhao, J. Xiong, Interface microstructure and fracture behavior of single/dual-beam laser welded steel-Al dissimilar joint produced with copper interlayer, The International Journal of Advanced Manufacturing Technology, 82 (2016) 631-643.

[13] L. Li, C. Tan, Y. Chen, W. Guo, C. Mei, CO2 laser welding–brazing characteristics of dissimilar metals AZ31B Mg alloy to Zn coated dual phase steel with Mg based filler, Journal of Materials Processing Technology, 213 (2013) 361-375.

[14] S. Frank, Flux-free laser joining of aluminum and galvanized steel, Journal of Materials Processing Technology, 222 (2015) 365-372.

[15] G. Yang, J. Ma, B. Carlson, H.-P. Wang, R. Kovacevic, Effect of laser beam configuration on microstructure evolution and joint performance in laser joining AA 6111 panels, Materials & Design, 123 (2017) 197-210.

[16] J. Ma, F. Kong, R. Kovacevic, Finite-element thermal analysis of laser welding of galvanized high-strength steel in a zero-gap lap joint configuration and its experimental verification, Materials & Design (1980-2015), 36 (2012) 348-358.

[17] J. Goldak, A. Chakravarti, M. Bibby, A new finite element model for welding heat sources, Metallurgical Transactions B, 15 (1984) 299-305.

[18] Z. Wan, H.-P. Wang, M. Wang, B.E. Carlson, D.R. Sigler, Numerical simulation of resistance spot welding of Al to zinc-coated steel with improved representation of contact interactions, International Journal of Heat and Mass Transfer, 101 (2016) 749-763.

[19] Filliard G, El Mansori M, Tirado L, Mezghani S, Bremont C, De Metz-Noblat M. Industrial fluxless laser weld-brazing process of steel to aluminium at high brazing speed. Journal of Manufacturing Processes. 2017;25:104-15.

[20] A. Koltsov, N. Bailly, L. Cretteur, Wetting and laser brazing of Zn-coated steel products by Cu–Si filler metal, Journal of Materials Science, 45 (2010) 2118-2125.

[21] T. Murakami, K. Nakata, H. Tong, M. Ushio, Dissimilar Metal Joining of Aluminum to Steel by MIG Arc Brazing Using Flux Cored Wire, ISIJ International, 43 (2003) 1596-1602.

[22] M. Vybornov, P. Rogl, F. Sommer, On the thermodynamic stability and solid solution behavior of the phases τ5-Fe2Al7.4Si and τ6-Fe2Al9Si2, Journal of Alloys and Compounds, 247 (1997) 154-157.

[23] J. Yang, Y. Li, H. Zhang, W. Guo, D. Weckman, N. Zhou, Dissimilar Laser Welding/Brazing of 5754 Aluminum Alloy to DP 980 Steel: Mechanical Properties and Interfacial Microstructure, Metallurgical and Materials Transactions A, 46 (2015) 5149-5157.

[24] M. Gatzen, T. Radel, C. Thomy, F. Vollertsen, Wetting behavior of eutectic Al–Si droplets on zinc coated steel substrates, Journal of Materials Processing Technology, 214 (2014) 123-131.

[25] L.A. Jácome, S. Weber, A. Leitner, E. Arenholz, J. Bruckner, H. Hackl, A.R. Pyzalla, Influence of Filler Composition on the Microstructure and Mechanical Properties of Steel—Aluminum Joints Produced by Metal Arc Joining, Advanced Engineering Materials, 11 (2009) 350-358.

[26] K. Bouché, F. Barbier, A. Coulet, Intermetallic compound layer growth between solid iron and molten aluminium, Materials Science and Engineering: A, 249 (1998) 167-175.

[27] H.R. Shahverdi, M.R. Ghomashchi, S. Shabestari, J. Hejazi, Microstructural analysis of interfacial reaction between molten aluminium and solid iron, Journal of Materials Processing Technology, 124 (2002) 345-352.

[28] H.-p.W. Xuesong Wang, Blair E. Carlson, Jianping Lin, Michael Poss and Joshua Solomon, Development of surface evaluation methods for class A welds, Sheet Metal Welding Conference XVII, Detiroit, 2016.

[29] C. Dharmendra, K.P. Rao, J. Wilden, S. Reich, Study on laser welding–brazing of zinc coated steel to aluminum alloy with a zinc based filler, Materials Science and Engineering: A, 528 (2011) 1497-1503.

Chapter 3

EFFECT OF FILLER WIRE COMPOSITION ON PERFORMANCE OF AL/GALVANIZED STEEL JOINTS BY TWIN SPOT LASER WELDING-BRAZING METHOD

3.1 Introduction

Government legislation regarding fuel efficiency and environmental issues has aroused the interest of the automotive industry to create new technological solutions. Beside the development of new powertrain solutions, mass reduction of the vehicle body is another effective approach. Lightweight structures currently are seen as a composite of structural materials such as steel, aluminum, and magnesium. From both a mechanical and economical perspective, hybrid structures have been introduced as an efficient way to satisfy these conditions [1]. In recent years, this approach has opened up an attractive field of research for joining aluminum and steel alloys together. The existence of a significant difference between Al and steel in terms of thermal and physical properties and almost zero solid solubility made the formation of intermetallic an inevitable result [2]. The generation of brittle intermetallic compounds (IMCs) with hardness around 1000 Vickers originated from the diffusion of iron into molten aluminum material. L. Agudo [3] pointed out that the formation of Fe_xAl_y from the Fe/Al intermetallic family was vital to have an effectual joining between the Al and steel. Lin et al. [4] showed that the mechanical performance of aluminum and steel joints were linked to the thickness of Fe and Al rich intermetallic layers where thicker ones lead to brittle fracture of joints. They stated that to avoid brittle fracture the thickness of IMC layer should be less than 10μm.

The growth of the IMC layer was correlated to the thermal cycle at the Fe/Al interface and the thickness can be controlled by process temperature, process duration, and time of interaction [5]. Laser-based joining technologies with concentrated energy density on a small area, ease of automation, and ability to reach a high scanning speed could be a suitable candidate for joining dissimilar materials. Several researches have been conducted on laser welding-brazing (LWB) of steel to aluminum in different joint configurations wherein a fusion welding joint was generated on the aluminum side and a brazing joint was formed on the steel side of the weld. Saida et al. [6] used LWB for an Al-steel lap joint configuration with AlSi12 filler. They fabricated joints at a laser power level of 1300 W resulting in a maximum strength of approximately 80% of the Al5052 base material and an IMC layer thickness less than 2μm. Filliard et al. [7] investigated LWB of steel to Al in an angled configuration by means of a single laser beam with spot diameter of 3 mm, laser power of 6 kW, and welding speed of 4-6 m/min. They succeeded in obtaining joints with mechanical strength of 101% of mechanical properties of filler material and IMC layers with thickness less than 2μm.

Besides the development of laser welding-brazing process by using of single laser beam, some studies have focused on the utilization of multi-laser beams with the purpose of enhancing the brazed quality and robustness of process. Yang et al. [8] comprehensively investigated the effect of laser beam arrangement on welding of similar materials in the coach peel configuration. Based upon the comparative results in terms of the mechanical properties, surface roughness, microstructural evolution, and finite element thermal analysis, the cross-beam laser mode was recommended as the best choice to join the aluminum panels. Mitterlstadt et al. [9] investigated the potentioal of using two-beam laser brazing process by means of two laser heads with the purpose laser-preheating to get more reliable process at desired high speeds.

The LWB joints are typically on the visible exterior of a car body for applications such as a deck lid and roof. The resultant joints require not only adequate strength to pass dynamic testing, but the welded joints should also be defect free with sufficiently low surface roughness to avoid post-weld processing. There is no doubt that these required qualities of the LWB joint are directly influenced by the input process parameters. Consequently, laser welding-brazing can be considered as a multi-input multi-output process. This point of view can enable utilization of the design of experiments (DOE) method to build up mathematical relationships between the LWB process input parameters and output variables. However, there are no available studies in the literature on the multi-response optimization of laser welding-brazing of steel to Al and the interaction of process parameters by using a statistical approach. There is limited work on the laser brazing of Al to Al and steel to steel coach peel panels which investigated a single response either on geometry of the weld bead or on surface roughness. Zhou et al. [10] conducted a hybrid optimization methodology to address the effects of process parameters on the bead profile of laser brazed steel panels. They combined a genetic algorithm (GA) and ensemble of metamodels (EMs) to establish the relationships between process parameters and bead geometries measured from experimental data. Rong et al. [11] optimized the seam shape in the laser brazing process by using the method of back propagation neural network (BPNN) and genetic algorithm (GA). They introduced welding speed, wire speed rate, and gap as the input parameters and discussed their effects on the sum values of bead geometry. Yang et al. [12] conducted experiments based on Taguchi L9 orthogonal array to optimize the shielding gas parameters to enhance the surface quality and mitigate the weld surface defects. The experimental results showed that the surface roughness of the bead was less than 1 μm when a circular gas nozzle was positioned at 5 mm

behind the laser beam, and the flow rate of shielding gas (pure argon) was adjusted at 30 Standard Cubic Feet per Hour (SCFH) with an inclination angle of 45° to the horizontal plane.

In this study laser welding-brazing process was utilized to join aluminum to steel panels by four commonly used filler wires at a high scanning speed. First, the influence of process parameters on desired responses was investigated by means of Response Surface Methodology (RSM) in order to clarify the effects of input parameters on the final results. Then a multi-objective optimization approach was implemented to find the optimal processing condition based on defined responses (maximum mechanical strength and minimum surface roughness). Finally, the effect of filler wires (AlSi12, AlSi5, AlSi3Mn1, and ZnAl15) and distribution of alloying elements in the weld were investigated with respect to the mechanical strength, surface roughness, and microstructure.

3.2 Experimental work

3.2.1 Material and methods

The materials used for dissimilar LWB in this study were aluminum 6022 and Hot Dip Galvanized (HDG) low carbon steel (GMW2M-ST-S-CR4) with chemical compositions as presented in Table 3.1. The thickness of coach peel panels were 1.2 mm and 0.65 mm for Al and HDG, respectively. The coach peel configuration in this study corresponds to the simplified geometry of an industrially relevant automotive application in the joining of roof to body side (see Figure 3.1).

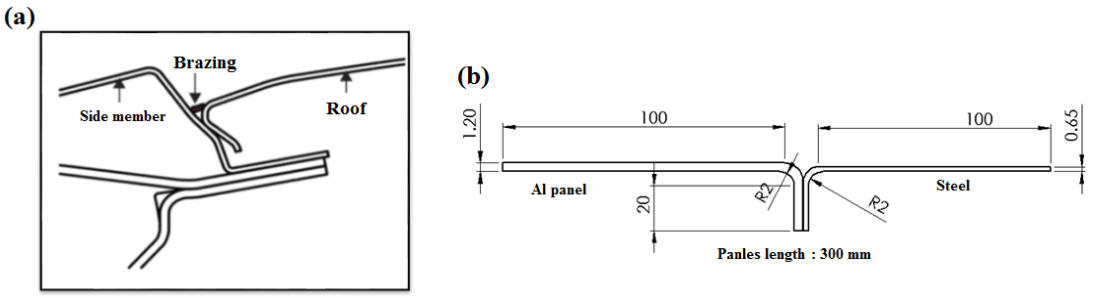

Figure 3.1 (a) Industrial application of aluminum roof-steel body side configuration, (b) dimensions of simplified coach peel configuration (mm).

Table 3.1 Chemical composition of substrate materials.

Substrates	Alloying elements							
	Si	Fe	Mn	Mg	Zn	Ti	Cr	Al
Al6022	1.00	0.15	0.07	0.56	0.01	0.02	0.02	Bal.
Hot dip Galvanized steel (HDG)	C	Al	Mn	P	Si	S	Fe	
	0.003	0.034	0.11	0.01	0.005	0.008	Bal.	

The average zinc coating thickness of steel panels was approximately 10μm with a typical cross section of coating is presented in Figure 3.2. It should be noted that the coating thickness was not uniform and varied (5 μm-12 μm) between locations. To study the influence of different filler materials on the quality of the resulting joint, four compositions of consumables having a diameter of 1.6mm were employed in studying LWB of aluminum to steel (refer to Table 3.2). The experimental set-up is illustrated in Figure 3.3, which includes a 4-kW continuous fiber laser (IPG Photonics Corporation) sending a 1075 nm wavelength beam through a 400μm optical fiber. The axis of the laser head was inclined to 5° from the vertical position in order to protect the optics from any damage caused by the back-reflected laser beam. An ABICOR BINZEL wire-feeding system was set up to deliver filler wire at 35° from the vertical axes. In order to provide twin beams, a beam splitter was mounted on the laser head to deliver two beams (side by side) with power ratio of 50/50. The twin-spot beam was defocused in a plane that each single beam diameter

was 1.5 mm. By considering the spot spacing as constant 0.6 mm the total width of twin-spot was 2.1 mm, as measured by Beam Viewer. In all experiments, the laser beam was adjusted to be at the center of the groove. Argon was delivered at a constant flow rate of 25 SCFH as the shielding gas 45° from the vertical axes.

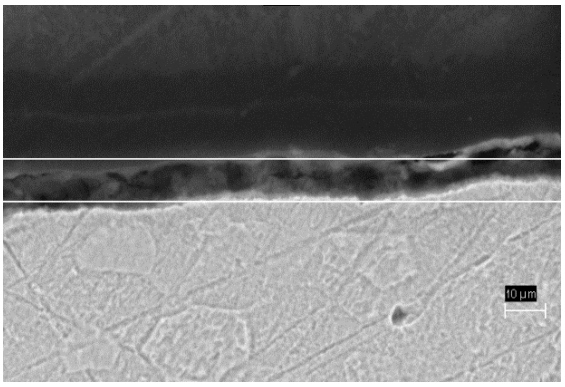

Figure 3.2 Cross-sectional view of zinc coating.

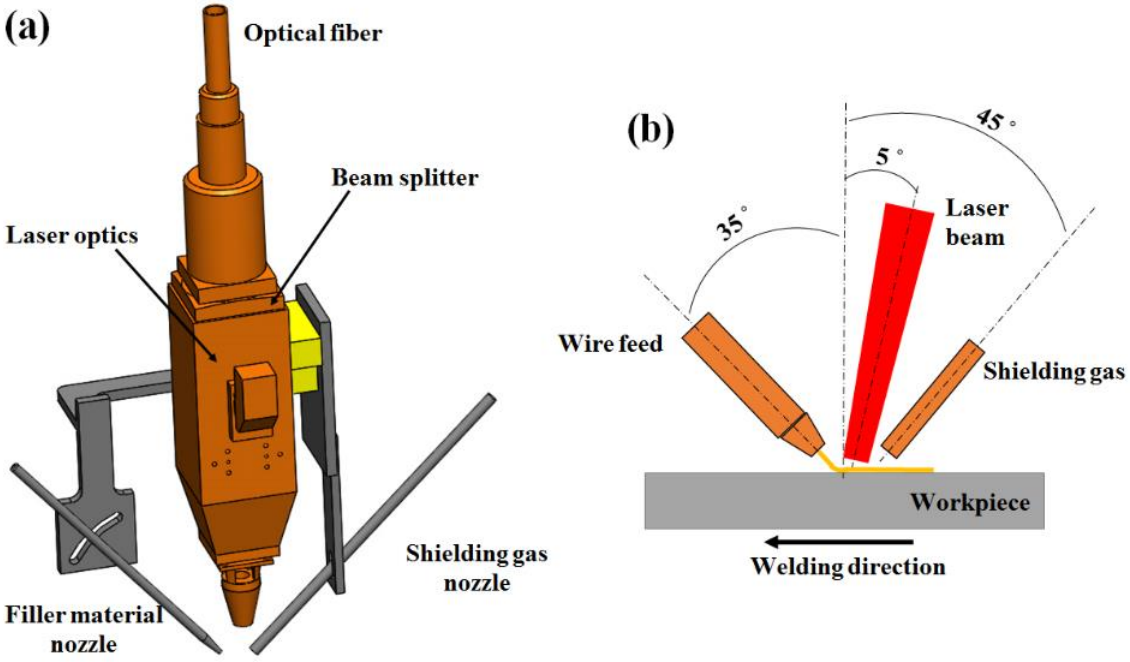

Figure 3.3 (a) schematic view of experimental set-up, (b) close-up illustration.

Table 3.2 Filler material alloy and melting range.

Alloy	Melting range (ºC)
AlSi12 (Al4047)	575 - 585
AlSi5 (Al4043)	573 - 625
AlSi3Mn1 (Al4020)	577 - 640
ZnAl15	382-450

3.2.2 Measurements and characterization

To study the resulting joint microstructure, weld joints were transversely cut using an abrasive waterjet cutting machine. After hot mounting, the sectioned samples were first ground by SiC papers of increasingly finer grit (120-2000) and then polished using 9, 6, 3, and 1μm diamond paste solutions. Two types of etching solutions (Keller reagent and Nital 3%) were used to reveal the general microstructure of aluminum and steel, respectively. A Leo-Zeiss 1450VPSE scanning electron microscope equipped with Energy Dispersive Spectroscopy (EDS) was utilized to characterize the microstructure and composition of the resulting intermetallic layer. Uniaxial tensile testing was conducted by means of an Instron 5582 testing machine at room temperature and with a monotonic displacement rate of 1 mm/min to evaluate the strength of the LWB joints. In this regard, the current work uses the term Resistance to represent the load measured during tensile testing over the width of the welded-brazed joint. This is done to provide a relative basis of comparison since it is difficult to measure the actual load bearing cross-sectional area of the welded-brazed joint. In order to meet the pure tensile loading condition shims were used to offset the thickness difference between the Al and steel sheets. From each welded sample three standard tensile coupons were cut in accordance with ASTM E 8M-01 [13]. The tests were terminated when the specimens separated. The fractured surfaces were observed by SEM. Surface roughness

of resulted beads was measured by Micro Photonic Nanovea non-contact profilometer. To eliminate the errors of measurement and secure reliable results, each surface roughness measurement was repeated three times. The average was reported as the representative surface roughness. The microhardness values of joints was measured by means of a microhardness tester machine at a load of 300 gf and a dwell time of 15 s.

3.2.3 Design of experiments

The optimization of the welding parameters was done for an Al4020 filler wire, because it's melting temperature encompasses the melting temperatures of other Al-based filler materials (Al4043-Al4047). The experiments were performed based on the three-factor with three-level Box-Behnken statistical design. This approach based on the Response Surface Methodology (RSM) offered the total number of 17 experiments. The main processing parameters such as laser power, welding speed, and wire feed rate were selected as the independent input variables, and surface roughness and mechanical strength represented the output variables. This number of experiments can provide adequate information to fit the second order polynomial Eq. (3-1).

$$y = a_0 + \sum_{i=1}^{n} a_i X_i + \sum_{i=1}^{n} \sum_{j=i+1}^{n} a_{ij} X_i X_j + \sum_{i=1}^{n} a_{ii} X_i^2 + e_r \qquad (3\text{-}1)$$

where n is the number of independent input variables (factors), X_i (i=1, 2, 3) are input predictors or controlling variables, a_0 is the constant coefficient, e_r is the error, and a_i, a_{ij} and α_{ii} are the coefficients of linear, interaction, and quadratic terms, respectively. The values of process parameters and their corresponding levels for aluminum-based filler wires are summarized in Table 3.3.

Table 3.3 Process variables and experimental design levels for Al-based filler material (AlSi3Mn1, Al4020).

Variable (factors)	Unit	Notation	-1	0	1
Laser power	kW	LP	3.2	3.6	4
Welding speed	mm/s	WS	60	70	80
Wire feed rate	mm/s	WFR	70	80	90

3.3 Parameters optimization

3.3.1 The effect of processing parameters on measured responses

The experimental results of surface roughness and mechanical resistance for laser welded-brazed joints using the AlSi3Mn1, Al4020 wire are listed in Table 3.4. Design-Expert V10 statistical software was used to analysis the measured responses. In order to implement the response surface model by means of reduced liner or quadratic models (Eq.1) an Analysis of Variance (ANOVA) method was employed. This technique can distinguish the effect of input parameters and their interactions on the specific response. The step-wise regression method was used to eliminate the insignificant terms with respect to their *p*-values. In this study, the level of confidence was considered 95%, and significant terms should have p-values less than the confidence level. Therefore, significant terms should have p-values less than 0.05. The ANOVA test results for mechanical resistance and surface roughness are listed in Tables 3.5 and 3.6, respectively.

Table 3.4 Design matrix and experimental measured responses.

Std	Run	LP	SS	WFR	Surface roughness (μm)		Resistance (N/mm)	
					Average value	Standard deviation	Average value	Standard deviation
7	1	3.2	70	90	0.9226	0.027	90.32	12.07
14	2	3.6	70	80	1.59	0.2954	94.46	9.59
16	3	3.6	70	80	1.73	0.163	89	7.36
9	4	3.6	60	70	1.04	0.093	91	8.05
17	5	3.6	70	80	1.33	0.078	94.01	10.4
1	6	3.2	60	80	0.903	0.073	102	3.51
11	7	3.6	60	90	1.95	0.152	100.51	10.76
12	8	3.6	80	90	1.83	0.21	96.05	4.03
5	9	3.2	70	70	1.25	0.17	141.42	2.48
3	10	3.2	80	80	1.63	0.216	75	8.2
8	11	4	70	90	1.33	0.032	125.8	7.35
13	12	3.6	70	80	1.35	0.147	103.75	16.86
15	13	3.6	70	80	1.52	0.062	96.2	8.04
6	14	4	70	70	1.4	0.14	100.76	4.85
4	15	4	80	80	1.36	0.195	122.24	5.32
10	16	3.6	80	70	1.47	0.185	92	11.6
2	17	4	60	80	1.605	0.096	134.72	5.62

The effect of process parameters and their interaction on each response are listed in ANOVA tables. The lack of fit and R^2 values were also included to imply the goodness of fit between the measured and predicted results. Although the R-squared values are not too close to 1, the models

indicate a good adequacy. Because the value of adequate precision for both responses was greater than 4 as the desirable ratio. Based on ANOVA analysis, laser power and the interaction of laser power and wire feed rate were the significant terms for the mechanical resistance response. In the surface roughness the significant terms were laser power, wire feed rate, and interaction of laser power and welding speed. The final mathematical response models for mechanical resistance and surface roughness as described by design expert software are summarized in Eqs. (3-2, 3-3).

$$\textbf{Resistance} = 2981.687 - 1154.918\times LP - 3.803\times WS - 17.287\times WFR + 0.907\times LP\times WS + 4.758\times LP\times WFR + 101.953\times LP^2 \quad (3\text{-}2)$$

$$\textbf{Surface roughness} = 234.64 - 135.97\times LP + 0.189\times WS - 3.306\times WFR - 0.0607\times LP\times WS + 1.891\times LP\times WFR - 0.00137\times WS\times WFR + 19.34\times LP^2 + 0.00106\times WS^2 \quad (3\text{-}3)$$

Table 3.5 ANOVA analysis for mechanical resistance of AlSi3Mn1, Al4020 filler wire joints.

Source	Sum of Squares	df	Mean Square	F-value	p-value	
Model	3578.05	6	596.34	4.08	0.0248	Sign.
A-LP	699.01	1	699.01	4.78	0.0536	
B-WS	230.48	1	230.48	1.58	0.2376	
C-WFR	19.53	1	19.53	0.13	0.7222	
AB	52.71	1	52.71	0.36	0.5614	
AC	1449.32	1	1449.32	9.92	0.0103	
A^2	1127.00	1	1127.00	7.71	0.0195	
Residual	1460.89	10	146.09			
Lack of Fit	1346.79	6	224.47	7.87	0.0329	Sign.
Pure Error	114.10	4	28.53			
Cor Total	5038.95	16				

$R^2 = 0.7101$, Adj $R^2 = 0.5361$, Pred $R^2 = -0.7558$, Adeq Precision = 7.319

Table 3.6 ANOVA analysis for surface roughness of AlSi3Mn1, Al4020 filler wire joints.

Source	Sum of Squares	df	Mean Square	F-value	p-value	
Model	1.21	8	0.14	7.78	0.0084	Sign.
A-LP	0.12	1	0.12	6.84	0.0346	
B-WS	0.076	1	0.076	4.38	0.0745	
C-WFR	0.44	1	0.44	22.55	0.0021	
AB	0.28	1	0.28	13.21	0.0086	
AC	0.017	1	0.017	0.95	0.3679	
BC	0.076	1	0.076	4.23	0.0784	
A^2	0.25	1	0.25	13.43	0.0079	
B^2	0.048	1	0.048	2.68	0.1456	
Residual	0.13	7	0.018			
Lack of Fit	0.012	3	4.153E-003	0.15	0.9262	Not Sign.
Pure Error	0.11	4	0.028			
Cor Total	1.38	16				

R2 = 0.9091, Adj R2 = 0.7923, Pred R2 = 0.7217, Adeq Precision = 10.354

The perturbation plot that clarifies the effect of process factors at the center point of design on the mechanical resistance is shown in Figure 3.4 (a). It is evident that welding speed and wire feed rate have negative linear effect on this response, in which by increasing each of them the resistance response was decreased. It can be seen that the effect of welding speed was more important than the effect of wire feed rate. Considering laser power, mechanical resistance was first declined by enhancing the level of laser power up to the center point of design. Then, by passing this point the resistance commenced to increase. Laser power is the most significant factor affecting the mechanical resistance. Figure 3.4 (b-c) depict the response surface (3D) and counter plot (2D) of laser power and welding speed effects on the mechanical resistance at the center level of wire feed rate (80mm/s).

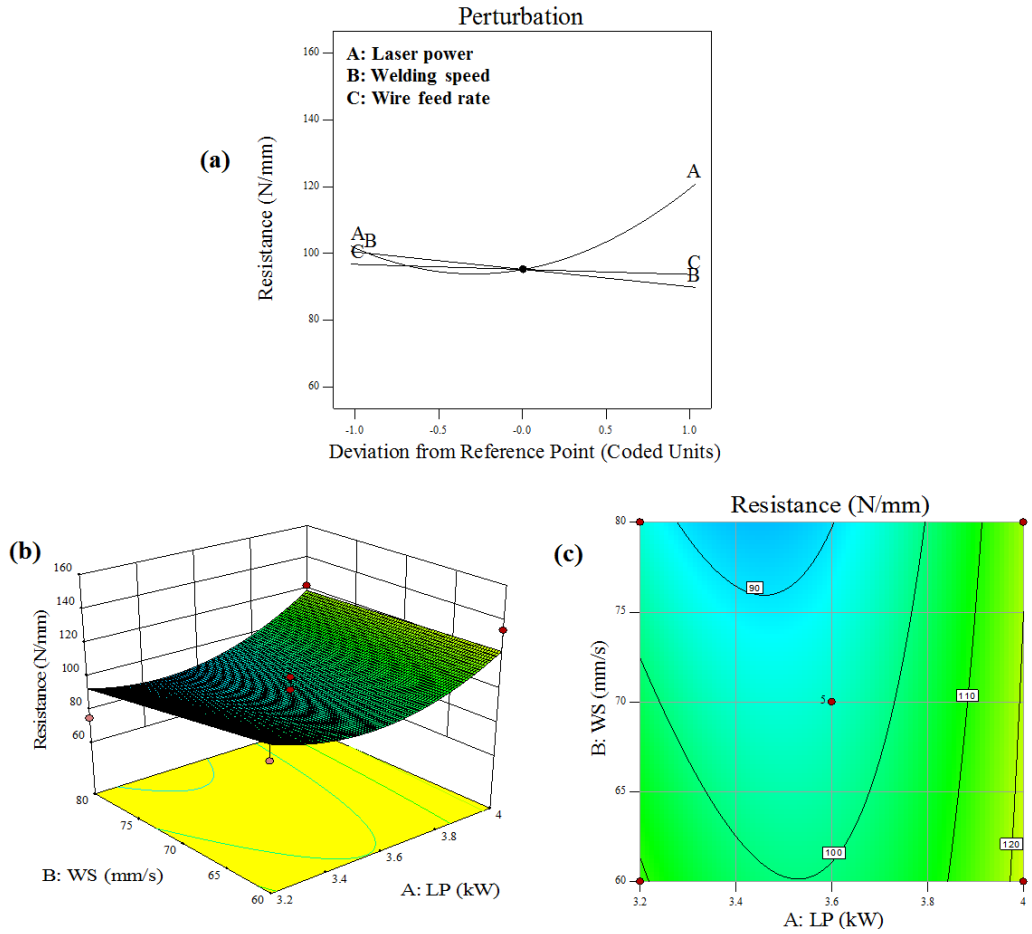

Figure 3.4 (a) Perturbation plot showing the effect of all factors on the mechanical resistance, (b-c) Response surface and graphical counter of the effect of laser power and welding speed on mechanical resistance for AlSi3Mn1, Al4020 filler wire joints.

Figure 3.5 (a) is the perturbation plot of the surface roughness response that indicates the effect of input parameters on this response. With the minimum surface roughness as criteria, it can be noticed that the welding speed and wire feed rate are the two independent variables that had negative effect on the surface roughness response. As the level of these two factors increased, the surface roughness was also increased. Concerning laser power, the curve has a maximum point around the center point of design and a minimum value of surface roughness with respect to the laser power was achieved on the lower level. Figure 3.5 (b-c) also illustrate the interaction effect of welding speed and wire feed rate on the surface roughness at the laser power of 3.6 kW. With

use of the response surface and graphical counter the interaction of factors on the desired response and also the consistency of results can be interpreted with the perturbation plot.

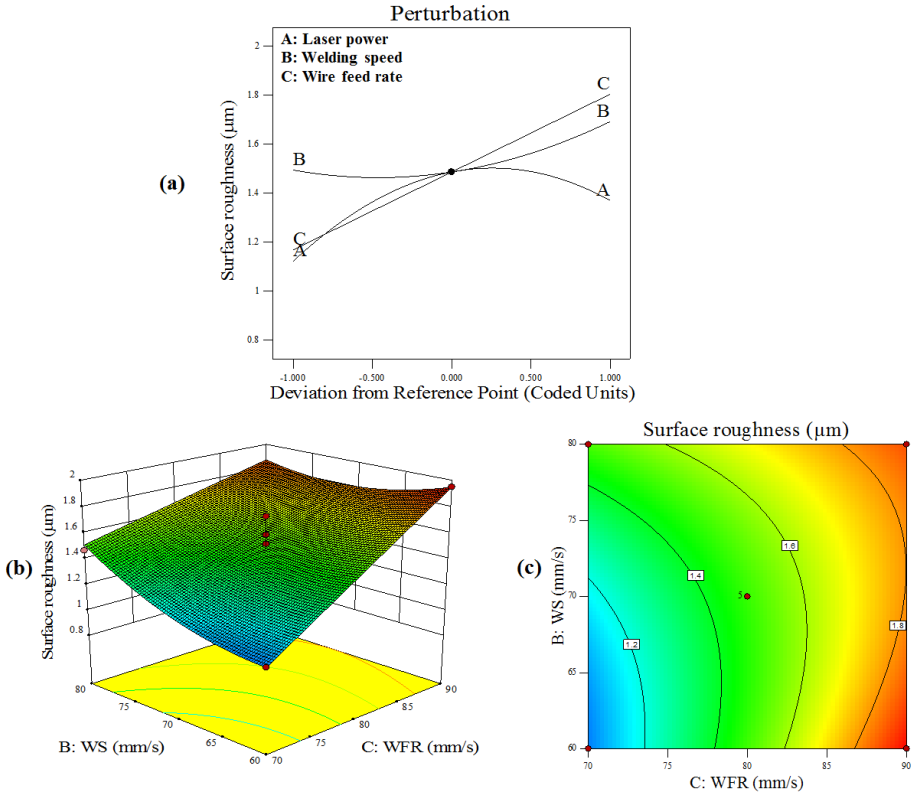

Figure 3.5 (a) Perturbation plot showing the effect of all factors on the surface roughness, (b-c) Response surface and graphical counter of the effect of wire feed rate and welding speed on surface roughness for AlSi3Mn1, Al4020 filler wire joints.

3.3.2 Validation of the models

In order to study the accuracy of numerically predicted results and their deviations from experimental results, design expert software was employed to provide appropriate graphs to clarify these concepts. Figure 3.6 exhibits the relationship between the actual and predicted values of mechanical strength and surface roughness. The experimentally measured and empirically obtained results for two responses tend to be close to the trend line with the slope of 1. It could be concluded that the predicted values by means of developed models were in a good agreement with the experimental results. The precision of models was further confirmed by the normal probability

of the developed model vs. residual graphs. As can be seen in Figure 3.6, the distribution of residuals along the diagonal line verifies that errors were normally distributed and models were developed appropriately.

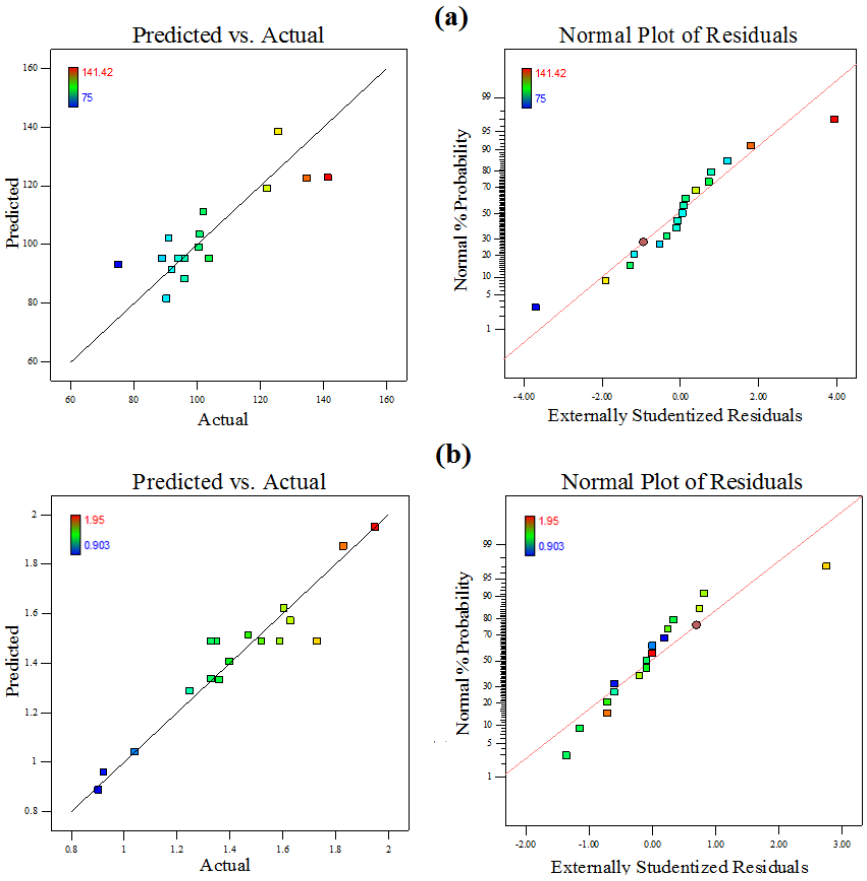

Figure 3.6 Predicted vs. Actual results and normal probability plots: (a) mechanical resistance, (b) surface roughness for AlSi3Mn1, Al4020 filler wire joints.

3.3.3 Optimization

For the purpose of optimization, a desired approach using design-expert software was utilized. This method is generally used in optimizing multi-response cases, in which the goals of the optimization criteria are represented as a single dimensionless factor called the desirability factor. This factor should be in the range from 0 to 1 where the value of 1 is the most desirable. The optimization criteria in LWB of dissimilar joints was reaching the minimum surface roughness

and maximum mechanical strength within the selected range of process parameters, as presented in Table 3.7. The experimental condition that has the highest desirability value was selected as the optimum condition. The ramp report for the multi-objective optimization results is graphically presented in Figure 3.7 for the optimized conditions. The optimal solution best minimizes the surface roughness with a value of 0.913µm and maximizes the mechanical strength with a value of 131N/mm.

Table 3.7 Optimization criteria.

Name	Criteria
Surface roughness	Minimize
Mechanical strength	Maximize
Laser power	In in range
Welding speed	In in range
Wire feed rate	In in range

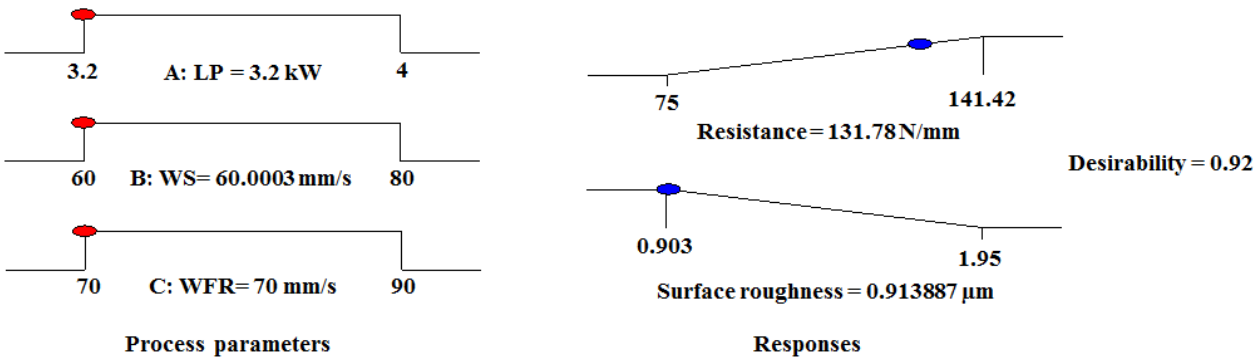

Figure 3.7 Optimum condition and ramp reports of multi-response optimization for AlSi3Mn1, Al4020 filler wire joints.

In order to verify the accuracy of multi-objective optimization results, additional experiments were conducted in the optimum condition. The average values of measured responses and predicted ones are summarized in Table 3.8. It can be shown that the difference between the

predicted and measured responses in the optimum condition was less than 10% which is a level acceptable from an industrial perspective.

Table 3.8 Confirmation experiments in the optimum processing condition for AlSi3Mn1, Al4020 filler wire joints.

Processing parameters				Responses	
LP (kW)	WS (mm/s)	WFR (mm/s)		Resistance (N/mm)	Surface roughness (μm)
3.2	60	70	Measured	120.34	0.93
			Predicted	131.78	0.91
			Error %	9.5	2.52

3.3.4 Zn-15%Al filler material processing parameters

Due to the Response Surface Method the optimized process parameters for welding aluminum to galvanized steel by using the AlSi3Mn1 filler wire was achieved. The melting temperature of the aluminum based wires (see Table 3.2) are within the same melting range; this optimal condition is also considered to be applicable to AlSi12 and AlSi5 filler materials. For ZnAl15 filler wire which has a lower melting temperature range (382℃ -450℃), this optimal condition cannot be applied. Based on our preliminary experiments, the Zn was mostly vaporized under the laser power of 3.2kW, and the groove was not filled with molten filler material thus, the resulting joint was not sufficient quality. To overcome this hindrance, the main process parameters were modified in order to achieve acceptable results. By comparing the performance of filler wires with respect to the surface roughness and fracture strength, the process parameter levels similar to those employed previously were investigated. The experiments on this type of wire were carried out at a welding speed of 3.6 m/min (60 mm/s). The laser power was decreased from 2.4 kW to 1 kW in increments of 0.2 kW and wire feed rate was tried in the range of 70 mm/s to 90 mm/s.

The resultant joints generally exhibited greater surface roughness, and fracture locations varied from within the weld bead to within the substrate material. The process parameters that delivered better surface quality and the highest mechanical performance were laser power 1.6 kW, welding speed 60 mm/s, and wire feed rate 90 mm/s.

3.4 Results and discussions

3.4.1 Microstructures and intermetallic layers

Metallographic analysis was completed on typical polished cross-sections, refer to the joints made by AlSi12 and ZnAl15 wires in Figure 3.8. The most obvious difference is the greater penetration of the Zn-based filler wire both in terms of depth into the gap between coupons as well as penetration into the Al6022 substrate.

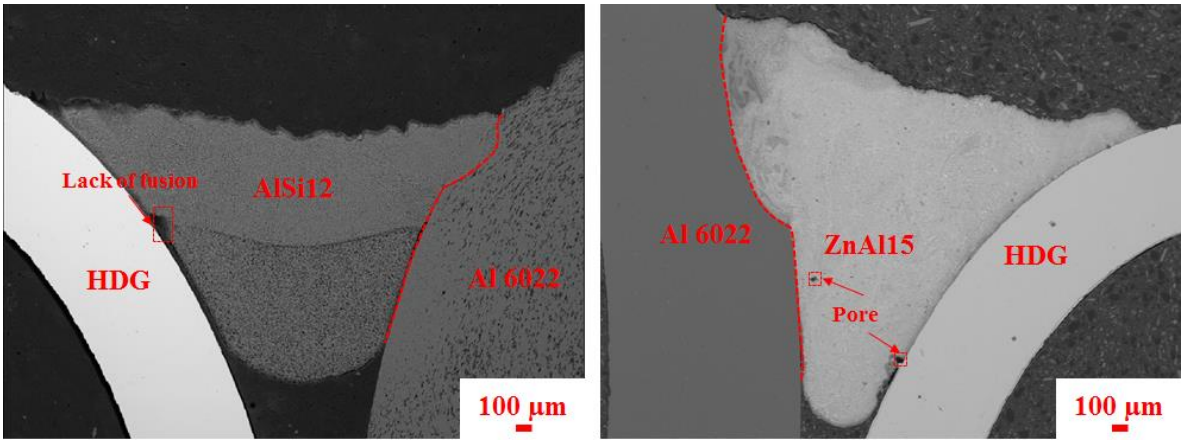

Figure 3.8 SEM observation of cross section of the joint made by (a) AlSi12 and (b) ZnAl15.

The high solubility of Zn inside the Al and formation of eutectic compound with very low melting point could be the main reason for development of inter-diffusion area along Al/bead interface [14, 15]. One potential source for the gas pores may be the zinc evaporation from the base galvanized steel. The reason behind this phenomena may originate from the high cooling rate of LWB process at high welding speeds based on an inadequate amount of time for zinc vapors to

escape [16]. This occurrence become worse in Zn-base filler material that there were too much zinc fumes during the joining process.

One of the most important challenges regarding dissimilar laser welding-brazing is the formation of undesired intermetallics that can drive poor mechanical properties if fractured. The microstructures at the steel substrate/braze interface for the Al-based wires and Zn-based wire are presented in Figure 3.9. Based on EDX compositional analysis the average chemical composition of dilution layer was obtained and the possible closest IMC that could form was determined. The type and average IMC layer thickness for each filler material is summarized in Table 3.9. As can be observed, among the Al-based wires, the thickest IMC was formed for the type of wire with the lowest amount of Si (AlSi3Mn1) and increasing the Si content of wire reduced the thickness of the IMC. The reduction of IMC layer by increasing the Si content of filler wire was attributed to several hypothesizes. Dharmendra et al. [17] pointed that filler wires with lower melting point improves wetting and reduces the IMC layer thickness. However, in the current body of work, refer to Table 3.2, addition of Si reduces the Solidus-Liquidus temperature range while maintaining a comparable Solidus temperature of approximately 575^{o}C. Thus, it would appear that the increased IMC layer thickness can be attributed to an extended time of the steel substrate being in contact with a molten pool. Furthermore, in LWB process because of high scanning speed and concentrated heat input, higher cooling rate could be expected and it would be the main reason to limit the growth of IMC excessively. It was stated that the increase of the applied cooling rate facilitates the formation of stable Si-rich Al_7Fe_2Si instead of binary Al-Fe IMCs which is the predominant phase at slower cooling rates [18]. The reason behind this phenomenon can be related to the difference in solubility and diffusivity of Fe and Si in Al. The higher cooling rate leads to a higher solubility and faster diffusion of Si and lower Fe concentrations at the interface [19].

Moreover, it was shown that diffusion coefficient of ternary Al_7Fe_2Si is much smaller than that of binary Al-Fe IMCs. Since the growth of IMC is diffusion control-based process, presence of Si could be so effective to decelerate the IMC thickening [20]. Also, it was reported that the presence of Si in Fe/Al system hinders the diffusion rate of Al atoms in the Fe matrix and inhibits the formation of brittle Al-Fe IMC [16].

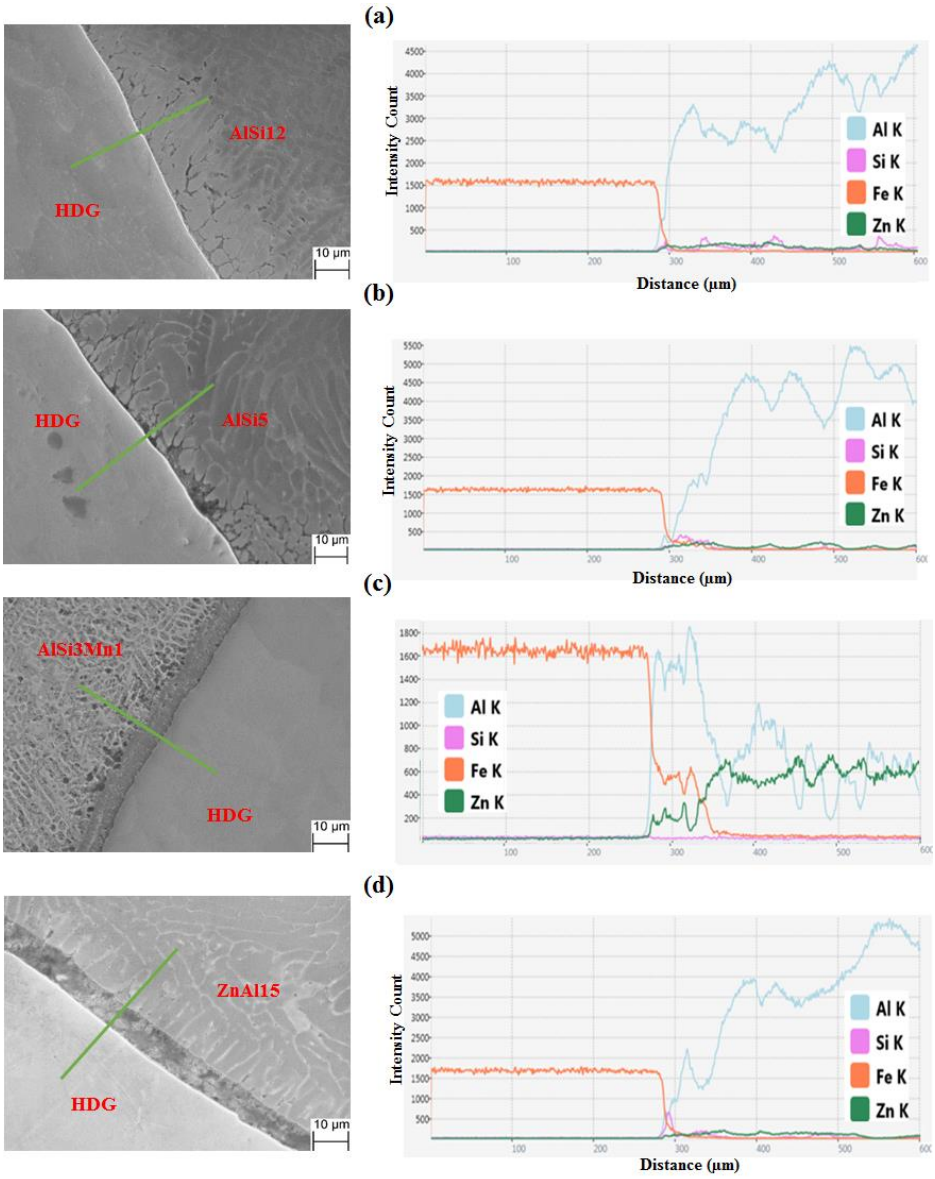

Figure 3.9 SEM micrographs and distribution of alloying elements at the interface of steel substrate/braze joint for different filler wire materials.

Table 3.9 Average thickness and EDS analysis of the dilution layer for different filler wires.

Type of filler wire	Dilution layer thickness (μm)	Atomic percent of alloying elements				Possible IMC type
		Al	Fe	Zn	Si	
AlSi12	1.6-2	72	16	1	11	Al_7Fe_2Si
AlSi5	2.5-3	75	17	2	6	Al_7Fe_2Si
AlSi3Mn1	5-6	70	15	15	-	Al_3FeZn
ZnAl5	6-8	62	29	9	-	Al_3FeZn

The largest dilution layer was measured around 8 μm for brazed of Zn-based wire and the type of IMC was specified as Al_3FeZn. Dong et al [21] observed similar compositions at the boundary in welding of Al alloy to galvanized steel using TIG with ZnAl15 wire. They also found a considerable amount of ZnO phase exactly adjacent to the IMC in the brazed region. In the present study, such phase was not observed and is attributed to the high cooling rate associated with a fast laser welding speed of 60 mm/s compared to that of 2 mm/s and a larger heat source applied.

It was reported that Zn-based filler wires, in contrast to Al-based filler wires, resulted in thick dilution layer since in presence of Zn a larger extent of Fe from steel substrate diffused into the interfacial layer [22]. However, larger affinity of Zn to Al compared to Fe improves formation of ternary Al_3ZnFe which is favorable for the good joint strength. Thus, formation of binary IMCs like Al-Fe and Fe-Zn that are detrimental to joint strength was restricted significantly [17, 22]. As reported AlFeZn is made of closed-pack crystals with several slip systems that prevents dislocation pile up and reduces brittleness [14]. From the results above, the schematic formation of IMC at the interface of steel and two types of Al-Si and Zn-Al based wires is shown in Figure 3.10. For Al-based wire, firstly, the steel substrate is wetted by the liquid aluminum. Secondly, solid state diffusion of Fe atom toward the interface as well as aggregation of Si atoms leads to formation of

Al-Fe-Si intermetallic layer. For the Zn-Based wire, the base steel is spread by Zn liquid, then solid state diffusion of Fe atom toward the interface as well as aggregation of Al atoms leads to formation of Al-Fe-Zn IMC.

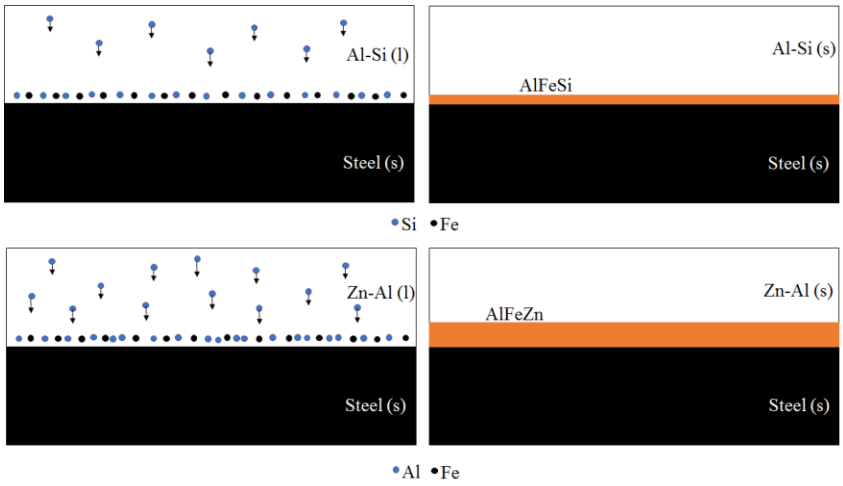

Figure 3.10 Formation process of the IMC layers during aluminum-steel LBW with Al-Si and Zn-Al based wires.

Based on the microstructural observation, it was found that the formation of IMC was not uniform along the interface of steel/bead and the IMC was thickest in the center regions of the braze/steel interface (compare Zone 2 to Zone 1 of Figure 3.11). Because the IMC growth is controlled by the solid state diffusion of Fe and/or Al within the steel and IMC layer itself, the resulting thermal history is a crucial factor. Based on obtained results from previous chapter, isotherms obtained by numerical simulation were in accordance with the variation of IMC thickness along the steel/brazed interface. A similar result was reported by Fillard et al. [7]. They found that the superposition of different convection flows including Marangoni, centrifugal, and centripetal convection flow reach the hot molten pool to the middle part of steel/brazed interface and kinetically increase the reaction rate at this area that leads to hasten the growth of IMC.

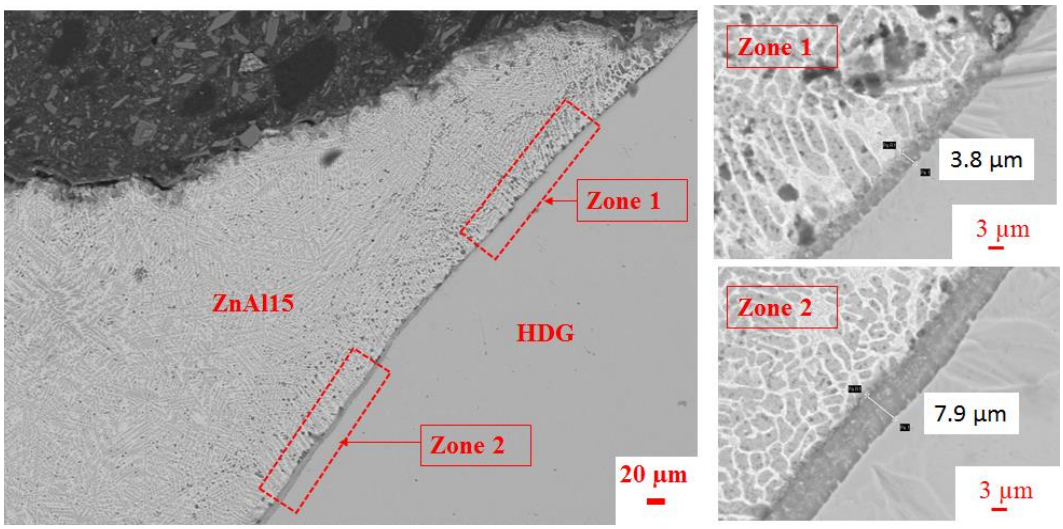

Figure 3.11 Variation of IMC layer along the interface of brazed/steel for bead obtained by ZnAl15 filler wire.

Another interesting point is the growth direction of columnar dendrites with respect to steel/bead interface. According to Figure 3.12 for Al-based wires, the perpendicular growth direction of solidified Al dendrites with respect to the boundary was taken account as epitaxial growth. Since the chemical composition of deposited wire and dilution layer was similar, this type of growth mode was dominant for these type of brazed joints [14]. However, for Zn-based wire, the dendrite growth direction was random in regard to the dilution layer. Such non-preferred growth direction was attributed to a mismatch between the crystallographic features of Zn-based solidified dendrites and Al-based dilution layer.

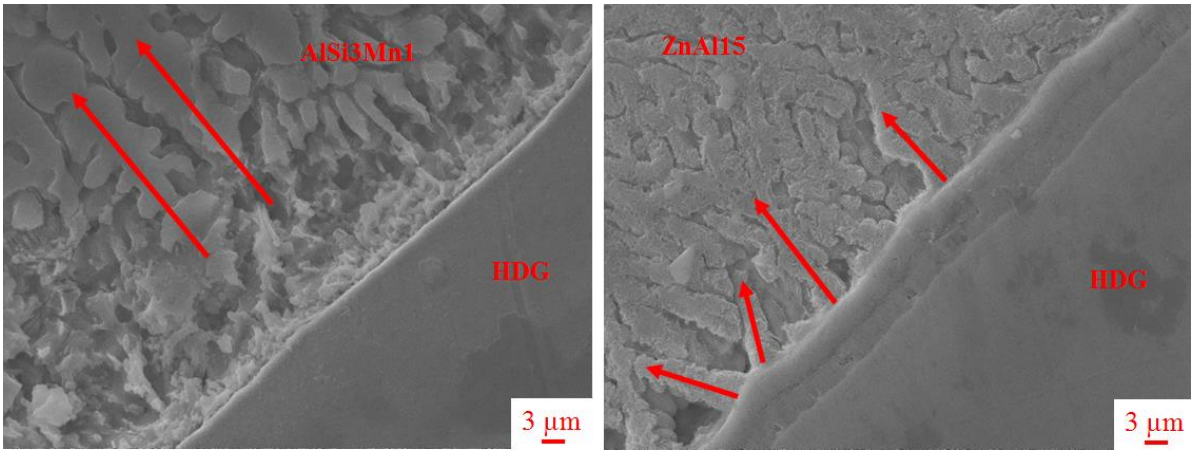

Figure 3.12 The morphology and orientation of solidified dendrites with respect to the steel/brazed bead boundary for Al-based and Zn-based wire.

The hardness of coach peel joints were measured along a profile which includes both base materials and weld seam with the results presented in Figure 3.13. As can be observed for the Al-based filler wires, the micro-hardness of the brazing bead increased with increasing amounts of Si from an approximate hardness of 70 for AlSi3Mn1 and AlSi5 to 110 for AlSi12. The ZnAl15 filler wire weld seam peaked at approximately 115 which becomes comparable to the hardness of the steel substrate.

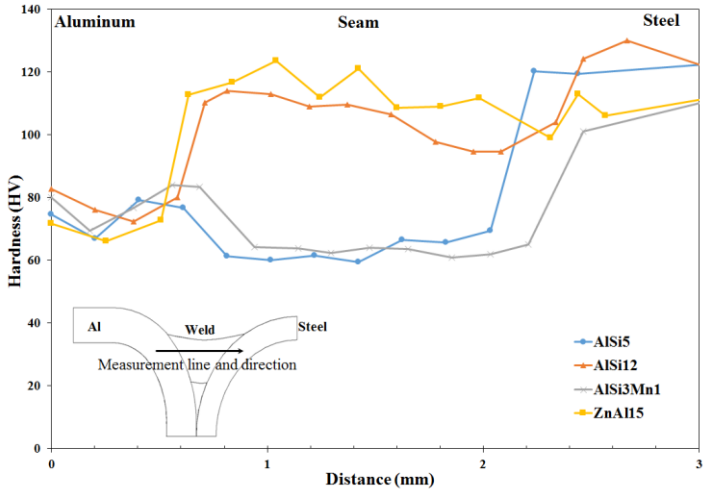

Figure 3.13 Hardness distribution of LWB joints.

3.4.2 Tensile strength

Generally, coach-peel joints of LWB are considered for non-structural applications on the exterior of automotive body; but regardless of this, a certain level of joint strength is expected. From the mechanical perspective, the weld cannot fracture before the panels deform. There is a concern in the mechanical performance of dissimilar materials joints that the presence of IMC layers at the interface between the weld bead and the steel panel may initiate premature fracture typically by the cleavage of the IMC phase.

As seen in Figure 3.14 (a), the joints made with Zn-based filler material exhibited the highest resistance level at approximately 180 N/mm. The resistance of the joints made with the three types of Al-based filler wires fell within a narrow range of each other. Of the Al-based materials, the AlSi3Mn1 filler material exhibited the highest resistance; though, this was paired with having the lowest value in terms of elongation and joints experienced a kind of brittle behavior in comparison to the generated joints by using a filler material with higher Si contents. It is also noted that an increase in Si content enhanced the joint ductility.

All tensile test coupons composed of the Al-based filler materials exhibited fractures at the interface between the weld bead and the aluminum panel as shown in Figure 3.15 (a). The crack has initiated and then propagated along the weld/braze bead and Al6022 substrate interface. With continued extension the coach peel samples continued to bend which alters the loading conditions at the crack tip such that the crack propagation moved into the welded/brazed bead along the growth direction of the columnar dendrites (Figure 3.12), propagated through the interdendritic region and ended with full fracture. In contrast, the higher strength and extension of the coupons welded-brazed with ZnAl15 filler material, drove the tensile test fractures to occur within the base Al6022 substrate (see Figure 3.15(b)). The fractography results (zones 1-2) show more dimples

in the ZnAl15 than in the case of AlSi3Mn1. This can mean that the fracture in joints with Zn-based filler wire was more ductile.

Since the thickness of IMC layer in all type of joints was less than critical value (less than 10µm); therefore, the strength of joints was more dependent on the size of fusion zone and bonding length than the thickness of intermetallic layer. The difference in fusion size and bonding length of joints with Al-based and Zn-based filler materials (Figure 3.8) can be the main reason of their different fracture modes. In order to provide a true comparison of Zn-based vs Al-based filler wire welds with the involvement of actual bonding length, other type of graph is plotted (Figure 3.14 (b)) on this regard. The resistance (load/mm) terminology was altered to load/area where area is a product of brazed joint width and length of wetting between the brazed and Al substrate.

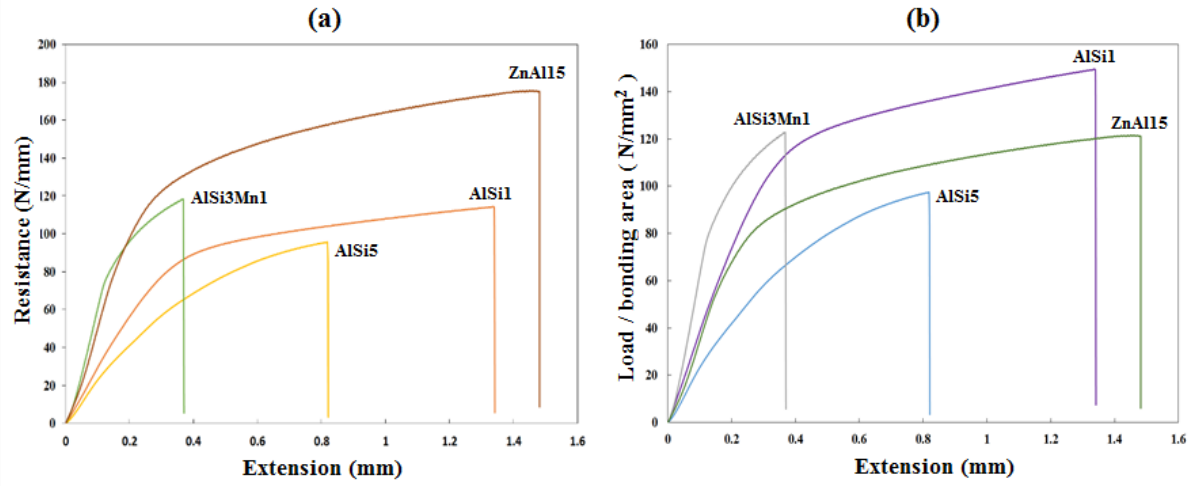

Figure 3.14 (a) Resistance vs elongation, (b) Load/bonding area vs elongation, for the LWB joints with AlSi3Mn1, AlSi5, AlSi12, and ZnAl15 filler materials.

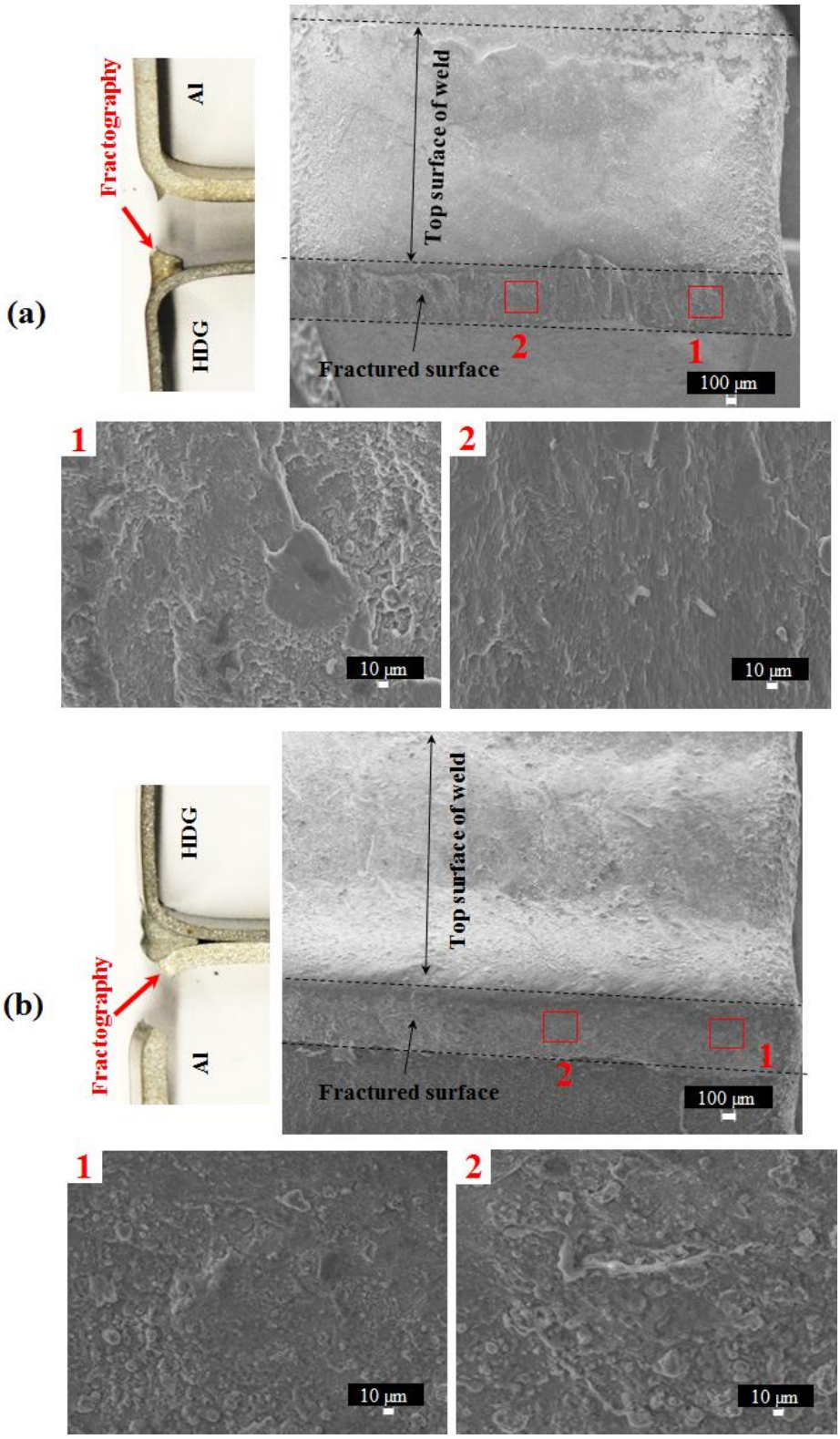

Figure 3.15 Fractured surfaces of tensile coach peel coupons, note differing fracture modes associated with the different filler wire material: (a) AlSi3Mn1, (b) ZnAl15.

3.4.3 Surface roughness

The welds in a coach-peel joint configuration should have a high surface quality in order to avoid the need for post-weld processing prior to painting of the BIW. Wang et al. [23] studied the effect of weld surface roughness on the surface quality of painted panels and found that welded joints should have a surface roughness less than 3µm in order to avoid the need for post-weld processing. To compare the surface quality of welded joints by means of four different wires, the weld beads were scanned using an optical profilometer (Figure 3.16 (a)). The measurements were repeated three times for each type of filler materials. The average value of the surface roughness, expressed as the arithmetical mean height Ra, as well as standard deviation are given in Table 3.10. The ZnAl15 filler wire joint exhibited the highest surface roughness while the lowest surface roughness was achieved by AlSi12 and AlSi3Mn1 wires. The images of beads from top view and captured surface topography of joints also confirmed these observations (Figure 3.16 (b-c)).

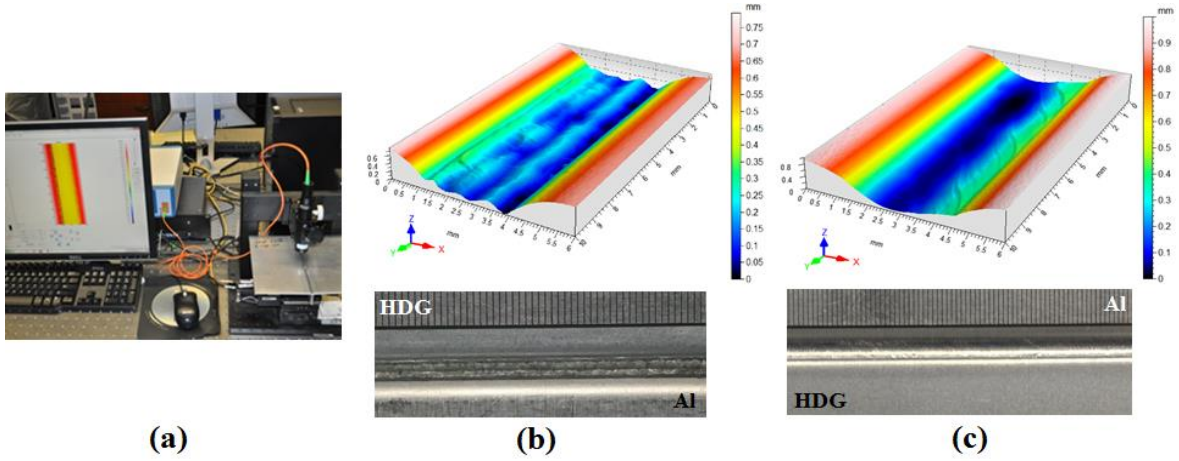

Figure 3.16 (a) Experimental equipment for measuring surface roughness, bead surface and 3D morphologies for (b) ZnAl15, (c) AlSi3Mn1.

Table 3.10 Measured surface roughness of four filler wire materials after welding/brazing using optimum processing parameters.

filler wire type	Surface roughness (Ra) μm	Standard deviation
AlSi12 (Al4047)	0.984	0.19
AlSi5 (Al4043)	1.443	0.13
AlSi3Mn1 (Al4020)	0.917	0.23
ZnAl15	2.83	0.17

3.5 Conclusions

The current study deals with the joining of aluminum alloy 6022 and hot-dip galvanized steel panels in the coach-peel configuration by a twin-spot (side by side) laser beam. The design of experiments and application of RSM in optimizing the process parameters of dissimilar LWB joints with Al-based filler materials were conducted. The welded joints with Al-Si, Al-Si-Mn, and Zn-Al filler wires were investigated to study the effect of alloying elements on surface roughness, mechanical strength, and microstructure of resultant joints. The following conclusions have been drawn:

1. The Box-Behnken statistical design accompanied with the response surface methodology was a simple and efficient method to investigate the effect of LWB process parameters and their interactions on the defined responses.
2. Based on RSM results, increasing the laser power has developed the mechanical resistance and when it comes to surface roughness it has an opposite trend. Welding speed and wire feed rate had minimal negative effects on the mechanical strength, while surface roughness has deteriorated significantly by increasing their levels.

3. The multi-response optimization approach by considering the minimum surface roughness and maximum mechanical strength has introduced the 3.2kW for laser power, 60 mm/s for welding speed, and 70 mm/s for wire feed rate as the optimum processing conditions for joints with Al-based filler wires.
4. The twin spot laser mode can be used to join aluminum and galvanized steel at high processing speed. The generated IMC layer on four different wires was less than the critical thickness (10µm). Among Al-based wires, the addition of Si into the brazed coat hinders the diffusion of Fe from the steel side into the weld, decrease the thickness of IMC. For Zn-based wire, although presence of Zn thickened the IMC, no brittleness effect was observed so that tensile coupons failed from aluminum panel.
5. In terms of mechanical strength the Zn-based filler material has offered the highest resistance about 180 N/mm. Among the Al-based wires, AlSi12 has the best performance with mechanical strength of 120 N/mm and highest elongation value.
6. The use of Al-based filler wires leads to have welds with high surface qualities. The lowest surface roughness was achieved in joints with AlSi3Mn1 wires about 0.91 µm and by using the ZnAl15 as consumable material this value increased to 2.83 µm.

References

[1] K. Martinsen, S.J. Hu, B.E. Carlson, Joining of dissimilar materials, CIRP Annals - Manufacturing Technology, 64 (2015) 679-699.

[2] S. Meco, G. Pardal, S. Ganguly, S. Williams, N. McPherson, Application of laser in seam welding of dissimilar steel to aluminium joints for thick structural components, Optics and Lasers in Engineering, 67 (2015) 22-30.

[3] L. Agudo, D. Eyidi, C.H. Schmaranzer, E. Arenholz, N. Jank, J. Bruckner, A.R. Pyzalla, Intermetallic Fe x Al y -phases in a steel/Al-alloy fusion weld, Journal of Materials Science, 42 (2007) 4205-4214.

[4] J. Lin, N. Ma, Y. Lei, H. Murakawa, Shear strength of CMT brazed lap joints between aluminum and zinc-coated steel, Journal of Materials Processing Technology, 213 (2013) 1303-1310.

[5] J. Yang , Z. Yu, Y. Li, H. Zhang, W. Guo, N. Zhou, Influence of alloy elements on microstructure and mechanical properties of Al/steel dissimilar joint by laser welding/brazing. Welding in the World, 62 (2018) 427-33.

[6] K. Saida, W. Song, K. Nishimoto, Diode laser brazing of aluminium alloy to steels with aluminium filler metal, Science and Technology of Welding and Joining, 10 (2005) 227-235.

[7] G. Filliard, M. El Mansori, L. Tirado, S. Mezghani, C. Bremont, M. De Metz-Noblat, Industrial fluxless laser weld-brazing process of steel to aluminium at high brazing speed, Journal of Manufacturing Processes, 25 (2017) 104-115.

[8] G. Yang, J. Ma, B. Carlson, H.-P. Wang, R. Kovacevic, Effect of laser beam configuration on microstructure evolution and joint performance in laser joining AA 6111 panels, Materials & Design, 123 (2017) 197-210.

[9] C. Mittelstädt, T. Seefeld, D. Reitemeyer, F. Vollertsen, Two-beam Laser Brazing of Thin Sheet Steel for Automotive Industry Using Cu-base Filler Material, Physics Procedia, 56 (2014) 699-708.

[10] Q. Zhou, Y. Rong, X. Shao, P. Jiang, Z. Gao, L. Cao, Optimization of laser brazing onto galvanized steel based on ensemble of metamodels, Journal of Intelligent Manufacturing, (2016) 1-15.

[11] Y. Rong, Z. Zhang, G. Zhang, C. Yue, Y. Gu, Y. Huang, C. Wang, X. Shao, Parameters optimization of laser brazing in crimping butt using Taguchi and BPNN-GA, Optics and Lasers in Engineering, 67 (2015) 94-104.

[12] G. Yang, J. Ma, B.E. Carlson, H.-P. Wang, M.M. Atabaki, R. Kovacevic, Decreasing the surface roughness of aluminum alloy welds fabricated by a dual beam laser, Materials & Design, 127 (2017) 287-296.

[13] Annual book of ASTM standards, metals test methods and analytical procedures, ASTM International, volume 03, 01., in, 2003.

[14] R. Shabadi, M. Suery, A. Deschamps, Characterization of Joints Between Aluminum and Galvanized Steel Sheets, Metallurgical and Materials Transactions A, 44 (2013) 2672-2682.

[15] H. Laukant, C. Wallmann, M. Müller, M. Korte, B. Stirn, H.G. Haldenwanger, U. Glatzel, Fluxless laser beam joining of aluminium with zinc coated steel, Science and Technology of Welding and Joining, 10 (2005) 219-226.

[16] A.M. Milani, M. Paidar, A. Khodabandeh, S. Nategh, Influence of filler wire and wire feed speed on metallurgical and mechanical properties of MIG welding–brazing of automotive galvanized steel/5754 aluminum alloy in a lap joint configuration, The International Journal of Advanced Manufacturing Technology, 82 (2016) 1495-1506.

[17] C. Dharmendra, K.P. Rao, J. Wilden, S. Reich, Study on laser welding–brazing of zinc coated steel to aluminum alloy with a zinc based filler, Materials Science and Engineering: A, 528 (2011) 1497-1503.

[18] S. Ji, W. Yang, F. Gao, D. Watson, Z. Fan, Effect of iron on the microstructure and mechanical property of Al–Mg–Si–Mn and Al–Mg–Si diecast alloys, Materials Science and Engineering: A, 564 (2013) 130-139.

[19] J.L. Song, S.B. Lin, C.L. Yang, C.L. Fan, G.C. Ma, Analysis of intermetallic layer in dissimilar TIG welding–brazing butt joint of aluminium alloy to stainless steel, Science and Technology of Welding and Joining, 15 (2010) 213-218.

[20] T. Murakami, K. Nakata, H. Tong, M. Ushio, Dissimilar Metal Joining of Aluminum to Steel by MIG Arc Brazing Using Flux Cored Wire, ISIJ International, 43 (2003) 1596-1602.

[21] H. Dong, W. Hu, Y. Duan, X. Wang, C. Dong, Dissimilar metal joining of aluminum alloy to galvanized steel with Al–Si, Al–Cu, Al–Si–Cu and Zn–Al filler wires, Journal of Materials Processing Technology, 212 (2012) 458-464.

[22] G. Sierra, P. Peyre, F. Deschaux Beaume, D. Stuart, G. Fras, Galvanised steel to aluminium joining by laser and GTAW processes, Materials Characterization, 59 (2008) 1705-1715.

[23] H.-p.W. Xuesong Wang, Blair E. Carlson, Jianping Lin, Michael Poss and Joshua Solomon, Development of surface evaluation methods for class A welds, in: Sheet Metal Welding Conference XVII, Detroit, 2016.

Chapter 4

INFLUENCE OF LASER BEAM INCLINATION ANGLE ON GALVANIZED STEEL LASER BRAZE QUALITY

4.1 Introduction

Laser brazing is a widely used process for joining closure panels in automotive manufacturing exemplified by joints such as the upper to lower panels of a liftgate or the roof to body side outer panels. These panels are typically zinc coated for improved corrosion protection and the brazed joints are visible to consumers. Thus, it's crucial to ensure stability of the brazing process and generate defect-free joints with high seam quality. However, in brazing zinc-coated steel sheets process instabilities can occur which cause defects requiring post-processing steps for cleaning and repair. Typical defects in galvanized steel laser brazed joints are surface pores, spatter, un-melted or/and one-sided melt wire, rises, open-out holes, short and long skips, and saw tooth surfaces, refer to Figure 4.1.

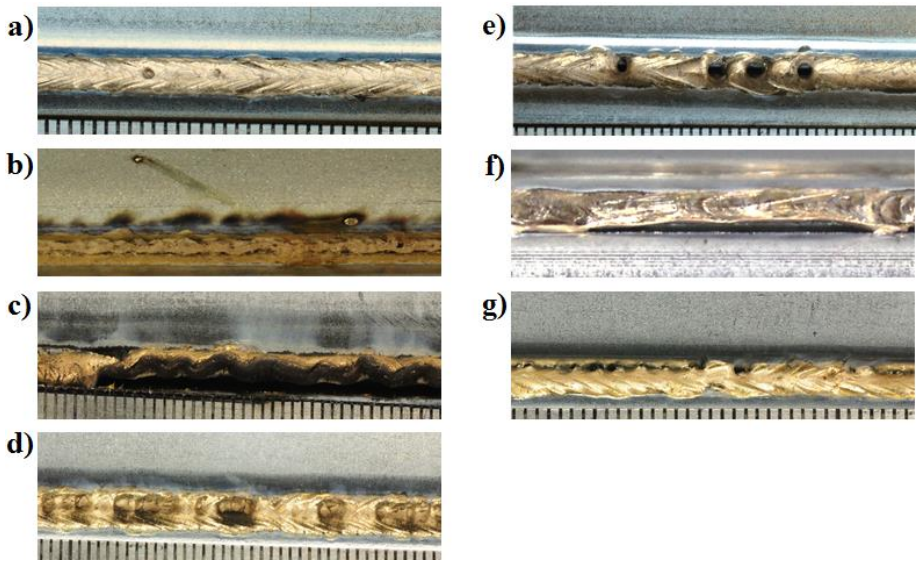

Figure 4.1 Typical imperfections in laser brazing process: (a) surface pores; (b) spatter; (c) single-sided wetting; (d) rises; (e) open-out blow holes; (f) skip; (g) saw tooth surface. [Note: experimental observations]

The process instabilities can be attributed to process variations due to the external trigger events and the existence of low boiling elements such as zinc coating. Ungers et al. [1] investigated the root cause of some braze defects such as pores and skips. They articulated that unsteady process parameters such as laser power, wire feed speed, and brazing speed could disturb the stability of molten pool dynamics and eventually cause seam imperfections. Grimm [2] studied the effect of laser beam offset on the beam quality. His experimental observations revealed that the occurrence of an asymmetric temperature profile in the process directly influenced the wetting behavior and led to defects such as unmelted and/or one-side melted wire. Frank et al. [3] reported that some of generated open-out holes during the laser brazing process could be fully closed in the case of consistent wire feeding. In addition, Lu et al. [4] emphasized the significant effect of insufficient wire feeding in causing process instability.

The influential role of zinc coating on the wetting behavior of molten filler material on steel substrate was studied for laser braze joints [5]. Experimental observations by Koltsov et al. [5] verified the significant role of the zinc layer in providing more fluidity and facilitating the wetting behavior of molten CuSi3 drops. The lower wetting angle was measured in zinc coated substrates as an indicator of enhanced wetting behavior in comparison to a bare steel substrate. The zinc existence not only helped the wetting performance but also prevented direct laser irradiation on the steel substrates, which would have caused unnecessary fusion of substrates and even thermal distortion especially in long braze joints. However, zinc has a boiling point of 907 °C which is lower than the melting range of copper-based filler wire, 965 – 1032 °C and as such is the predominant cause of laser brazing process instability for zinc coated steels in addition to process variations. Kimura et al. [6] conducted experimental studies to understand the mechanism of process defects. The pressurized zinc vapor is created during the brazing process and disrupts the

melt pool stability and even permeates the molten material resulting in braze defects. They concluded that pressurized zinc vapor expelled the molten filler material and resulted in seam defects such as open-out holes, porosity, and spatter.

In laser welding of lap-joint galvanized steel panels, the evaporation of zinc layer at the faying surface and through the molten pool caused the instability of process and formation of pores and blowout holes [7]. To overcome this challenge some techniques have been introduced to reduce the disruption to the welding process. Chen et al. [8] and Graham et al. [9] propesed methods to provide routes for degassing the zinc vapor by creating a pre-set gap between the weld plates and pre-drilled holes in the bottom plate, respectively. However, these methods are not applicable to laser brazing processes since zero-gap part fitting is required for a high-quality seam and intentional holes in the bottom sheet are undesirable. Zinc removal is another successful method where the zinc layer in the process area is evaporated by application of a preheating pass [10]. However, this method requires an additional process and is relatively expensive for automotive applications.

Another approach to developing a robust laser brazing process free of sporadic imperfections, is the application of multi-beam welding. The twin-spot laser beams in the form of two separate laser optics [11] and one single beam split into dual beams [12] have been studied. The hypothesis of a multi-beam approach is to preheat the adjoining panels for consistent brazing conditions. Preheating helps to clean the panel surface which improves wetting. The most recent study was conducted by Reimann et al. [13] to investigate selective zinc removal by means of triple laser beams. In this method, two small leading beams evaporated the zinc coating prior to wetting and at the substrate area where the edges of the weld seam would form. The trailing high-power beam was dedicated to melting of the filler material. Although high quality and straight

edged braze joints were reported with application of the three beams compared to a single beam method, additional complexity was added to the laser brazing process by introducing extra process parameters such as laser power of the two leading beams and the lateral distance between the two laser beams.

In this study, the laser beam inclination angle in a single beam method was studied for designing a robust laser brazing process for galvanized steel panels with neither additional complexity nor equipment. The change of laser beam inclination angle was achieved by changing beam work angle and travel angle. The energy distribution on the wire and substrate were hence affected and achieved a preheating or post-heating mode. Brazing tests with different beam inclination angles were conducted to study their effect on braze process stability and braze quality. The process stability was captured by high-speed videos. Furthermore, a multi-physics simulation model was developed to simulate the brazing process and provide understanding of the process instability. Finally, the effect of laser beam inclination angle on the seam quality was analyzed based upon visual inspection of the type of defect and surface roughness, high-speed videos of the brazing process, numerical simulation, and cross-sectional dimensions of the braze joint.

4.2 Experimental procedure

4.2.1 Materials

In this study Hot-Dip Galvanized (HDG) and electro-galvanized (EG) low carbon steel were used as the base material. The thickness of steel sheet was 0.65 mm and the average zinc coating thickness was 10 μm. The 600 mm length experimental braze joint was composed of two coupons butted up to one another wherein one coupon geometry simulated a roof panel and the other a body side outer. The roof and body side coupons form a roof joint and have a 5mm height-offset to represent the condition of a real roof joint geometry. The studied coupon geometry fully clamped

in the welding fixture is presented in Figure 4.2(a). A CuSi3Mn1 filler wire with diameter of 1.6 mm was used in all experiments. The chemical composition of the filler wire is provided in Table 4.1.

Table 4.1 Chemical composition of CuSi3Mn1 wire.

Si	Mn	Cu	Al	Sn	Zn	Pb	Fe	P	Other total
2.8 – 2.95	0.75 – 1.5	Bal.	<0.01	<0.20	<0.20	<0.02	<0.3	<0.02	<0.40

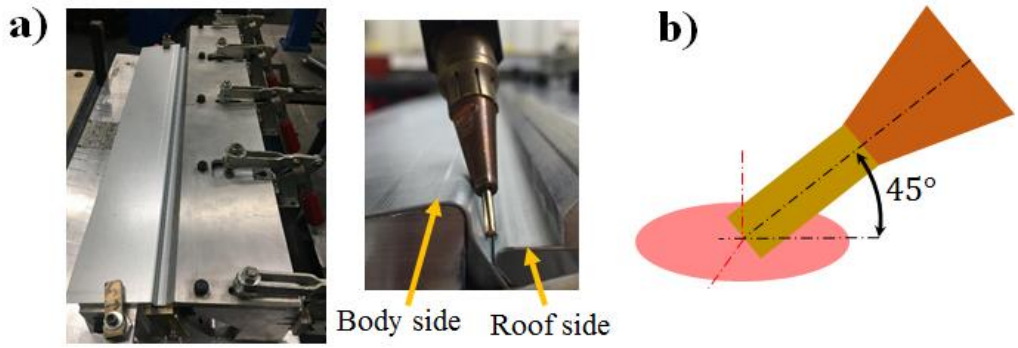

Figure 4.2 (a) Top and side view of fully clamped coupons in the welding fixture, (b) 3D laser beam and filler wire relationship.

4.2.2 Experimental method

The experiments were designed to mimic automotive laser brazing processes in terms of process variables and brazing equipment. A diode laser with 960-1070 nm wavelength in continuously emitting, CW, mode and a maximum power of 6 kW was selected as the laser source. The laser spot had a diameter of 3.2 mm in the focal plane was delivered by a Scansonic brazing head. The brazing head was mounted to a six-axis robot to provide the movement. The 45º wire feeding module was mounted onto the brazing head. While brazing, the wire axis and laser beam maintains an angle of 45º regardless of the beam inclination angle. In all experiments, air plume suppression in coaxial configuration with a flow rate of 8 l/min was provided. Figure 4.2(b) schematically demonstrates the position of the laser spot and filler wire when they are aligned with no offset. Note that the center of the beam spot coincides with the center of the wire tip.

The laser beam direction was changed by adjusting travel angle, TA, and work angle, WA. The schematic illustrations of TA and WA are presented in Figure 4.3. In addition to the main brazing process parameters; laser power, wire feeding speed, and robot speed, TA and WA were also considered as influential factors that not only could affect the final quality of joints but also reduce the occurrence of spatter. The values of the laser brazing process parameters to be tested are listed in

Table 4.2. The following were fixed; laser power at 3.8kW, wire feed speed at 60mm/s, and braze speed at 65 mm/s. The travel angle was tested at values ranging from -30˚ to 20˚, and the work angle ranged from -10˚ to 5˚. Bead-on-plate test were also conducted to investigate the effect of different zinc coatings on the laser brazing process. In this regard, the processing head was positioned perpendicular to the substrate surface and used without additional filler material.

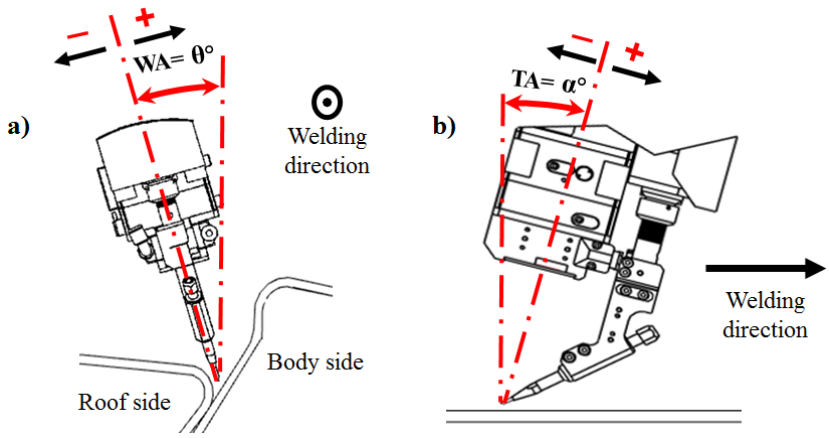

Figure 4.3 Schematic illustration: (a) work angle (WA); (b) travel angle (TA).

Table 4.2 Brazing conditions.

Parameters	Value
Laser power (kW)	3.8
Wire feed speed (mm/s)	60
Braze speed (mm/s)	65
Travel angle (deg)	-30˚ – 20˚
Work angle (deg)	-10˚ – 5˚

A high speed camera was used to record the laser process during brazing with a frame rate of 4000 fps. The molten pool area was illuminated by a pulsed high frequency diode laser with power of 500 W and wavelength of 810 nm. A narrow bandwidth IR filter ($798 < \lambda < 820$ nm) was mounted in front of the camera. A schematic illustration of the monitoring set up is shown in Figure 4.4.

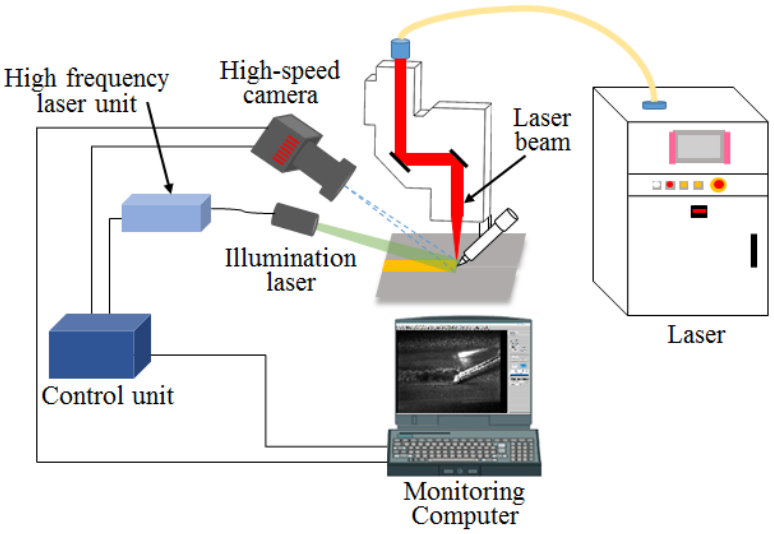

Figure 4.4 Schematic view of in-situ monitoring system.

The laser beam energy density distribution at focal plane position was measured by a PRIMES focus monitoring system where a two-dimensional contour plot and a three-dimensional top hat plot can be observed in Figure 4.5(a-b).

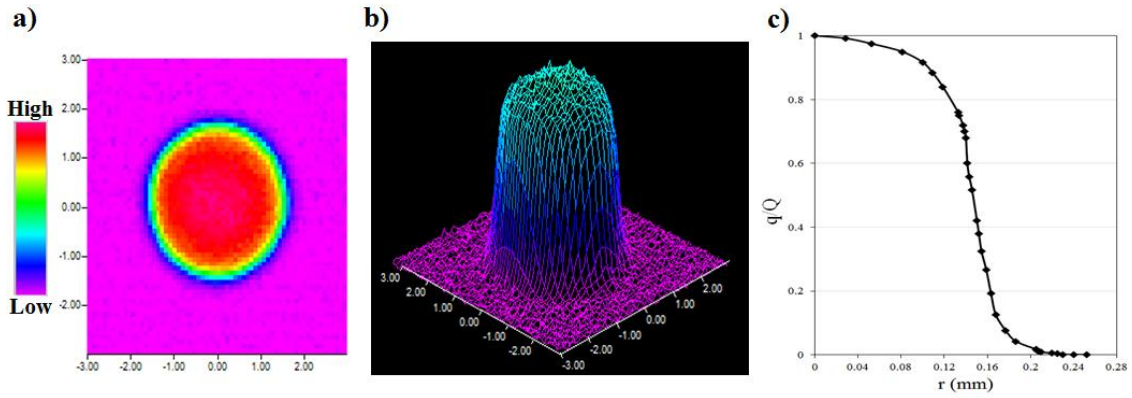

Figure 4.5 Laser beam energy intensity distribution in focal plane: (a) 2D energy density contour, (b) 3D energy density plot, (c) normalized energy distribution of a laser beam along the radial direction.

4.2.3 Characterization

Each weld test had a unique combination of work angle and travel angle which were applied to fabricate two separate braze joint geometries. The first braze joint consisted of a single pass 600 mm long braze seam whereas the second joint consisted of three consecutive 160 mm long braze seams separated by a gap of approximately 30 mm. The braze seam quality and process stability were evaluated based upon visual inspection, bead cross-section, process monitoring, and metallographic analysis. Visual inspection was used to quantify braze defects such as spatter, open-out holes, pores, skips, and rises. The surface roughness was measured by Keyence VR-3100 at three areas of interest in the coupons with long braze seams (see Figure 4.6(a)) and averaged results were reported. For cross-sectional observations, three samples were transversely cut at the middle of three short brazes as shown in Figure 4.6(b). The hot mounted samples were first polished with increasingly finer paper (240-2000 grit) followed by subsequent polishing steps with diamond paste of 9, 6, and 3 μm particle size. The polished cross-sections were ultrasonically cleaned before chemical etching. The prepared samples were analyzed with Leo-Zeiss 1450VPSE scanning

electron microscope equipped with Energy Dispersive Spectroscopy (EDS) to characterize the cross-sectional dimensions, microstructure and composition of the brazed joints.

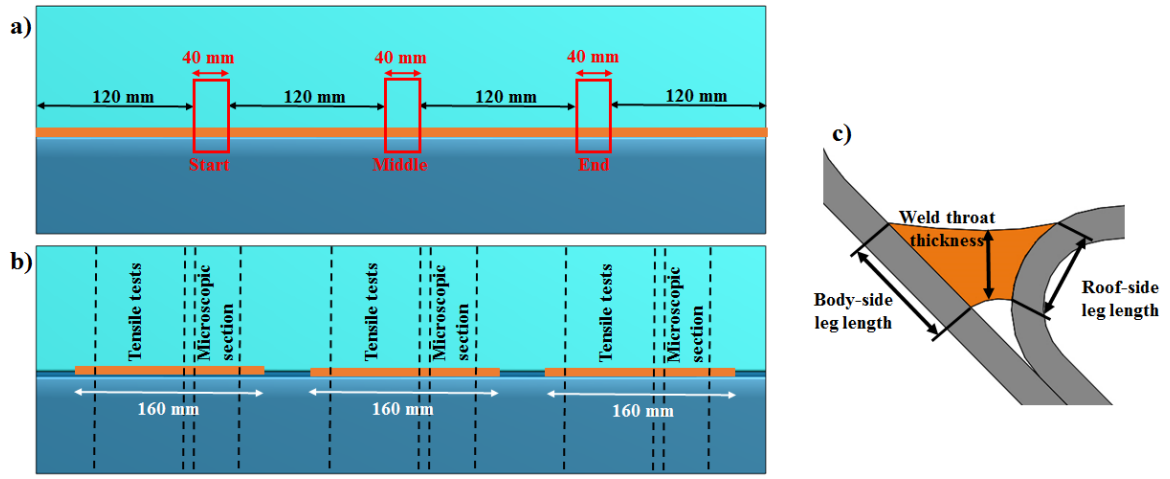

Figure 4.6 (a) Areas of interest for surface roughness measurement at the start, middle and end of the long brazed coupon, (b) samples prepared for microscopic observation and mechanical tests, (c) geometrical features of a laser braze joint cross-section.

The cross-sectional dimensions of a brazed seam are critical to joint strength. Figure 4.6(c) illustrates the important geometrical features of the braze cross section, where the throat thickness is the shortest distance between the weld root and weld face. The strength of brazed coupons was evaluated by tensile testing. Each tensile test was repeated three times and tests were terminated upon fracture initiation. The tensile tests were carried out at room temperature in accordance with ASTM E 8M-01.

4.3 Process simulation model

4.3.1 Computational domain

A multi-physics simulation model was developed with the purpose of studying melt behavior in laser brazing under various process conditions. The computational domain is schematically shown in Figure 4.7. The critical domain along the laser scanning zone was meshed into uniform

cells of 0.06 mm, and gradually coarsened into two sides as it gets further away from the laser zone. The total number of cells is 917,446. Note that in the experiments the substrate was stationary, while the laser beam and feed wire were moved along the seam path. In the simulation, a moving inlet boundary condition that continually feeds the wire was difficult to achieve numerically. Instead, the filler wire and laser beam were set stationary with the panels translating at the brazing process speed. The thermo-physical material properties used for the base and filler materials are listed in Table 4.3.

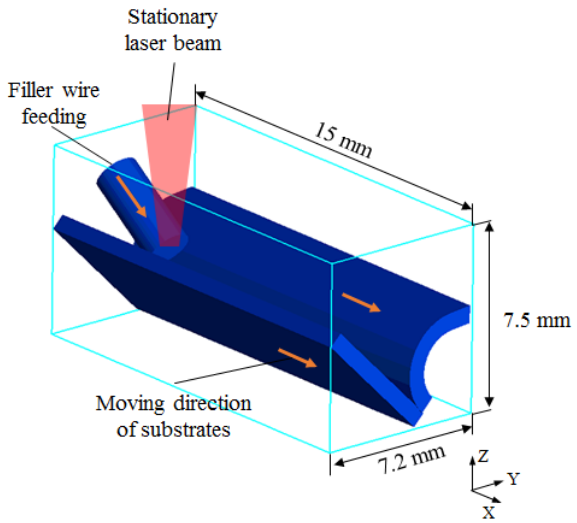

Figure 4.7 Schematic of computational domain with wire feeding.

Table 4.3 Thermo-physical properties of base and filler materials and related parameters used in the simulation [13].

Nomenclature	Unit	Value	
		Filler material	Panels
Density	Kgm^{-3}	8435	7854
Specific heat	$JKg^{-1}K^{-1}$	308	468
Thermal conductivity	$Wm^{-1}K^{-1}$	30.6	66.9
Surface tension	Nm^{-1}	1.25	1.79
Dynamic viscosity	Pas	0.00507	0.0067
Melting temperature	K	1210 - 1305	1800
Latent heat	JKg^{-1}	1.71×10^5	2.77×10^5

4.3.2 Mathematical Model

4.3.2.1 Governing equations

In analyzing the molten pool flow of laser brazing process four equations (mass, momentum, energy conservations and Volume of Fluid) are required to be solved to determine the distribution of temperature, velocity, pressure, and free surfaces. To simplify the mathematical model, the flow was considered to be laminar and incompressible with Newtonian viscosity. The main governing equations were discussed as below:

- Mass conservation equation (Continuity):

$$\rho \nabla . \vec{u} = m_s \tag{4-1}$$

where, $\vec{u} = (u, v, w)$ is the velocity field, ρ is the density, and m_s is the mass source term from the adding wire.

- Momentum conservation equation (Naiver-Stokes):

$$\frac{\partial \vec{u}}{\partial t} + \vec{u} . \nabla \vec{u} = -\frac{1}{\rho}\nabla P + \mu \nabla^2 \vec{u} - K\vec{u} + \frac{\dot{m}_s}{\rho}(\overrightarrow{u_s} - \vec{u}) + \rho \vec{g} - \rho \vec{g} \beta (T - T_0) \tag{4-2}$$

where, P, μ, K, $\overrightarrow{u_s}$, $\vec{g}$, T, T_0, and β represent the pressure, dynamic viscosity, drag coefficient in mushy zone, velocity of mass source, gravity vector, molten pool temperature, reference temperature, and coefficient of thermal expansion, respectively. The porous media drag concept was considered to model the solid to liquid phase change [14]. The flow in the mushy zone followed the Carman-Kozeny equation as a function of solid fraction. In Darcy type drag model as given in Eq. (4-3) the coefficient C is zero for temperatures beyond liquidus point and is effectively infinite in solid phase. In Eq. (4-3) the C is a constant reflecting the morphology of mushy zone and f_s is the solid fraction. The last term in the right hand side of Eq. (4-2) is the Boussinesq approximation for simulating the buoyancy force.

$$K = C\frac{f_s^2}{(1-f_s)^3} \tag{4-3}$$

- Energy conservation equation:

$$\frac{\partial h}{\partial t} + \vec{u}.\nabla h = \frac{1}{\rho}\nabla.(k\nabla T) + S_h \tag{4-4}$$

here, h is the enthalpy, k is the thermal conductivity, T is the temperature, and S_h is the energy source due to added mass. The energy-temperature relationship was used to consider the solid-liquid phase transition. This enthalpy-based continuum model is given in Eq. (4-5) where, ρ_s and ρ_l are the solid and liquid density, respectively; C_s and C_l are the specific heat at a constant volume of the solid and liquid phases, respectively; T_s and T_l are the solidus and liquids temperatures, respectively; and ΔH is the latent heat of fusion.

$$h = \begin{cases} \rho_s C_s T & (T \le T_s) \\ h(T_s) + \Delta H\dfrac{T-T_s}{T_l-T_s} & (T_s < T \le T_l) \\ h(T_l) + \rho_l C_l (T-T_l) & (T_l < T) \end{cases} \tag{4-5}$$

- Volume of Fluid (VOF) equation:

$$\frac{\partial F}{\partial t} + \nabla.(uF) = 0 \tag{4-6}$$

A VOF equation is a type of continuity equation that represents a conservation of volume of fluid (F). F is a step function that is equal to one when the control volume or cell is filled up with fluid and zero when the control volume has no fluid. The cells with F values between 0 and 1 were used to track the free surfaces.

4.3.2.2 Laser model

The beam scan of the diode laser in focal plane yielded a top-hat energy distribution profile (Figure 4.5). It was used to model laser energy in Flow3D analysis. The normalized energy distribution curve along the beam radius direction at the focal plane is plotted in Figure 4.5(c).

With a grid size of 0.06mm in the melt area, there were 4 cells to represent the curve in Figure 4.5(c).

Laser beam reflection and absorption are the main phenomena modeled to represent the laser-material interaction in the laser brazing process. The laser beam was discretized into multiple energy rays and their multi-reflection on the material surfaces was considered. Ray-tracing algorithm was used in Flow-3D to follow each ray and calculate its multiple reflections on free surfaces [15]. In each reflection, a certain percentage of ray energy was absorbed by the material surface and the remaining energy was reflected and used as an input ray for subsequent surfaces. The Fresnel absorption model was used to calculate the absorptivity. The multiple reflections continued until the reflected energy was no more than 1% of the initial ray energy. In the Fresnel model the absorption rate and direction of reflected ray can be calculated as a function of laser beam incident angle and laser-dependent and material-dependent coefficients by the following equations:

$$X_{R(n)} = X_{I(n)} - 2(X_{I(n)}.N_{(n)})N_{(n)} \quad (4\text{-}7)$$

$$\alpha(\emptyset_{(n)}) = 1 - \frac{1}{2}\left(\frac{1+(1-\varepsilon\cos\emptyset_{(n)})^2}{1+(1+\varepsilon\cos\emptyset_{(n)})^2} + \frac{\varepsilon^2 - 2\varepsilon\cos\emptyset_{(n)} + 2cos^2\emptyset_{(n)}}{\varepsilon^2 + 2\varepsilon\cos\emptyset_{(n)} + 2cos^2\emptyset_{(n)}}\right) \quad (4\text{-}8)$$

where n, $X_{I(n)}$, $N_{(n)}$, and $X_{R(n)}$ are the nth reflection calculation, direction of nth incoming ray, surface normal, and direction of nth reflected ray, respectively. The $\alpha(\emptyset_{(n)})$ denotes the absorption rate, ε is coefficient determined by laser type and material properties, and $\emptyset_{(n)}$ is the angle between the nth incoming ray and nth surface normal.

4.3.2.3 Boundary conditions

To achieve the energy balance on the top free surface, the heat flux of irradiated laser beam and thermal dissipation by convection and radiation were considered by Eq. (4-9).

$$k\frac{\partial T}{\partial n} = q_L - h_c(T - T_0) - \sigma\varepsilon_r(T^4 - T_0^4) \tag{4-9}$$

where k is the thermal conductivity, n is the normal vector to the local free surface, $q_L$is the laser surface heat flux, h_c, σ, and ε_r are convection coefficient, Stefan-Boltzmann constant, and emissivity, respectively. The remaining surface was modeled by natural convection.

In laser brazing, the melt surface is held in place by pressure upon the melt surface derived by surface tension and shear forces as expressed in the following equation:

$$-P + 2\mu\frac{\partial V_n}{\partial n} = \frac{\gamma}{R} \tag{4-10}$$

where, P is the pressure on the free surface, γ and R are the surface tension coefficient and radius of surface curvature, respectively. The second term on the left side in Eq. (4-10) describes the shear stress on the melt pool by Newton's viscosity law.

4.3.3 Numerical procedure

The simulation domain was discretized into small rectangular cells and Finite Volume Method was used to solve the governing equations. The commercial software Flow3D used the following steps to calculate the variables:

1. Explicit method was utilized to solve the Naiver-Stocks equation, Eq. (4-2).
2. To satisfy the mass continuity equation, Eq. (4-1), the Generalized Minimum Residuals (GMR) method was used to iteratively calculate the pressure at each cell. The induced velocity variations due to pressure changes were added to the computed velocities in step 1.

3. The energy equation, Eq. (4-4), was solved by the implicit option to calculate the temperature field.
4. Volume of fluid equation, Eq. (4-6), was solved to track the free surface and provide the new fluid configuration.

4.4 Results and discussion

4.4.1 Effect of different zinc coating

The main imperfections in laser brazing process (see Figure 4.1) resulted from various external trigger events that will be discussed in following sections. Besides the process instabilities and external events, the type of zinc coating could be considered as the hidden cause in spattering and wavy appearance of laser brazed seams. The experimental observations in dissimilar laser brazing of aluminum to galvanized steel (section 2.4.4) have shown the difference in edge straightness of brazed joints with electro-galvanized (EG) and hot-dipped galvanized (HDG) coatings. However, the effect of zinc coating were not analyzed as the influential factor in the formation of seam imperfections. Therefore, in this chapter the effect of different zinc coatings was studied before going through the effects of external trigger events and laser beam inclination angle on the robustness of laser brazing process.

To investigate the effect of different types of zinc coating the bead on plate experiments were conducted at (LP=1.6 kW and BS=50 mm/s) and brazing tests were done at (LP=3.8 kW, BS=65 m/s, WFS=60 mm/s). The typical cross section of coatings in Figure 4.8 is shown a relatively uniform coating thickness across the surface in EG; whereas, a varied thickness across the surface was observed in HDG coating. Marder [16] provided more details on the microstructure difference of zinc coatings. HDG zinc coatings show a zinc spangle structure, have an intermetallic Fe2Al5 inhibition layer and various Fe-Zn-phases at the steel-zinc interface, whereas EG zinc

coatings have a steel-zinc interface without extensive intermetallic phases and show a homogenous microstructure.

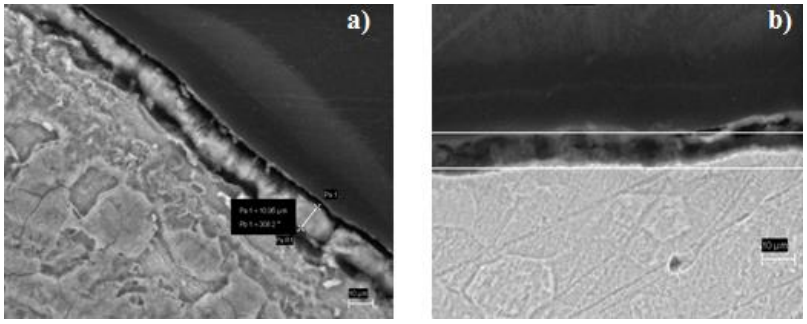

Figure 4.8 Cross-sectional view of zinc coatings: (a) EG, (b) HDG.

High speed imaging of bead on plate experiments clearly displayed the different behavior of EG and HDG coatings. Representative images are shown in Figure 4.9. In hot-dip galvanized substrates the eruptive evaporation of zinc coating and burst of particles were noticeable in the zone ahead of the laser beam. However, the evaporation process at electro-galvanized substrates was continuous and accompanied by the emission of fumes. EDX compositional analysis of end craters in bead on plate tests showed than zinc vaporization zone in front of the laser beam in EG substrates was wider (about two times) than in HDG substrates. This could be attributed to the lower reflectance of matte EG surfaces. SEM images of typical end craters are provided in Figure 4.10.

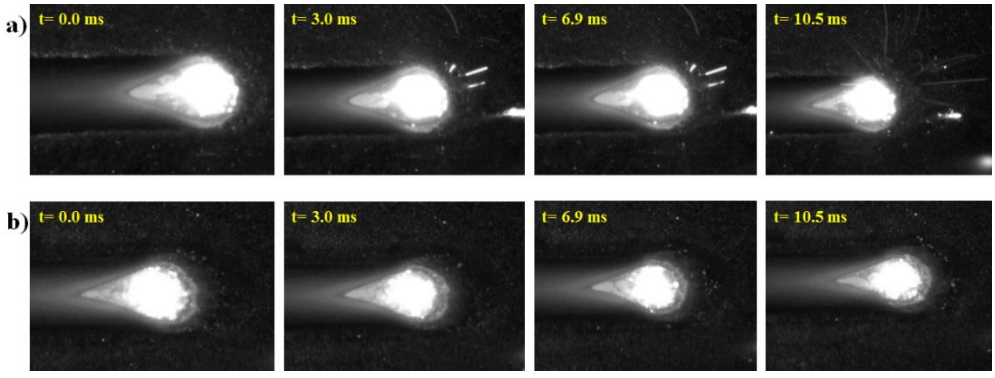

Figure 4.9 Successive images of bead-on-plate tests: (a) HDG, (b) EG.

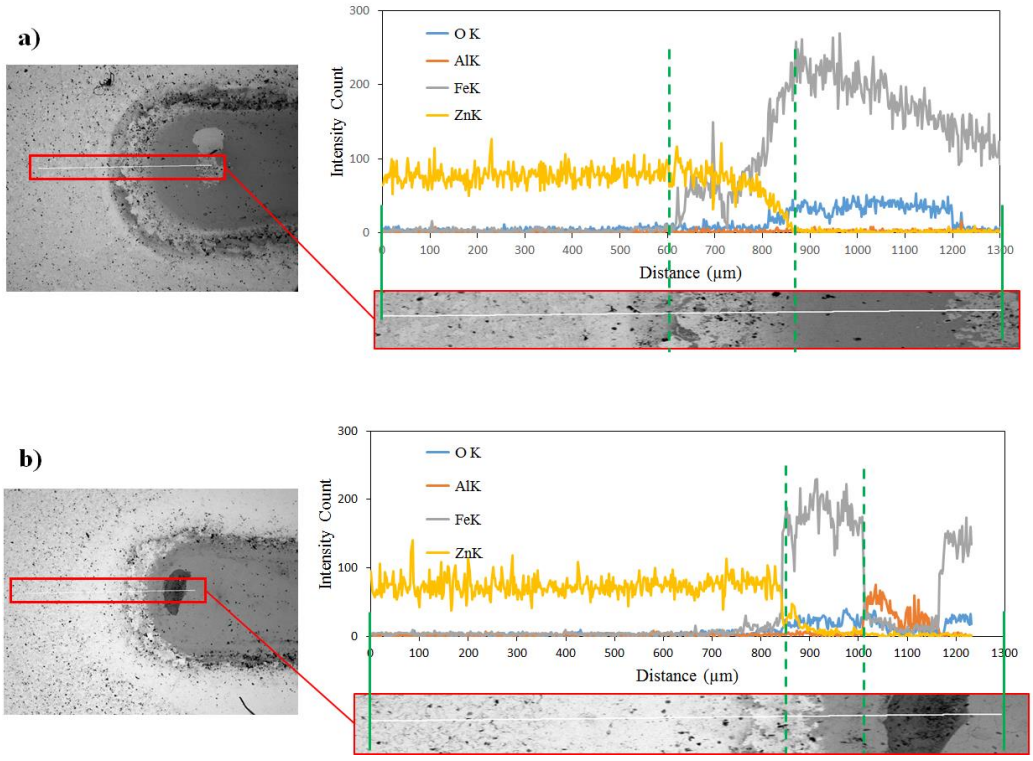

Figure 4.10 SEM micrographs and EDX analysis of end craters of bead-on-plate tests: (a) EG, (b) HDG.

Further comparison of different coatings was continued in laser brazing of roof joints by high speed imaging. A closer look at the joining process showed an occasional occurrence of flaky breakage in zinc coating of hot-dip galvanized coating. The broken coating moved toward the center of molten pool in pulses and resulting a wavy in wavy wetting line and braze edges. However, a continuous dissolution of zinc coating and straight seam edge was observed in electro-galvanized coating. A series of successive images in Figure 4.11 are shown the occurrence of zinc breakage at the wetting line of HDG substrate. This phenomena can be attributed to the morphological and compositional structure of galvanized zinc coatings. The existence of intermetallic layer in HDG coating was explained by Culcasi et al. [17] that the bath of molten zinc used for the hot-dip galvanizing process usually contains about 0.2 at.% of aluminum. This leads to the generation of Fe2Al5 and various zinc-iron-phases at the interface between the steel

substrate and the zinc during the hot-dip galvanizing process. These IMC layers create a firm transition layer between the substrate and the zinc coating. As some of the IMC phases are brittle, the crack formation within the zinc coating is expected. Nevertheless, in EG coated substrates no extensive transition zone of LMCs is formed between the steel substrate and the zinc coating and the crack formation at the interface is not probable.

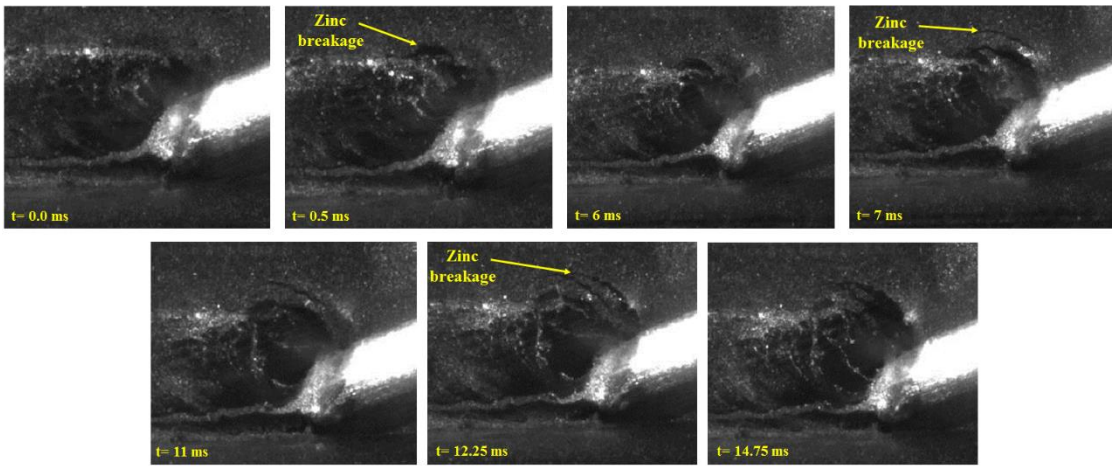

Figure 4.11 Intermittent breakage of zinc coating and wavy seam edge in laser brazing of HDG substrates.

In summary, the comparison of electro-galvanized and ho-dip galvanized coting types from two experimental perspectives were conducted. The eruptive evaporation of zinc, burst of particles ahead of the processing area, and zinc coating breakage were made the HDG coating as the challenging type of substrate for laser brazing process. Therefore, hot-dipped galvanized steel was used as the base material for the rest of investigation in this chapter.

4.4.2 Visual analyses

The processing parameters defined in Table 4.2 were tested with a travel angle of 10º and work angle of 5º. To study the process window, the braze speed and filler wire feed speeds were changed in increments of 10 mm/s and the laser power increased in increments of 500 W. A process

window graph was obtained with respect to laser power, brazing speed, and wire feed speed, refer to Figure 4.12. The green domain indicates the combination of process parameters which led to acceptable braze seam quality. The acceptable braze seam was defined by surface quality and cross-sectional dimension metrics. The effect of wire feed speed or braze speed on cross-section and surface quality are presented in Figure 4.13. Even though the brazed seam produced with a braze speed of 85 mm/s visually looks acceptable, the cross-sectional view illustrates a weak joint with a connection width of only 0.38 mm. The measured cross-sectional area exhibits a reduction from 3.1 mm^2 to 1.9 mm^2 when the braze speed increased from 45 mm/s to 85 mm/s, refer to Figure 4.13(b). While the laser power and braze speed were kept unchanged with a line energy of 58.4 J/mm, increasing wire feed speed from 40 mm/s to 80 mm/s changed the seam surface quality and cross section dimensions.

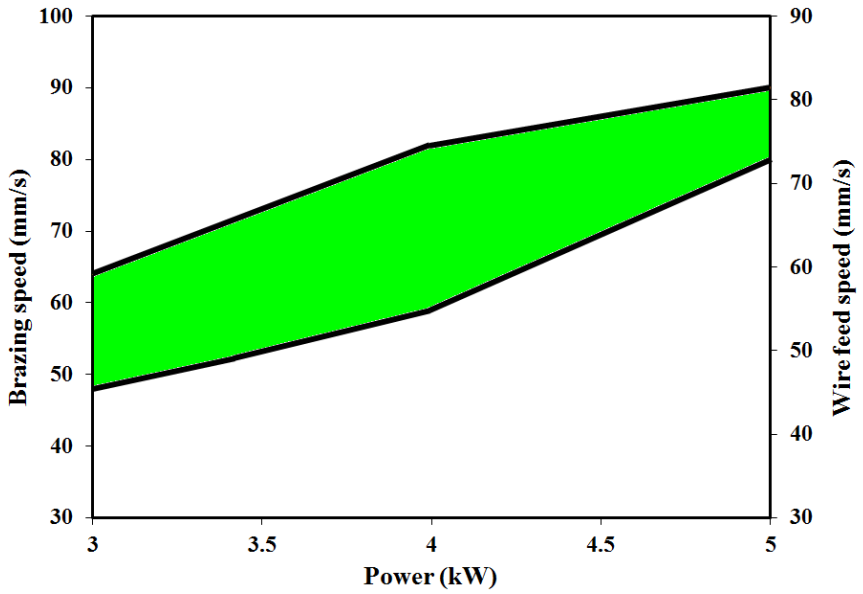

Figure 4.12 Process map of the laser brazing window for HDG steel coupons.

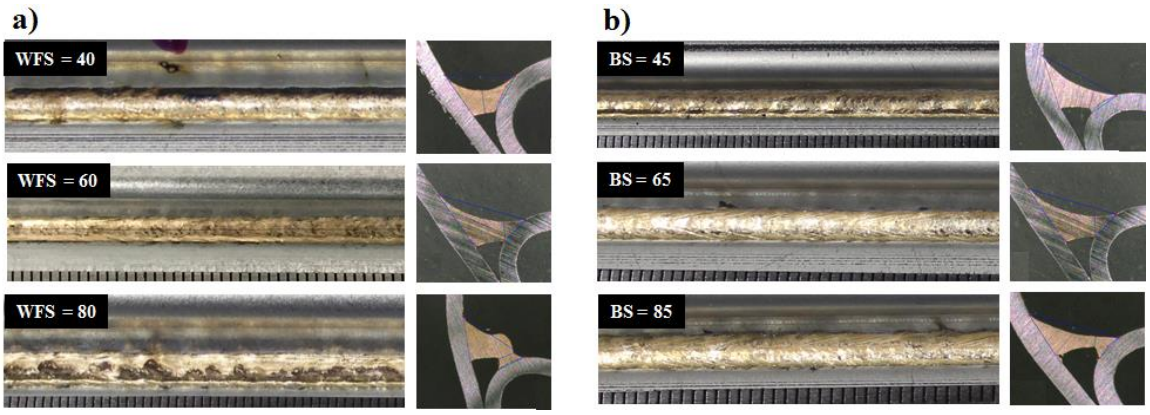

Figure 4.13 Surface appearances and cross-sectional images of laser brazed joints with LP=3.8 kW: (a) BS=65 mm/s, (b) WFS=60 mm/s.

Based on the results in brazing capability graph (Figure 4.12), the laser power, LP, braze speed, BS, and wire feed speed, WFS, were set at LP=3.8 kW, BS=65 mm/s, WFS=60 mm/s, and were consistently applied in subsequent experiments. The travel angle was tested at 6 levels; -30º, -20º, -10º, 0º, 10º and 20º, and the work angle was tested at four levels; -10º, -5º, 0º and 5º to study their effects on process robustness. To protect the optics from back-reflection damage, the work angle was kept constant at 5 degrees when studying the effect of travel angles. The travel angle was set at 10 degrees when studying the effect of work angles. The number of imperfections in brazed seams of 480 mm total length were inspected visually and the results are summarized in Table 4.4. The highest number of blow-out holes was generated with negative travel angles. When the travel angle was positive, this type of defect was eliminated. Tool axis force, wire feed force and wire feed angle are the main factors affected by the change of travel angle. As schematically depicted in Figure 4.14 of negative TA angles, the wire feed module becomes almost perpendicular to the weld seam. The dominancy of vertical force component leads to a high frictional force from the panel to the wire tip that prevents smooth movement of the wire on the joint surface. The highest number of spatter was counted when travel angle and work angle were 0º and -10º,

respectively. The increasing trend in the number of spatter and surface pores was observed when varying the work angle from the body side to the roof side.

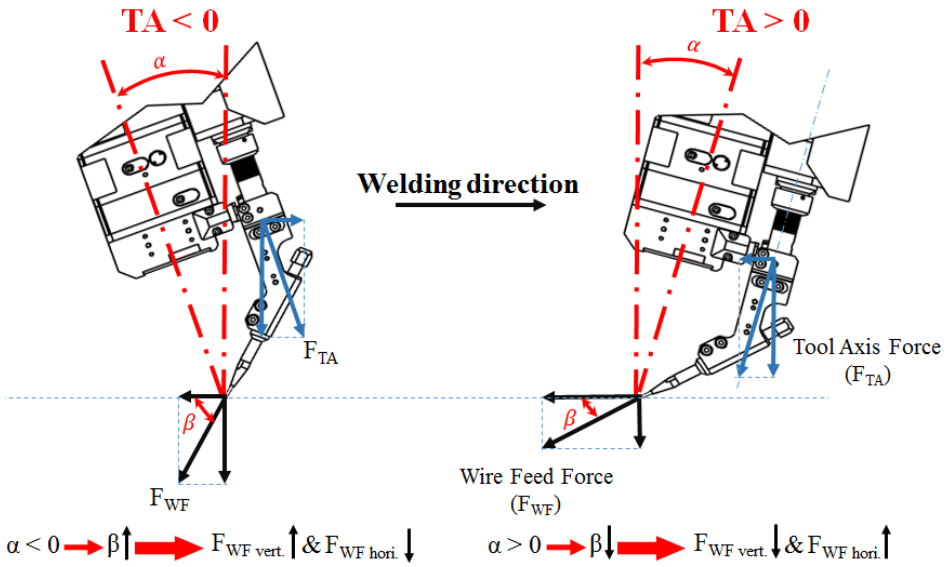

Figure 4.14 Schematic representation of tool axis and wire feed forces.

Table 4.4 Type and number of captured defects in visual inspected samples.

Tilting angles		Spatter	Open-out hole	Surface pore	Rise
Travel angle	Work angle				
TA=-30	WA = 5	0	9	4	0
TA=-20		0	3	2	0
TA=-10		2	0	2	0
TA=0		5	0	3	0
TA=10		1	0	0	0
TA=20		2	0	2	3
TA=10	WA=-10	3	0	0	1
	WA=-5	2	0	1	0
	WA=0	0	0	0	0
	WA=5	1	0	0	0

The brazed joints were assessed based on surface quality and mechanical behavior. The surface quality of brazed joints in each laser beam inclination condition was measured in three locations (refer to Figure 4.6). The average value of the surface roughness, expressed as the root mean square height Sq, along the braze bead as well as the standard deviation are given in Figure

4.15. The highest surface roughness values were measured under negative angles for both TA and WA. By changing the angle of processing head from TA=-20º to TA=10º the surface roughness decreased approximately 50%. The same trend was observed for work angle. The surface quality was the best when WA=5º with the laser head tilting toward the body side.

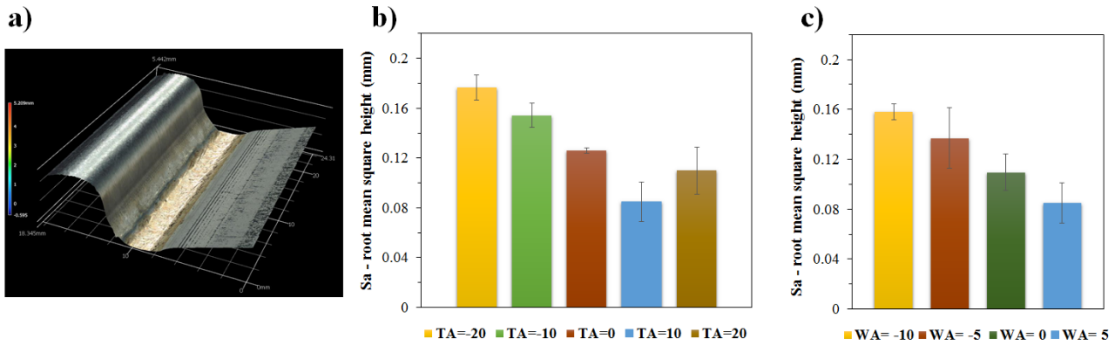

Figure 4.15 (a) 3D morphology for TA=10, (b) measured surface roughness for travel angles, (c) measured surface roughness for work angles.

4.4.3 High speed video observation – process monitoring

High-speed video imaging was used to investigate process dynamics and defect formation mechanisms. For process monitoring, experiments were conducted on hot-dip galvanized samples with a braze seam length of 250 mm. The molten pool observation results have shown occasional occurrence of spatter and degas bubbles. The burst of bubbles was noted mostly in the front and middle parts of the molten pool caused by escaping gas. The bubble bursting drove molten pool movement and led to opening and closing of cavities and the generation of surface pores (refer to Figure 4.16(c)). The expansion and burst of bubbles occurred in less than 1.25 ms and surface pores were generated in 3.5 ms. The phenomena can be explained from a perspective of viscosity and surface tension that are highly crucial to the laser brazing process. The molten filler material with weak internal friction as a result of lower viscosity helps zinc vapor to escape. Surface tension is considered as the cohesive force between the molecules of the liquid near the surface. The

attraction of liquid molecules results in an inward force that pulls them together and minimizes the surface area. The consequence of large bursting of bubbles increases the surface area of liquid by overcoming the high surface tension. Due to the temperature dependence of surface tension, higher values of surface tension were expected when moving toward the back of the molten pool where the liquid was cooler. A high surface tension helps to prevent the separated areas from closing again.

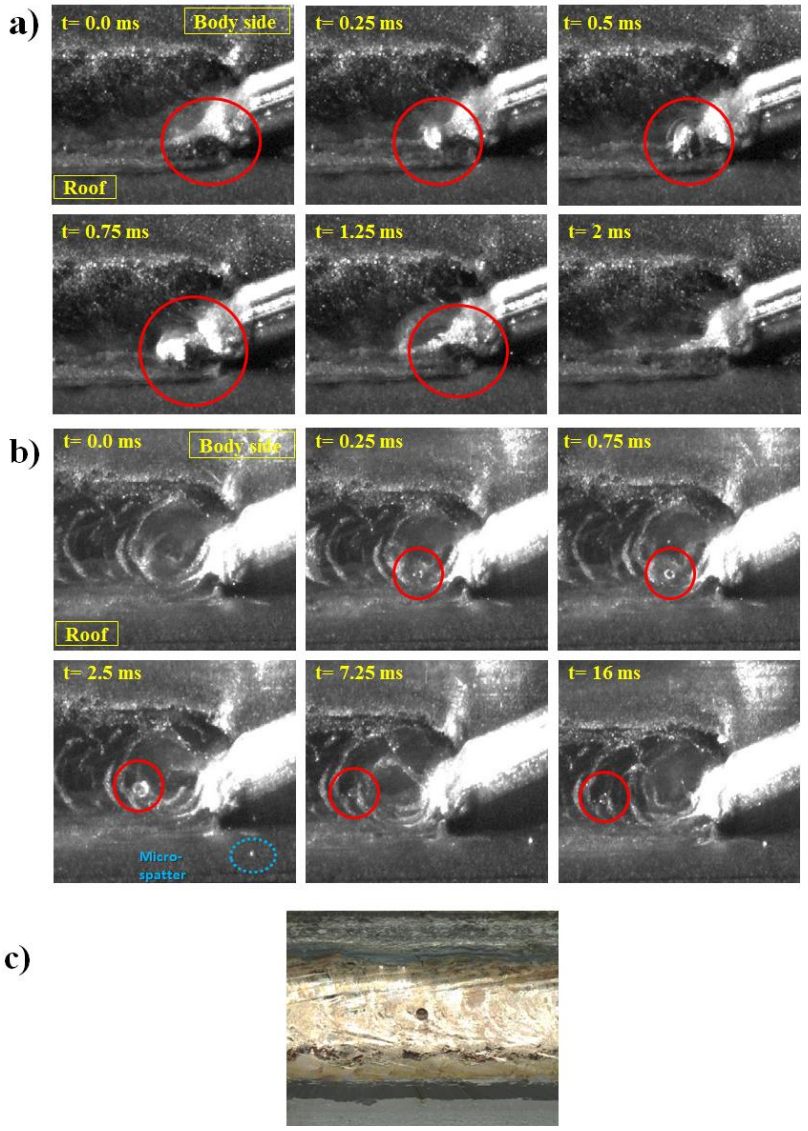

Figure 4.16 (a-b) high-speed image sequences of molten pool under bubble formation, (c) illustration of surface pore.

Spatter was categorized into two types: micro-spatter of size approximately 0.1-0.2 mm and spatter of size larger than 0.1-0.2mm. Micro-spatter was mostly observed at the melt front edge where molten filler wire was interacting with either molten zinc or vapor trajectories from zinc coating. Occasionally, micro-spatter was generated during the degassing process in which a small portion of molten material was ejected from the center of the bubble (refer to Figure 4.17(b)). A series of successive images depicting the occurrence of micro-spatter at the wetting line and burst of bubbles are shown in Figure 4.17. The majority of micro-spatter were solidified in air before touching the panels while a smaller portion landed and attached to the panels. However, the presence of micro-spatter was an indication of molten pool instability which directly affected the surface quality of brazed seams.

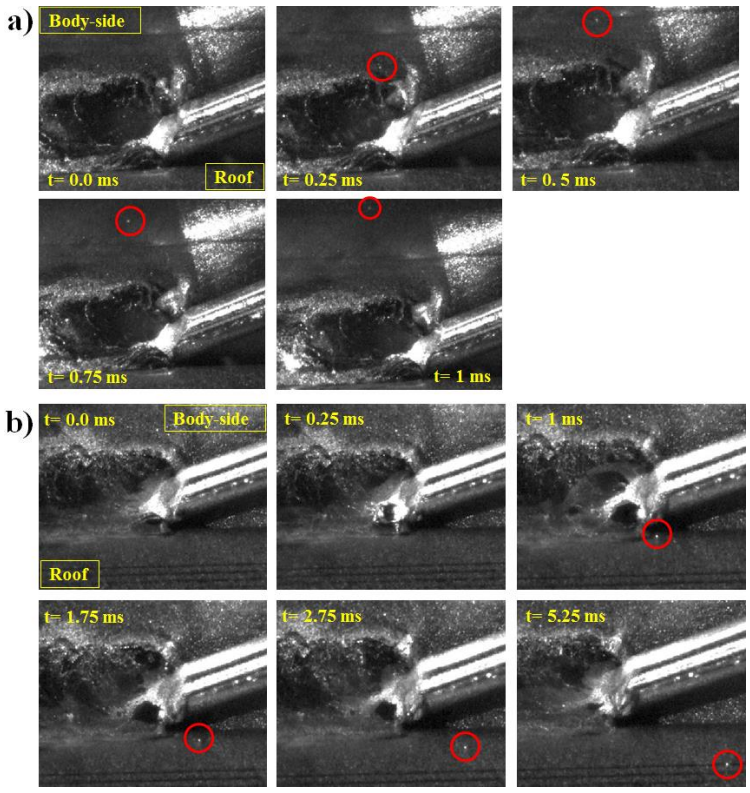

Figure 4.17 Successive images showing presence of micro-spatter in: (a) melt front, (b) degassing.

Large spatter was either attached to the panels or acted as re-entrant material to the brazed seam. Figure 4.18 illustrates a series of representative images forming these incidents during the laser brazing process. This type of spatter was mostly generated in the middle part of the molten pool where the zinc vapor pressure was relatively high. The high-pressured zinc vapor went through the melt pool to the surface, forming spatter, burst of bubbles, and causing process instabilities. The generation of micro-spatter at the wetting edge was also noticeable in Figure 4.18(a) (dotted blue line).

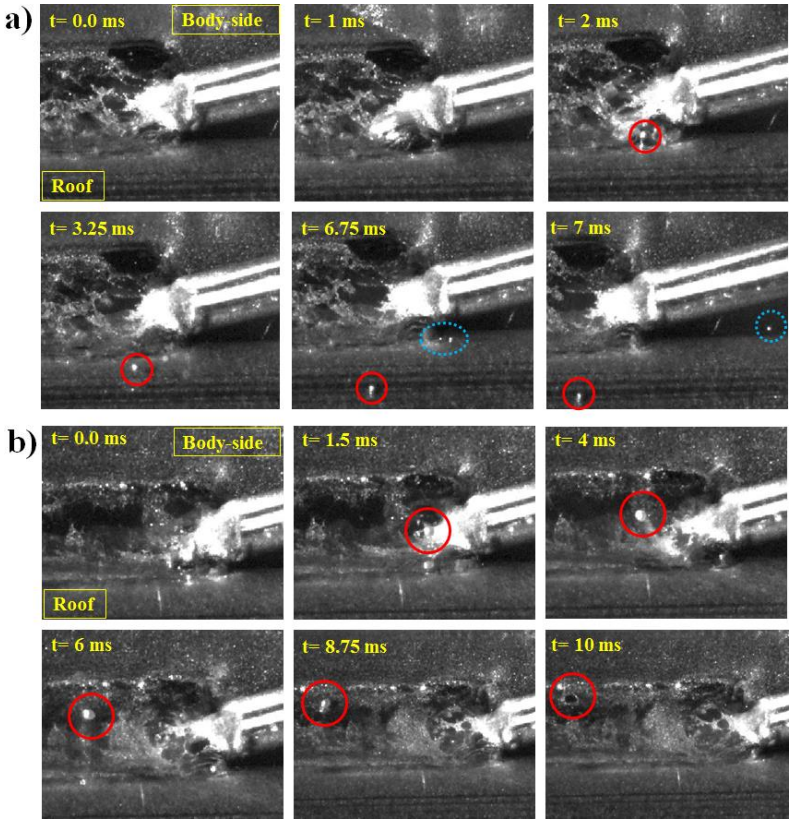

Figure 4.18 High-speed images of generated spatter in brazing process: (a) stuck, (b) re-entrant.

As discussed above, pores and spatter imperfections were directly attributed to the existence of low boiling point zinc. However, the laser beam energy distribution and temperature history were critical in ensuring a stable process. In this study, the effect of two laser beam tilt angles,

travel angle and work angle, on the stability of laser brazing was investigated. Imperfections were quantified for each laser beam tilting condition on 250 mm long braze seams. All counts of imperfections were conducted manually.

The travel angle was set at four levels; -30˚ -20˚, 0˚ and 10˚. In the case of TA= -30˚ no micro spatter in front of the melt pool was noted during the process. The negative angle of the laser beam shined the beam ahead of the wire moving direction. This helped to preheat the zinc coating so that zinc coating was partially evaporated ahead of the wetting line. As a result, the interaction of molten material with eruptive zinc vapor was minimized and improved process stability. However, several open-out holes and pores were observed. Insufficient wire feed speed was reported as the main reason in generation of open-out holes by Kimura et al. [6]. In this negative travel angle, inconsistent feeding was detected as the cause of occasionally insufficient wire feed. As shown in schematic view (Figure 4.14) the feeding nozzle was positioned in almost a vertical position. The downward spring force of tool axis was high and led to a large frictional resistance to wire movement along the substrate surface. The resulting unsmooth or jagged wire movement caused the inconsistency in adding material into the groove and occasional defects. During the process, holes were initiated at the wetting line where melt material and substrates met. Three different scenarios for the initiated holes at the image sequences of high-speed videos are shown in Figure 4.19. It was found that in a stable feeding condition, the molten material could cover the holes. Otherwise, the holes remained open until solidification. In the case of a closed hole, a propagated circular wave was observed around the melt pool surface and this observation is consistent with Heuberger et al. [18]. In the worst case, the opening hole was shifted toward the middle of the molten pool when this phenomenon coincided with the breakage of the zinc coating. The momentum of zinc breaking would cause a dramatic enlargement in the hole size which

yielded a big hole in the center of the braze seam. The breakage of zinc coating is expected in hot-dip galvanized steel with Fe2Al5 intermetallic layer [19]. The jagged wire movement was noticed in negative TA angles due to high resistance force from the panel to the wire tip. The marked black soot on panels were clearly showing the escape routes of generated zinc vapor from the bottom of the molten pool.

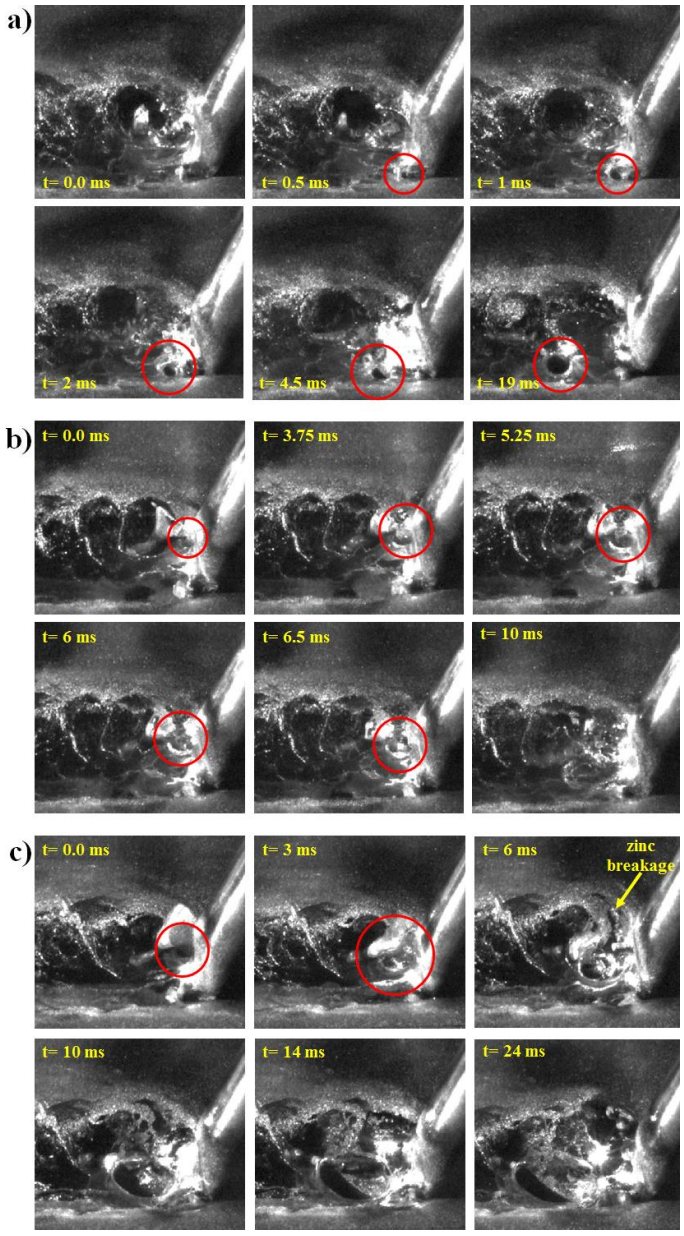

Figure 4.19 High-speed video images in brazing process with TA=-30: (a) covered hole, (b) existing hole, (c) enlarged hole.

The amount of imperfections during the process was counted for the 4 travel angle conditions and reported in Table 4.5. The number of open-out holes decreased when TA= -20° and zero in positive travel angles, where a smooth feeding condition led to the elimination of open-out holes. When TA < 0°, the wire feed was not consistent and the braze surface quality was poor. However, the number of spatter, micro-spatter, and degas decreased due to the preheating effect of laser beam and existence of open-out holes as discussed previously. The open holes in the process allowed the zinc vapor rushing out in pulses and leaving black soot marks on the panels.

Table 4.5 Number of imperfections counted on recorded high-speed videos under different TA angles.

Travel angle	Counted defects			
	Spatter	Micro spatter	Degas	Open-out hole
TA=-30	0	15	27	13
TA=-20	1	16	34	1
TA=0	1	22	40	0
TA=10	4	34	49	0

The effect of work angle on process robustness was independently studied at four levels; 5˚, 0˚, -5˚ and -10˚. The counted number of imperfections during the process are reported in Table 4.6. The number of imperfections were increased by tilting the laser head towards the roof side. The change in work angle toward either roof or body side affected the laser beam energy projection onto the panels. When WA < 0°, tilting toward roof side, the high level of absorbed energy was accompanied with a shorter leg length/wetting thickness on roof side and increased the number of degas and spatter. As a result, zinc vapor easily pushed out from the roof side and increased the amount of degas and spatter. The high number of these imperfections resulted in an agitated molten pool and surface waves. The successive images in Figure 4.20 represent the disruptive impact of this degassing phenomena in dynamics of molten pool area. The high level of disturbance not only

influenced the process robustness but also the braze quality. Surface roughness measurements (see Figure 4.15) verified the fact that brazed coupons under WA=5˚ condition contained the lowest number of degas and micro-spatter and achieved the highest surface quality.

Table 4.6 Number of imperfections counted on recorded high-speed videos under different WA angles.

Work angle	Counted defects			
	Spatter	micro spatter	degas	Open-out hole
WA=5	4	34	49	0
WA=0	5	35	124	0
WA=-5	15	56	169	0
WA=-10	22	67	270	0

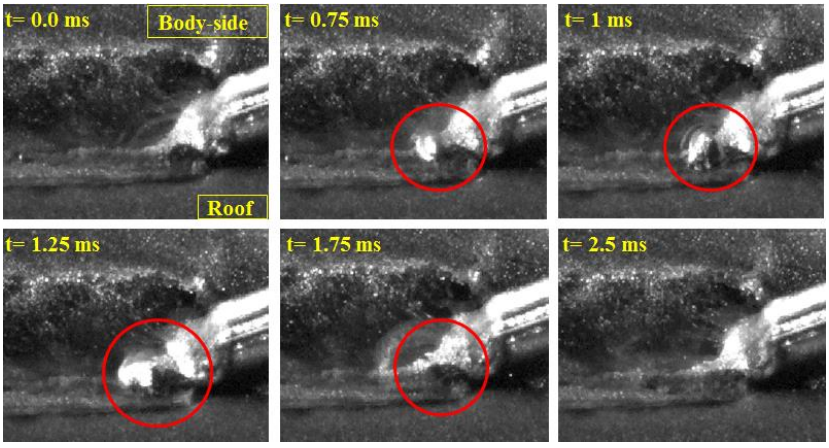

Figure 4.20 High-speed images of degas phenomena in laser brazing process with WA=5˚.

4.4.4 Simulation-based analysis

It is required that the simulation model accurately predicts the cross-sectional dimensions of the seam with respect to the given process parameters. Figure 4.21(a) compares the experimentally obtained and numerically simulated cross-sections of the laser brazed joint. As can be seen, there is a good agreement between experimental measurement and numerical prediction in terms of seam

curvature, leg lengths on both sides, and throat thickness. This validated numerical model was then used for process analysis and improvement.

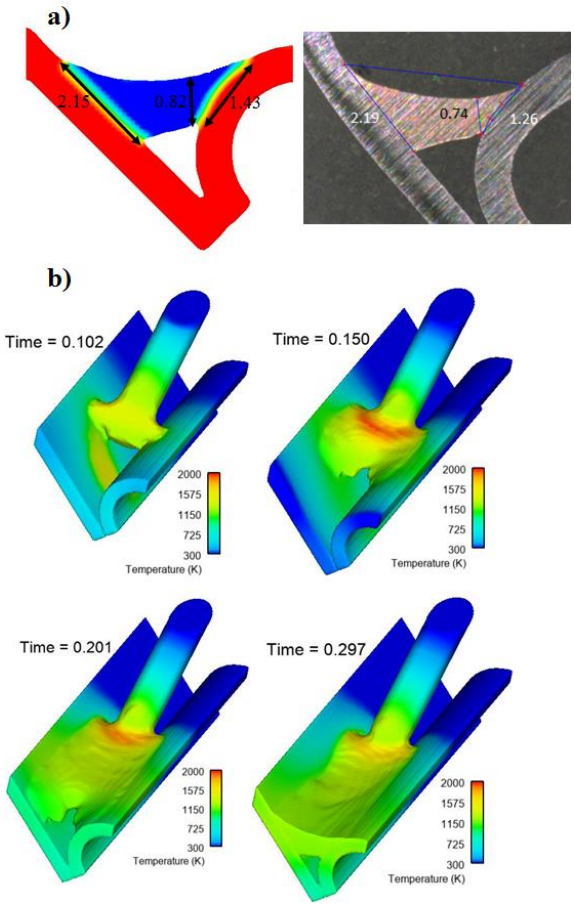

Figure 4.21 (a) Comparison between numerically simulated and experimentally obtained cross-sections (LP=3.8 kW, WFS=60 mm/s, BS=65 mm/s); (b) Temperature history at different steps of laser joining process.

Laser irradiation was considered as a surface flux to simulate the thermal field. The filler material was heated up and melted by laser irradiation which then flowed into the groove thereby wetting and joining the heated steel panels. The process was followed by continuously melting the filler wire and wetting over the panels. Figure 4.21(b) depicts the simulated laser brazing process over different time intervals.

The numerically calculated temperature field was utilized to investigate the effect of laser inclination angles (TA and WA) on the brazing process. The distance between wetting line and zinc evaporation front line was introduced as an indicator of possible spatter occurrence. Figure 4.22 shows the temperature contours resulting from TA levels of -30˚ -10˚, 10˚ and 20˚. The black line represents the zinc evaporation front (1180^{o}K). As shown in TA>0 a short distance less than 0.15 mm was calculated between zinc evaporation line and molten filler wire wetting area. Whereas, by tilting the laser head toward negative TA angle such as TA=-30^{o}the distance between these two lines was increased up to 0.55 mm. In other words, an evaporation of zinc coating was done ahead of the wetting zone. The simulation results have not shown significant influence of WA on the distance between wetting and zinc evaporation lines. The predicted distance maintained a length of 0.15 mm for various WA conditions. The vaporization of zinc coating ahead of wetting was beneficial in increasing the robustness of brazing process by reducing the interaction of melt filler material and disruptive zinc vapor. The further away the zinc evaporation line is from the wetting line, the less amount of zinc can be dissolved into the molten pool and less possibility of degassing and spatter. The high-speed video observations and process defects count in Section 4.2 have also verified the influential role of negative travel angles in reducing spatter.

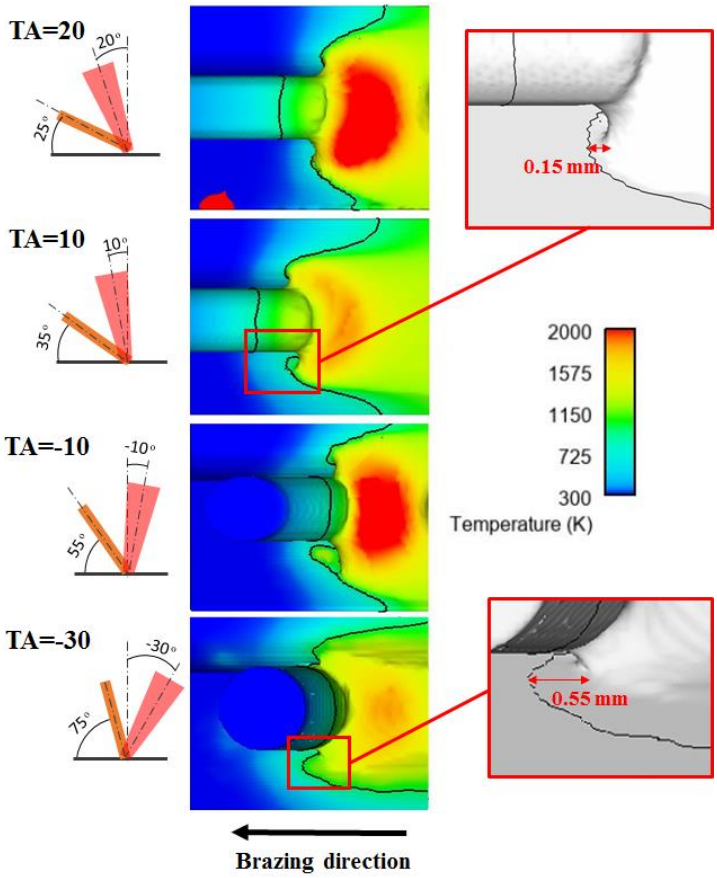

Figure 4.22 Top view of simulated brazed seams under different TA angles. The isothermal line of the zinc evaporation temperature (1180 K) is shown by a black line.

4.4.5 Macro-metallographic and SEM analysis

The load capacity of brazed joints is directly influenced by the geometry of the brazed seam (refer to Figure 4.6). In addition to the bonding length along the body and roof sides the weld throat thickness plays a crucial role. Therefore, the variation of travel and work angles on brazed seam dimension were studied. The micro section of brazed coupons at different TA angles with their associated dimensions are provided in Figure 4.23. Among all cases the roof leg length was shorter than the body side length. The throat thickness and leg lengths decreased when the travel angle moved toward positive values and reached the lowest values at TA=10°. In addition, this travel angle was accompanied with the best surface quality as discussed in Section 4.1. For TA<0, the

dominancy of a vertical force pushing down more molten material into the groove eventually created a thick throat thickness. The other consequence of this configuration was inconsistency of wire feeding that led to several open out holes as shown in Figure 4.23(a). Despite the increase of surface roughness at TA=20°, the dimensional values were increased and the occurrence of open-out holes were eliminated. The experimental observations have shown that the change of TA angle exhibited a larger effect on braze quality than the cross-section of the seam.

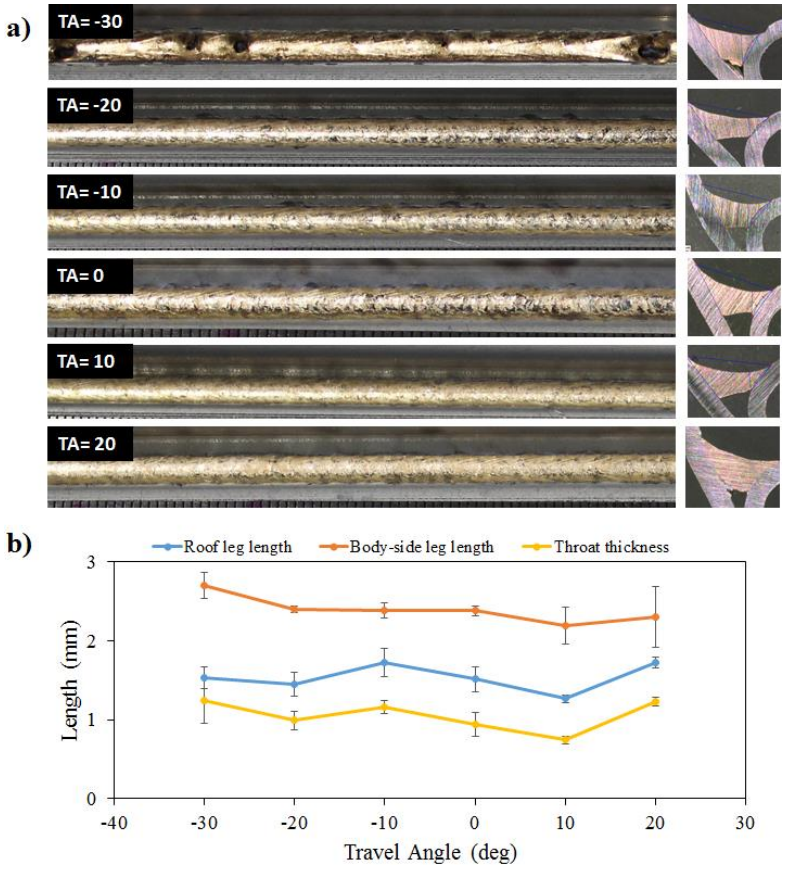

Figure 4.23 (a) Seam surface and micro section of brazed coupons at TA angles, (b) dimensional values of brazing seam.

The change of work angle, aside from its influential role on the surface quality and process stability, affected the dimensional values. For WA>0°, where the laser beam inclined toward the body side, the leg length on this side increased while the roof length had the lowest value. As

shown in Figure 4.24 the thickest braze throat with the preferred shape of brazed seam was achieved at WA=0°, where an even braze geometry with similar leg lengths was generated on both roof and body sides.

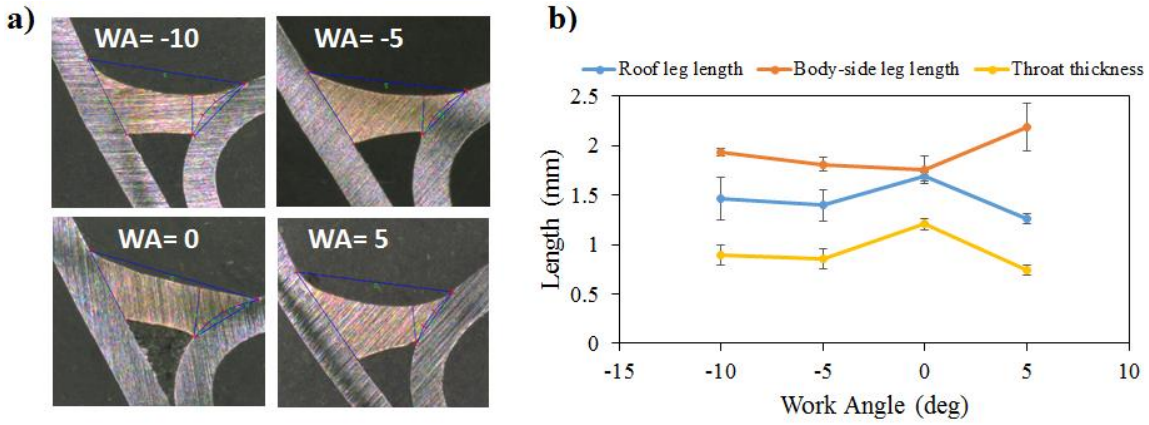

Figure 4.24 (a) Micro sections of brazed coupons at different WA angles, (b) dimensional values of brazing seam.

The zinc accumulation at the seam edges is an inevitable fact in the laser brazing process applied to galvanized steel [19]. The propagation of Zn liquid toward the bead toe was the main reason for the zinc pile-up. This pile-up was laid on the fluid dynamic phenomena (Marangoni flow) that dissolved zinc into the liquid silicon-bronze pushed by the newly liquefied wire. The cross-sectional examination of brazed edges derived from different TA angles confirmed the zinc accumulation and diffusion. SEM and element mapping of seam edges at the body side are shown in Figure 4.25. The amount of accumulated zinc at the seam edge was decreased by moving toward negative TA arrangements. This reduction of zinc was attributed to the pre-vaporization or partially removing the zinc coating by the laser beam at negative TA angles.

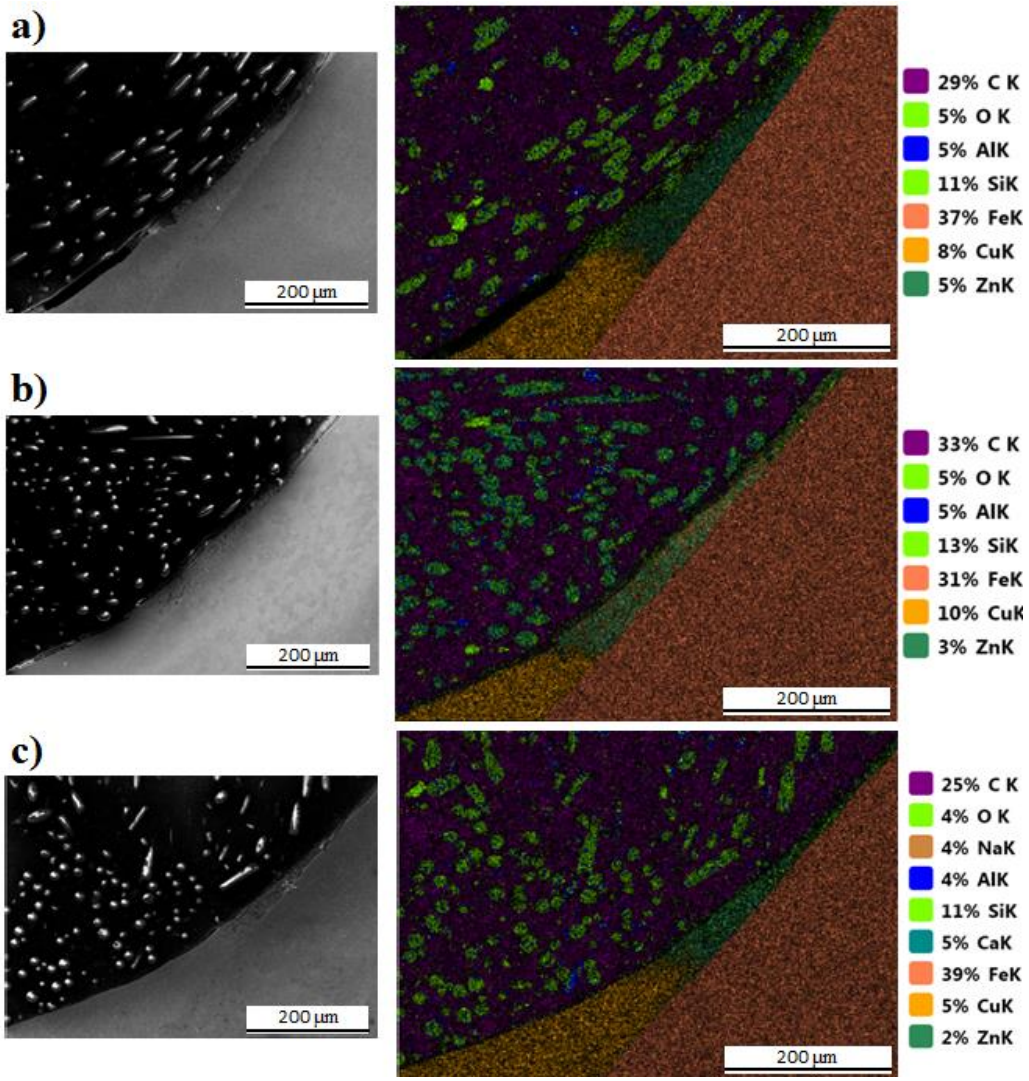

Figure 4.25 SEM images and EDX scanning of the seam edges: (a) TA=20°, (b) TA=10°, (c) TA=-30°.

4.4.6 Tensile test

The effect of variations in work and travel angles were also studied from the perspective of mechanical performance. Tensile tests were performed to investigate the strength of brazed joints. All tensile coupons failed within the base material with a maximum load ranging from 2.8 kN to 3.4 kN. Figure 4.26(a-b) provides the dimension and representative fracture mode of the test coupons. Tensile test results exhibit a minor influence of braze angles on the mechanical strength

of the brazed joints. Thus, a seam with sufficient strength can be achieved at various WA and TA angles as long as the throat thickness requirements are met.

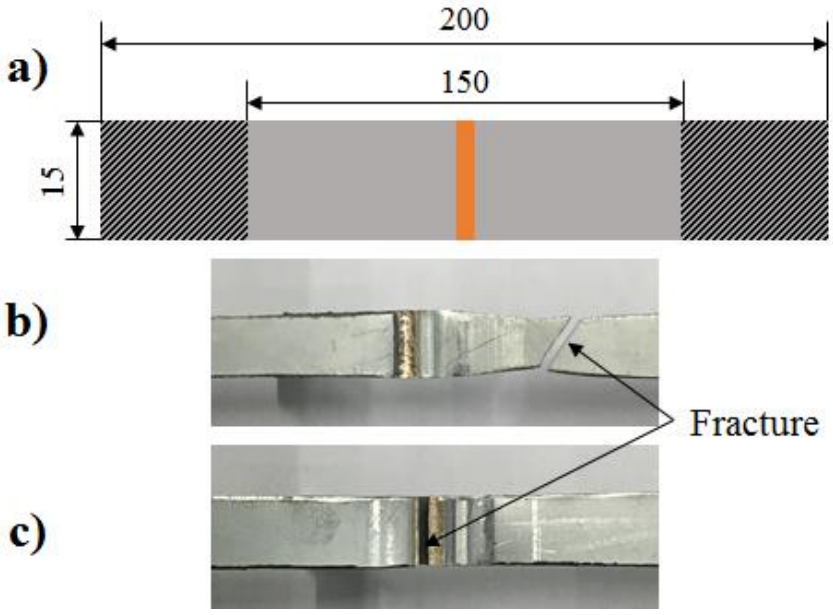

Figure 4.26 (a) Schematic view of prepared specimen for tensile test (dimensions are in mm), (b) base metal fracture mode, (c) brazed bead fracture mode.

Further investigations were done to study the relation between mechanical strength and cross-section dimensional values of brazed joints. The experimental tensile test results of brazed coupons fabricated using LP=4.3 kW, WFS=70 mm/s and BS=90 mm/s exhibit a strong dependence of strength on the throat thickness rather than on the leg lengths. In joints with a throat thickness below the 0.5 mm the fracture mode was altered from base metal failure to brazed seam failure (see Figure 4.26(c)). Thus, the minimum acceptable value for the throat thickness should be 0.5 mm for roof joint applications fabricated from the stack-up investigated in this work.

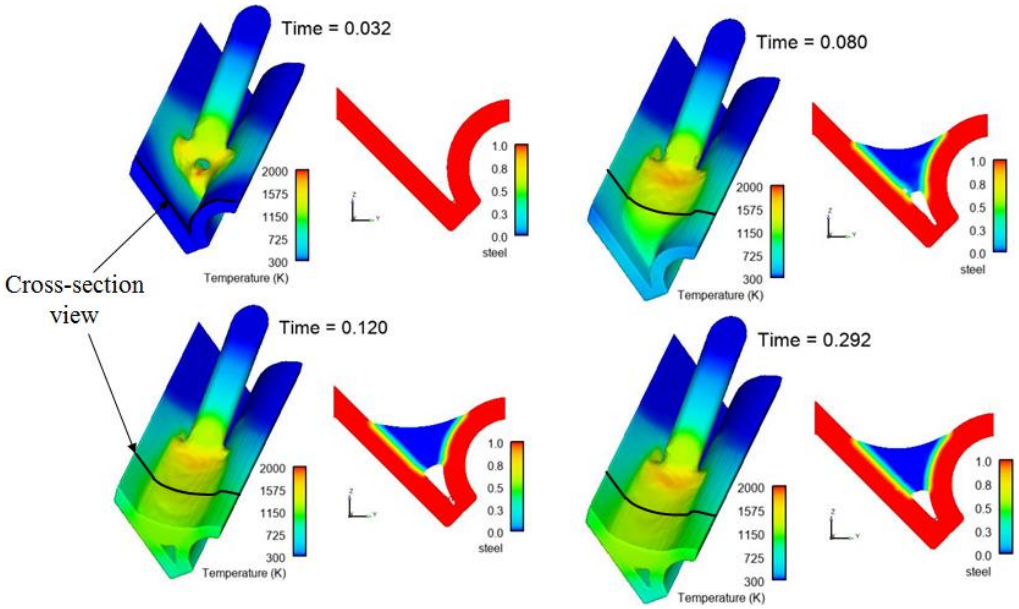

Figure 4.27 Predicted temperature history and seam cross sectional characteristics under TA=-30° and wire feeding angle of 35°.

In summary, process configurations having negative travel angles enabled pre-evaporation of zinc coating. Smooth wire movements can be achieved by a proper design of wire feed module to maintain a low wire feed angle. Process simulation of the brazing process having negative travel angle (TA=-30°) with the wire feed angle of 35 degrees with respect to the surface of panels have shown promising results. As shown in Figure 4.27, not only could temperatures above the zinc evaporation be achieved on panels ahead of the wetting line but also open-out holes were eliminated and cross-sectional seam properties were in an acceptable range.

4.5 Conclusions

In this study the laser brazing of hot-dip galvanized steels was investigated with the purpose of increasing the process robustness and decreasing spatter. The effects of single mode laser beam inclination on process stability and seam characteristics were studied. Both beam travel angle and work angle were discussed. High-speed video imaging was used to capture molten pool dynamics

and occurrence of defects in the brazing process. In addition, a numerical simulation model was established to study the formation of braze seam and calculate the temperature history and velocity fields in the melt area. A good agreement was found between the measured and predicted dimensions of the brazed seam. The experimental and numerical observations verified the effectiveness of negative travel angle in spatter reduction. The key results of this investigation are summarized as follows:

1. Experimental observations revealed that spatter occurrence was attributed either to the interaction between melt pool front edge and erupted particles of zinc coating at the wetting line or to zinc dissolution and eventual evaporation from the melt pool front.
2. Numerical simulation shows that the zinc evaporation line extended up to 0.55 mm in front of the wetting line with negative travel angles. A change in WA did not cause any considerable change.
3. The change in TA affected the brazed bead geometry and its quality. For all tested travel angles, roof leg length of the resulting braze was shorter than the body side leg length. Negative TAs were benefiting the process by pre-vaporizing and/or partially removing zinc coating. The inconsistency in wire feeding due to a high resistance force on the wire tip can be resolved by modifications of the filler wire feeding module.
4. Change of WA exhibited significant effects on braze geometrical property and its quality. Positive work angles (WA>0) increased the leg length on body side and negative ones (WA<0) increased the roof side leg length. An even seam geometry was achieved when WA=0°.

5. High-speed video observations enabled the observation that by tilting the laser beam towards the roof side (WA<0) the number of degas increased with a majority occurring at the roof side. One reason is postulated to be that the more absorbed energy on the roof side causes the dissolved zinc to rise to the surface through shorter roof leg length.

References

[1] M. Ungers, D. Fecker, S. Frank, D. Donst, V. Märgner, P. Abels, S. Kaierle, In-situ quality monitoring during laser brazing, Phys. Procedia. 5 (2010) 493–503.

[2] A. Grimm, Prozessanalyse und-überwachung des Laserstrahlhartlötens mittels optischer Sensorik, (2012).

[3] S. Frank, M. Ungers, R. Rolser, Coaxial Control of Aluminum and Steel Laser Brazing Processes, Phys. Procedia. 12 (2011) 752–760.

[4] F. Lu, B. Lu, X. Tang, S. Yao, Study of influencing factors and joint performance of laser brazing on zinc-coated steel plate, Int. J. Adv. Manuf. Technol. 37 (2008) 961–965.

[5] A. Koltsov, N. Bailly, L. Cretteur, Wetting and laser brazing of Zn-coated steel products by Cu–Si filler metal, J. Mater. Sci. 45 (2010) 2118–2125.

[6] S. Kimura, S. Takemura, M. Mizutani, S. Katayama, Laser brazing phenomena of galvanized steel and pit formation mechanism, Int. Congr. Appl. Lasers Electro-Optics. 2006 (2006) P528.

[7] R. Akhter, W.M. Steen, K.G. Watkins, Welding Zinc-Coated Steel with a Laser and the Properties of the Weldment, J. Laser Appl. 3 (1991) 9–20.

[8] W. Chen, P. Ackerson, P. Molian, CO2 laser welding of galvanized steel sheets using vent holes,Mater.Des.30(2009)245–251.

[9] M.P. Graham, D.M. Hirak, H.W. Kerr, D.C. Weckman, Nd:YAG laser welding of coated sheet steel, J. Laser Appl. 6 (1994) 212–222.

[10] J. Ma, F. Kong, B. Carlson, R. Kovacevic, Two-pass laser welding of galvanized high-strength dual-phase steel for a zero-gap lap joint configuration, J. Mater. Process. Technol. 213 (2013) 495–507.

[11] C. Mittelstädt, T. Seefeld, D. Reitemeyer, F. Vollertsen, Two-beam Laser Brazing of Thin Sheet Steel for Automotive Industry Using Cu-base Filler Material, Phys. Procedia. 56 (2014) 699–708.

[12] M. Mohammadpour, N. Yazdian, G. Yang, H.-P. Wang, B. Carlson, R. Kovacevic, Effect of dual laser beam on dissimilar welding-brazing of aluminum to galvanized steel, Opt. Laser Technol. 98 (2018).

[13] W. Reimann, M. Dobler, M. Goede, M. Schmidt, K. Dilger, Three-beam laser brazing of zinc-coated steel, Int. J. Adv. Manuf. Technol. 90 (2017) 317–328.

[14] V.R. Voller, C. Prakash, A fixed grid numerical modelling methodology for convection-diffusion mushy region phase-change problems, Int. J. Heat Mass Transf. 30 (1987) 1709–1719.

[15] J. Cho, S.-J. Na, Implementation of real-time multiple reflection and Fresnel absorption of laser beam in keyhole, J. Phys. D. Appl. Phys. 39 (2006) 5372.

[16] A.R. Marder , The metallurgy of zinc-coated steel, Prog. Mater. Sci. 45 (200) 191–271.

[17] J.D. Culcasi, P.R. Seré, C.I. Elsner, A.R. Di Sarli, Control of the growth of zinc–iron phases in the hot-dip galvanizing process. Surf. Coat. Technol. 122 (1999) 21–23.

[18] E. Heuberger, D. Schmid, J.-P. Weberpals, F. Tenner, M. Schmidt, Influence of the brazing speed on the seam characteristics in laser beam brazing of zinc coated steel, J. Laser Appl. 31 (2019) 22407.

[19] W. Reimann, S. Pfriem, T. Hammer, D. Päthe, M. Ungers, K. Dilger, Influence of different zinc coatings on laser brazing of galvanized steel, J. Mater. Process. Technol. 239 (2017) 75–82.

Chapter 5

SUMMARY AND FUTURE WORK

In this thesis, the single-beam and multi-beam laser welding-brazing techniques for joining similar and dissimilar materials have been studied experimentally and numerically. Heat transfer and fluid flow simulation models were developed to better understand the physics during the process and well expand the experimental observations of welded joints. Based on the obtained results the following conclusions can be made:

5.1 Effect of dual laser beam arrangement

The feasibility of joining galvanized steel (hot-dip galvanized and electro-galvanized coating) and Al6022 aluminum alloy in a coach-peel configuration was investigated using a laser in dual-beam mode to obtain a sound and uniform brazed bead with high surface quality at a high welding speed. The effects of changing the laser arrangement and coating type on the thickness of intermetallic compound (IMC), surface roughness, edge straightness, and tensile strength of the resultant joints were studied. A new technique was introduced to measure the edge straightness of brazed joints, and criteria for acceptable ranges were identified based on human vision resolution. The lowest surface roughness and better mechanical performance were observed in dual cross-beam laser brazed joints. The deviation of measured edge straightness in electro-galvanized steel panels was lower than the hot-dipped ones. It was found that high scanning speed minimized the thickness of IMC as thin as 3 μm, and change of dual-beam laser shape altered the failure location from the steel-brazed interface toward the Al-brazed interface. The validated FEM thermal simulations evidenced that the peak temperatures at the Al-steel interface were around the critical temperature range 700-900˚C that is required for the highest growth rate of IMC. However, the

time duration that the molten pool was placed inside this temperature range was less than 1s, and this duration was too short for diffusion-control based IMC growth.

5.2 Effect of filler wire composition

Surface roughness and mechanical strength are the important criteria affected by the process parameters during welding. These parameters are used to judge the weld quality for some applications, such as the automotive industry. Thus, the influences of the main laser welding-brazing process parameters (laser power, wire feed speed, and scanning speed) was studied as well as the type of consumable material on the mechanical strength and surface roughness of welds. Analytical models that related the output properties of interest to process parameters were also developed. The response surface methodology (RSM) and desirability function were utilized to conduct a multi-response optimization approach. It was found that the laser power of 3.2kW, welding speed of 60mm/s, and wire feed rate of 70mm/s can be introduced as the optimum processing condition by considering the minimum surface roughness and maximum mechanical strength. Four different filler wire materials (AlSi12, AlSi5, AlSi3Mn1, and ZnAl15) in an optimized processing condition were employed to study the effects of the wire alloying elements on the microstructure, surface quality, and mechanical resistance of the welded joints. The measured intermetallic compound, IMC, layer at the Fe/Al interface of joints revealed that AlSi12 filler wire resulted in the thinnest IMC layer at less than 2μm. In contrast, this value increased to 7μm for joints with ZnAl15 wire. In terms of surface roughness, the lowest (Ra=0.917 μm) and highest (Ra=2.83 μm) values were achieved by using AlSi3Mn1 and ZnAl15 wires, respectively. The Zn-based filler wire offered the maximum tensile resistance around 180N/mm. The joints with AlSi12 wire had a mechanical resistance of 120 N/mm and lower values of IMC layer thickness and surface roughness. Therefore, AlSi12 filler material is

recommended as the laser brazing filler material for joining dissimilar aluminum-galvanized steel coach peel panels in automotive body-in-white (BIW) fabrication applications.

5.3 Effect of laser beam inclination angle

Potential defects associated with laser brazing process can be attributed either to the main process parameters or external trigger events from all parts of the equipment in use. As a result, a design of experiment method accompanied with multi-physics simulation model were used to generate a “brazibility graph”. The graph can be used not only for choosing the appropriate set of process parameters but also describe the response of the laser brazing process to typical factor variations encountered in production. As discussed in chapter 2, the difference in coating type (HDG and EG) has affected the edge straightness of laser brazed joints at the steel side. Difference in type of zinc coating was considered as the influential factor in the laser brazing of galvanized steels. Therefore, the effect of different types of zinc coating was characterized on the laser brazing process. A more detailed observations of the process dynamics showed intermittent breakage of zinc coating, eruptive evaporation of zinc, and burst of particles in front of the processing zone in hot-dip galvanized steel. Therefore, the use of HDG steel sheets as base material is making the laser brazing process more challenging and lead to the formation of spatter and a wavy appearance of the seam. Experimental observations revealed that spatter occurrence was attributed either to the interaction between melt pool front edge and erupted particles of zinc coating at the wetting line or to zinc dissolution and eventual evaporation from the melt pool front. The laser beam inclination angle (travel angle and work angle) was introduced to decrease spattering and increase the process robustness in laser brazing of hot-dip galvanized steels. It was found that negative travel angles helped to move the zinc evaporation front ahead of the wetting front and reduce the

interaction between the zinc vapor and melt pool. Numerical simulation shows that the zinc evaporation line extended up to 0.55 mm in front of the wetting line with negative travel angles.

5.4 Future work

The following steps should be taken for future work:

- Accommodate the effect of zinc coating layer explicitly in the developed fluid-flow simulation model to predict frequent formation of seam imperfections and implement temperature dependent material properties to obtain more precise results.
- Feasibility study of using adjustable ring mode (ARM) as a new generation of fiber laser source in the laser brazing application. The ring beam can be used to evaporate the zinc coating prior to wetting and stabilize the molten pool. The center beam can be dedicated to melt of the filler material.
- Implement a close-loop control system to dynamically adjust the laser intensity distribution during the laser brazing process on hot-dip galvanized steels with respect to the temperature distribution.
- Develop a new type of filler material with lower melting range than the boiling temperature of the zinc layer to eliminate the spatter occurrence in laser brazing of galvanized steel substrates.

5.5 Publications

1. **Masoud Mohammadpour**, Baixuan Yang, Hui-Ping Wang, John Forrest, Michael Poss, Blair Carlson, Radovan Kovacevic, Influence of laser beam inclination angle on galvanized steel laser braze quality, Optics & Laser Technology, .

2. **Massoud Mohammadpour**, Nima Yazdian, Guang Yang, Hui-Ping Wang, Blair Carlson, Radovan Kovacevic, Effect of dual laser beam on dissimilar welding-brazing of aluminum to galvanized steel, Optics & Laser Technology, 98 (2018) 214-228.
3. **Massoud Mohammadpour**, Nima Yazdian, Hui-Ping Wang, Blair Carlson, Radovan Kovacevic, Effect of filler wire composition on performance of Al/Galvanized steel joints by twin spot laser welding-brazing method, Journal of Manufacturing Processes, 31 (2018) 20-34.
4. Guang Yang, **Masoud Mohammadpour**, Nima Yazdian, Junjie Ma, Blair Carlson, Hui-Ping Wang, Radovan Kovacevic, Cross-beam laser joining of AA 6111 to galvanized steel in a coach peel configuration, Lasers in Manufacturing and Materials Processing, 4 (2017) 45–59.
5. Lin Wang, **Masoud Mohammadpour**, Baixuan Yang, Xiangdong Gao, Jean-Philippe Lavoie, Klaus Kleine, Fanrong Kong, Radovan Kovacevic, Monitoring of keyhole entrance and molten pool with quality analysis during adjustable ring mode laser welding, Applied Optics, 6 (2020) 1576-1584.
6. Nima Yazdian , **Masoud Mohammadpour** , Fanrong Kong , Radovan Kovacevic, Hybrid laser/arc girth welding of 304L stainless steel tubes, part 1 – Pore mitigation, thermal analysis and mechanical properties, Journal of Pressure Vessels and Piping, 163, (2018) 75-93.
7. Nima Yazdian, **Masoud Mohammadpour**, Reza Razavi, Radovan Kovacevic, Hybrid laser/arc welding of 304L stainless steel tubes, part 2 – Effect of filler wires on microstructure and corrosion behavior, Journal of Pressure Vessels and Piping, 163, (2018) 45-54.